DIRECT OBSERVATIONS ON MICROSTRUCTURE EVOLUTION OF CEMENT SYSTEMS AT EARLY AGES

By

MASOUD MORADIAN

Bachelor of Science in Civil Engineering
K. N. Toosi University of Technology
Tehran, Iran
2008

Master of Science in Civil Engineering/Structure
University of Tehran
Tehran, Iran
2011

Submitted to the Faculty of the
Graduate College of the
Oklahoma State University
in partial fulfillment of
the requirements for
the Degree of
DOCTOR OF PHILOSOPHY
May 2017

DIRECT OBSERVATIONS ON MICROSTRUCTURE EVOLUTION OF CEMENT SYSTEMS AT EARLY AGES

Dissertation Approved:

Dr. M. Tyler Ley

Dr. Stephen A. Cross

Dr. Julie A. Hartell

Dr. Allen Apblett

ACKNOWLEDGEMENTS

Many individuals contributed to my work and I would like to properly acknowledge them. I greatly appreciate the support, patience, limitless energy and empathy, and guidance given to me by my academic advisor, Dr. M. Tyler Ley. Dr. Ley's comprehensive approach to solve complicated problems and his efforts in reviewing of numerous revisions of my papers have greatly contributed to this dissertation.

I would like to thank my committee members, Dr. Stephen A. Cross, Dr. Julie A. Hartell, and Dr. Allen Apblett who generously agreed to support me. I would especially like to thank Dr. George W. Scherer (Princeton University), Dr. Jeffrey W. Bullard (National Institute of Standards and Technology), and Dr. Zachary Grasley (Texas A&M University) for their thoughtful comments on my papers.

I greatly appreciate the encouragement of my family, my wife Ghazal Sokhansefat, my father and mother (Ali and Fatemeh) and my brothers (Saeed, Majid, and Hossein); I could have not done this without their inspiration.

This work was supported by funding from Federal Highway Administration (FHWA) Exploratory Advanced Research (EAR) program and funding from the United State National Science Foundation (NSF). I thank our collaborators, Brad Chmelka (University of California, Santa Barbara), Andreas Lüttge and Rolf Arvidson (University of Bremen), Denise Silva and Josephine Cheung (W.R. Grace), and Larry Roberts (Roberts Consulting), for their insightful advice on this work. The XRD measurements were made at W.R. Grace by Jeffrey Nicolich.

Use of the Center for Nanoscale Materials and the Advanced Photon Source, both Office of Science user facilities, was supported by the U.S. Department of Energy, Office of Science, Office of Basic Energy Sciences, under Contract No. DE-AC02-06CH11357. Special thanks go to Xianghui Xiao, Volker Rose, and Robert Winarski (Argonne National Lab).

Finally, it was my great privilege to work with my teammates Qinang Hu, Mohammed Aboustait, Taehwan Kim, Bret Robertson, David Porter, and Jake LeFlore. A special thanks is also given to Narges Nourian for all of her help on with the data analysis.

Name: MASOUD MORADIAN

Date of Degree: MAY, 2017

Title of Study: DIRECT OBSERVATIONS ON MICROSTRUCTURE EVOLUTION OF CEMENT SYSTEMS AT EARLY AGES

Major Field: CIVIL ENGINEERING

Abstract: There is limited understanding of the mechanisms or direct measurements of cement paste hydration, as the main component that determines mechanical, durability, and rheology properties of concrete. This dissertation uses non-destructive in-situ X-ray imaging at multiple length scales (from 15.6 nm/pixel to 1.45 μm/pixel) to follow the three dimensional microstructural evolution and chemical composition change of ordinary portland cement (OPC) and monoclinic tricalcium silicate (mC_3S) paste at early ages.

Microscale resolution observations are made on paste at industrially relevant water-to-solids ratios between 0.40 and 0.70 to investigate the solidification of cement paste, evolution of air-filled void system, and stress induced change in kinetics of hydration. Complementary nanoscale resolution measurements were also made for a collection of OPC and mC_3S particles at higher w/s to obtain microstructural and chemical information during hydration.

The results from multiple techniques and different solution environments show that during the first hours of the reaction, hydration products with Ca/Si>3 form on and near the surface of the hydrating particles. These hydration products seem to change in chemistry and density over time. This process seems to be important to the induction and acceleration period of cement hydration.

On the other hand, at the end of the induction period, the volume of air-filled voids reaches a maximum value and then decreases during the acceleration period and stays constant. The void distribution changes from a few coarse voids to a large number of smaller and more uniformly distributed voids after 10 h. This behavior is suggested to be controlled by changes in the ionic strength that cause exsolution of dissolved air from the pore solution.

The results obtained from the loading experiments show that stress applied between 24 h and 60 h alters hydration kinetics of portland cement. The application of load caused an increase in stiffness, early age creep, and dissolution of individual cement particles in the highly loaded samples. These measurements provide insights into the microstructural changes that occur due to early age stress applications during the hydration of portland cement. Mechanisms are presented that discuss the observed behaviors.

TABLE OF CONTENTS

Chapter Page

LIST OF TABLES

Table Page

LIST OF FIGURES

Figure Page

Figure Page

CHAPTER I

INTRODUCTION

1-1-Introduction

Concrete is the most consumed construction materials in the world [1]. The wide availability and inexpensive nature of the required materials as well as desirable mechanical and durability performance make concrete a useful building material. Cement paste is used to bind the aggregates in a concrete mixture together and plays an important role in the strength, durability, and rheology of concrete. Unsurprisingly, the hydration of cement paste has received significant attention among researchers [2-5]. In spite of numerous works performed to understand cement hydration, the principal mechanisms of hydration, particularly at the early ages, are still a subject of controversy [2, 3, 5].

Hydration of cement related powder is an exothermic reaction. Once water is added to cement, there is a short period of rapid initial reactions identified by a large exothermic signal in isothermal calorimetry curve [2]. Later, the rate of heat release decreases significantly and then stays about a constant value during a period called the induction period. This time period is practically very important since concrete is fresh and can be transported and placed to the desired shape. After a certain time, the induction period is terminated and the reactions cause heat release again during a period called the acceleration period followed by another decelerating rate period called the deceleration period [2]. These time periods correspond to important properties of

cement paste such as setting time and strength gain. However, there is currently little understanding of the transition between these periods [2, 3, 5].

Many studies of hydration use bulk measurements to study the process and so they cannot provide detailed measurements of the individual particles during the reactions. Some of these techniques include isothermal calorimetry, chemical shrinkage, pore solution analysis, quasi-elastic neutron scattering (QENS), and nuclear magnetic resonance (NMR) [2, 6-13]. Some work has also used imaging techniques to make observations of the evolution of the microstructure over time. This is typically done with scanning electron microscopy (SEM) or transmission electron microscopy (TEM) on samples where hydration has been arrested [14-17]. Although SEM and TEM provide images with high resolution, the results are limited to the investigated 2D cross-section of the sample [18]. In addition, the required sample preparation such as polishing may cause artifacts in fragile samples.

X-ray computed tomography (XCT) is a powerful and non-destructive technique that can be completed in many cases with no sample preparation with a spatial resolution of as small as a few nanometers (nano tomography) [19-21] to several microns (micro tomography) [4, 22, 23]. XCT is widely utilized in medicine to visualize biological samples non-destructively [24, 25]. These methods are similar but the length scales are different. A series of 2D X-ray radiographs are acquired from different viewing angles and the data are used to build a 3D rendering of the sample. The 3D rendering can be used for morphological and quantitative analyses. The gray value in the produced images is a function of X-ray absorption and can indicate differences in chemistry and density of the materials [26-28]. The contrast in gray value intensities can be used to evaluate XCT dataset quantitatively by separating the collected images into regions of different constituents.

In spite of the powerful abilities of ordinary XCT, the necessary time for data acquisition at a micron length scale may be several hours and so it cannot be used to study rapidly evolving processes, such as what occurs during the first hours of cement hydration [4, 29, 30]. Recent breakthroughs in X-ray

imaging now allow tomography data collection to be made at near video acquisition rates at the Advanced Photon Source (APS) at Argonne National Laboratory. The technique is named fast computed tomography (fCT). This advancement is possible because of improvements in detectors, precision stages, and increased photon flux [29-33].

In this dissertation, several different types of X-ray imaging techniques are used to study cement hydration of portland cement related powders at different length scales. These techniques include fCT, ordinary X-ray computed tomography (XCT), Transmission X-ray Microscopy (TXM), and Nano Computed Tomography (nCT) at multiple length scales. In addition, SEM with Energy-Dispersive X-ray Spectroscopy (EDS) and Nano X-ray Fluorescence (nXRF) were used to evaluate compositional changes. In addition, a special testing setup is design to investigate the impact of loading on microstructure evolution and physical properties of cement paste. The mechanisms and practical significance of the measurements are also discussed.

Improved knowledge of these processes would allow for better control over cementitious materials and improved usage of both chemical and mineral admixtures. This would allow for improvements in the economy, constructability, and sustainability for concrete. The data can also be useful to verify analytical models and improve their assumptions.

1-2-Research Objectives

There is little agreement on the basic mechanisms of cement hydration. In this dissertation, three fundamental topics in this area are investigated:

1. Observations of structure and chemistry changes of portland cement systems during the first 16 h of hydration.

2. Evolution of air-filled void system during the first 16 h of hydration.

3. The microstructural evolution in cement paste samples under different levels of stress during their first 60 h of hydration and its effects on stiffness and early age time-dependent strain of the samples.

The research presented in this dissertation is based on the work performed by the author at Oklahoma State University. The chapters in the dissertation are written in journal paper format for easy submission.

CHAPTER II

MULTI-SCALE IN-SITU OBSERVATIONS OF STRUCTURE AND CHEMISTRY CHANGES OF PORTLAND CEMENT SYSTEMS DURING HYDRATION

Abstract

There is little agreement about the mechanisms or direct measurements of the transition of cement paste from a slurry to a solid. This chapter uses five different in-situ X-ray imaging at multiple length scales (from 15.6 nm to 1 μm) to follow the three dimensional microstructural evolution of portland cement, and monoclinic tricalcium silicate paste over the first 16 h of hydration. Measurements of over 60,000 particles in industrially relevant water-to-solids ratios (w/s) captured every 10 min were made at the micron scale. Nanoscale examinations of the structure and chemistry are used to support this work. The results show that hydration products with an average Ca/Si > 3 form on and near the surface of the hydrating particles that appear to control the reaction rate. These hydration products appear to change in chemistry right as more rapid dissolution and formation of hydration products during the acceleration period. A mechanism is proposed that uses these observations to explain the different rates of reaction that describe how concrete stiffens and gains strengths.

Keywords: X-ray Computed Tomography; Cement Hydration, Acceleration Period; Calorimetry; Induction Period

2-1-Introduction

Currently, there is little understanding about the mechanisms that govern the transition of portland cement or C_3S[2] paste from a slurry to a solid. This change occurs between what is known as the induction and acceleration period [2, 34-39]. Improved knowledge of this process would allow for better control over cementitious materials and improved usage of both chemical and mineral admixtures. This would allow for improvements in the economy, constructability, and sustainability for concrete, the most commonly used building material in the world.

Several hypotheses have been proposed in the literature to explain the initial dissolution of cement particles and the subsequent formation of the microstructure. Some suggest that a hydrated layer forms at the particle surface that reduces the accessibility to the surrounding solution and then this material subsequently disappears [34, 35, 38]. More recent publications have focused on the localized formation of etch pits or more uniform dissolution, depending on the calcium concentration within solution [37, 40, 41], and others hypothesize that early hydration products form within these etch pits that may slow the release of ions and control the local dissolution of the anhydrous particle by covering the most reactive sites [3, 42, 43].

Previous work studying changes in the solution chemistry during the first 4 h of hydration of C_3S with w/s from 0.70 to 20 shows that the Si concentration is low (between 1 μmol/L and 4.5 μmol/L for w/s = 0.70) while the Ca in solution increases over time and reaches a maximum (≈ 1700 mg/L for w/s = 0.70) near the end of the induction period [44]. After reaching a maximum value the Ca begins to decrease and the Si concentration begins to slightly increase. At this same time the heat given off by the reaction begins to increase [37, 45, 46]. It is not clear what causes this observation but it has been proposed to be caused by rapid dissolution of C_3S [2, 37, 45].

[2] Conventional cement chemistry notation is used throughout this dissertation: C = CaO, S = SiO_2, H = H_2O.

Unfortunately, these measurements only examined the average ionic concentration in the solution and no information is obtained about the change in microstructure for these periods.

Many hydration studies use bulk measurements to study the process and so they cannot provide detailed measurements of the individual particles during the reactions. Some of these techniques include isothermal calorimetry, chemical shrinkage, pore solution analysis, quasi-elastic neutron scattering (QENS), and nuclear magnetic resonance (NMR) [2, 6-13]. Imaging has been used to make complementary observations of the evolution of the microstructure over time. This is typically done with scanning electron microscopy (SEM) or transmission electron microscopy (TEM) on samples where hydration has been arrested [14-17]. In order to examine these samples with these techniques the hydration must be stopped. This is typically done by using isopropyl alcohol or other solvents to remove the water through solvent exchange followed by drying [47-50]. These samples are then cast into epoxy and polished or fractured and a surface is investigated. This process has the potential to introduce artifacts [15, 16, 42, 48, 49, 51]. If an in-situ technique could be used to study this process then more insights may be able to be gained.

One important study used a single particle of C_3S with w/s = 2. Hydration was arrested on three different samples with acetone after 5min, 30 min, and 60 min [51]. The selected times corresponded to the initial reaction, the induction period, and the onset of the acceleration period in the calorimetry curve. After arresting hydration, the sample was broken and investigated by SEM. The authors observed a non-uniform layer of hydration product around the original particle which grew in thickness in the induction period and then shrank at the onset of the acceleration period. Poorly crystalized CH precipitates were observed at the end of the induction period that dissipated during the acceleration period. This observation aligns well with some other publications that suggested the formation of CH is an important parameter in the transition from the induction period to the acceleration period [46, 52, 53]. Despite these important observations this paper is rarely discussed in the literature. One possible reason is that the quality of the SEM

images was poor, there was no chemical analysis to support their claims, and there may have been concerns over the high w/s and the use of acetone to arrest hydration.

Some in-situ imaging has been done by using soft X-ray transmission imaging to collect time-lapse transmission images while C_3S reacts at a w/s = 5 [54]. These images suggest that the hydration process is not limited to the surface of the C_3S particle and can occur inside the particle as well. However, if the transmission path of the X-rays is too long (> 10 μm for anhydrous C_3S), then there will be insufficient transmission of X-rays. Higher energy X-ray imaging techniques, such as laboratory and synchrotron X-ray Computed Tomography (XCT) allows for more than an order of magnitude higher penetration. This can allow 3D microstructural data to be obtained non-destructively from the micron to nanometer length scale for thick samples [19, 20, 55-61].

Recent work has combined nano-tomography and nano-X-ray fluorescence with a technique called nano-tomography assisted chemical correlation (nTACCo) that is used to observe early particle dissolution and subsequent hydration products with a resolution of 50 nm [27, 62]. This technique provides quantitative measurements of 3D structure, chemical composition, and mass density of the hydration products. These experiments yield important observations of the changes in structure and chemistry but these observations have not been made continuously or in industrially relevant w/s.

More in-situ observations are needed of cement particles as they react at industrially relevant w/s. However, the acquisition time for typical XCT is several hours and there will be artifacts created if there is movement. Because of this, XCT is a challenging technique to use to study in-situ early age hydration reactions and often requires the reactions to be first arrested in order to be studied [29, 30]. Fortunately, recent developments in fast data acquisition rates from high-flux synchrotron sources have made it possible to collect 3D data at the micron scale in a few seconds

[29-33, 63]. This technique is named fast computed tomography (fCT). This reduction in acquisition time makes this technique useful for studying early cement hydration.

In this chapter, five different types of X-ray imaging techniques are used to study hydration of portland cement related powders at different length scales. These include fCT, Transmission X-ray Microscopy (TXM), and Nano Computed Tomography (nCT) at multiple length scales. In addition, SEM with Energy-Dispersive X-ray Spectroscopy (EDS) and Nano X-ray Fluorescence (nXRF) were used to evaluate compositional changes of some samples before and after hydration. The focus of this work is to find greater insights into the mechanisms that control the change from the induction to the acceleration period in both C_3S and portland cement hydration.

2-2-Method and Experiment

2-2-1-Materials

Cementitious materials used for the tests were NIST cement number 168 from the Cement and Concrete Reference Laboratory (Frederick, Maryland) (OPC) [64], and monoclinic C_3S (mC_3S). The mC_3S samples were produced by Mineral Research Processing (Meyzieu, France). These materials were investigated by ASTM C114 test method, automated scanning electron microscopy (ASEM), XRD analysis, isothermal calorimetry, and Blaine fineness (ASTM C204).

The specifications and bulk chemical composition of the investigated materials are presented in Table 2-1. The experimental details are included in the appendix A. According to ASEM and Blaine fineness, OPC was slightly finer than mC_3S.

XRD analysis demonstrates that mC_3S powder is close to pure C_3S. XRD analysis of OPC powder can be found in another publication [64]. Isothermal calorimetry results are presented in Figure 2-1 for five different mixtures. These mixtures match the conditions of the imaging

experiments in this chapter. One sample used w/s = 5. Some sedimentation may happen in this sample during the calorimetry test; however, the results provide an average w/s that matches the experimental conditions.

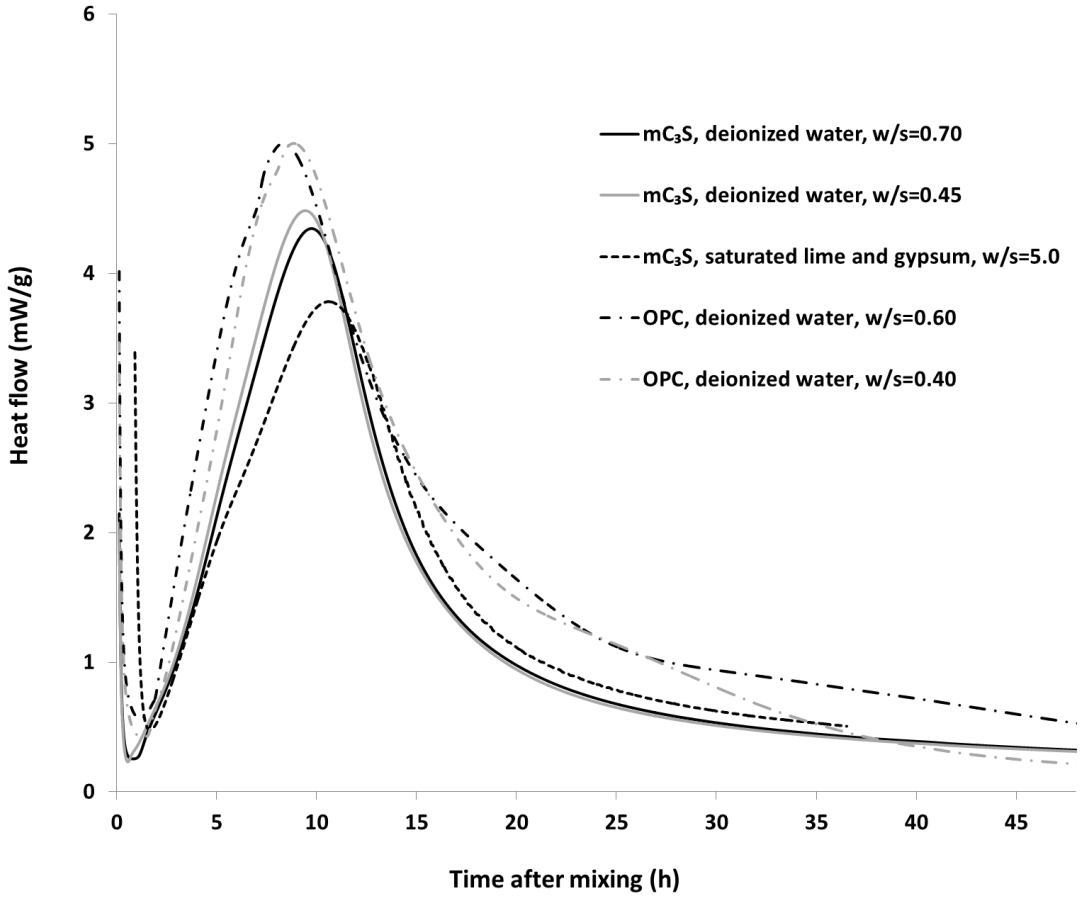

Fig. 2-1. Heat flow from isothermal calorimetry over time.

Table 2-1. Specifications and chemical composition of binders.

	Blaine (cm^2/g)	BET surface area (m^2/g)	Density (gr/cm^3)	Chemical Composition (%)						Phase concentration (%)			
				SiO_2	CaO	Al_2O_3	MgO	Fe_2O_3	SO_3	C_3S	C_2S	C_3A	C_4AF
OPC	4080	NA	3.15	19.91	62.27	5.11	3.87	2.15	3.49	54.5	15.7	8.0	7.0
mC_3S	3588	0.86	3.12	26.54	71.97	0.94	0.06	0.48	-	≈100	-	-	-

2-2-2- Examination of Pastes

2-2-2-1-Sample Preparation and Instruments Setting

Four paste samples were examined at industrially relevant w/s with 1 μm/pixel spatial resolution with fCT. These experiments were conducted at beamline 2-BM at the Advanced Photon Source (APS) at Argonne National Laboratory. The instrument details can be found in Table 2-2. More details about the facility can be found in other publications [31, 32].

Table 2-2. Instruments settings for fCT, TXM, SEM, and EDS experiments.

fCT	Resolution		1 μm/pixel
	Source energy		30 keV
	Total scan time		5 s
	Number of projections		1500
	angular increments		0.125°
	projection dimensions		2016×1536 pixel×pixel
TXM[a]	Resolution		241 nm/pixel
	Exposure time		50 s
	Source energy		40 keV
	Power		10 W
	Current		250 μA
nCT	Resolution		15, 65, and 130 nm/pixel
	Source energy		5.3 and 8.3 keV
	Dynamic range[b]	Min	0
		max	65,536
SEM[c]	Accelerating voltage		~20 keV
	Filament drive		71.6%
	Emission current		~55 μA
	Brightness		-15%
	Contrast		90%
	Working distance		17 to 18 mm
EDS	Minimum counts per second		3500
	Live time (acquisition time)		5 sec
nXRF	Resolution		50 nm/pixel
	Detector dwelling time		0.1 s
	Scaler count time		0.1 s

[a] radiographs from this test are used
[b] data are displayed in FLOAT type
[c] backscattered imaging mode under vacuum condition

As reported in Table 2-3, four different paste samples were investigated. Dry powders were also investigated to aid in the segmentation of the data sets. This will be discussed later in the chapter.

Table 2-3. Properties of samples and scan times for fCT test.

Cementitious material	w/s	Time for first tomograph (minutes)	Time for last tomograph (hours: minutes)
mC_3S	0.70	70	15:40
mC_3S	0.45	70	15:40
OPC	0.60	34	11:34
OPC	0.40	34	11:34
mC_3S powder	-	-	-
OPC powder	-	-	-

Samples were prepared with 5 g of powder and the necessary water to reach the desired w/s. Two different w/s (one lower and one higher) were used because it was important to make a sample that was well compacted and to investigate the differences in performance. The mixing and sample preparation are discussed in the appendix A.

2-2-2-2-Overview of fCT and XCT

Sample alignment took between 34 and 70 min. After alignment, 3D tomographs were collected every 10 min. Figure 2-2 shows the 3D tomograph and a typical slice from the mC_3S sample with w/s = 0.70. The gray values in the XCT and fCT datasets correlate to the x-ray absorption of the material. Therefore, a change in gray value for a given location could be attributed to the difference in chemistry, density or both. These gray values allow the data to be separated into different constituents and then quantitatively evaluated. This process is called segmentation. A segmented or binary image showing the material with high X-ray absorption is shown in the lower right of Figure 2-2. The steps used to create this image will be discussed in the next section.

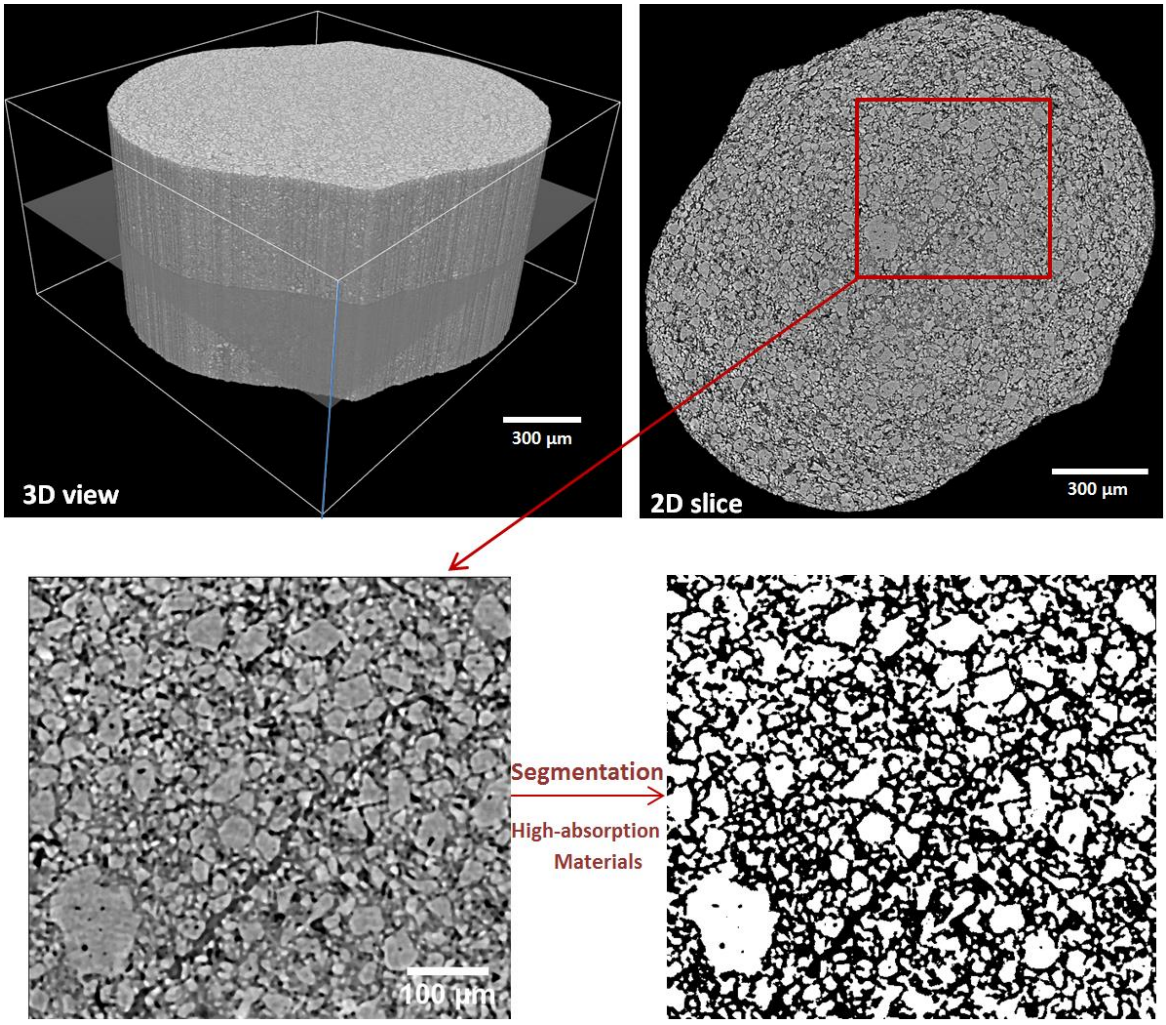

Fig. 2-2. Examples of 3D model, a 2D slice, and a region before and after segmentation of high-absorption materials from mC_3S paste with w/s = 0.70.

2-2-2-3-Image Processing

First, a median filter (radius of 2.5 µm) was used to remove noise from the images. This popular filter is used to preserve image edges with minimal signal distortion [65, 66]. It is common to choose different ranges of gray values to separate the different materials for data processing. To help guide this decision, the dry powder was scanned and the bulk density was measured. By using the bulk density and the volume of the container, the volume of the powder could be calculated. Once the volume of powder was known, different threshold values could be chosen

and the volume could be estimated and compared to the calculated volume of powder. The calculated threshold value is applied to all collected tomographs and the single voxel regions were removed from the data as they are at the spatial limit of the method and therefore treated like noise.

For this work, it was convenient to separate the data into low and high X-ray absorption material due to the high X-ray energy level in fCT measurements. The low-absorption material consists of voids, water filled space, mixtures of water and small anhydrous particles, and low density hydration products. The high-absorption material consists of everything else including anhydrous cement and some hydration products close to the surface of the anhydrous cement grains.

A limited region of the sample that is 1000 μm in diameter by 100 μm in height was used for the analysis. This region was used to reduce the computational expense and also to avoid beam hardening artifacts that may occur near the edges. This allowed over 60,000 particles to be investigated from each sample in the region of interest. These same settings were then used to segment the high-absorption material in the slurry scans. Figure 2-2 shows a region of a cross section both before and after the segmentation of high-absorption materials.

These same settings were used on the slurry scans. While these samples contain water, this should have minimal impact on the measured gray values as water has a low X-ray absorption and so this should not affect the X-ray attenuation. In medical CT scans it is common to use a fixed range of gray values for segmentation regardless of the surrounding fluid [23]. The sensitivity of the results of the segmentation was investigated by altering the segmentation values by ±2.5% of the calculated threshold value. These differences were chosen based on the expected variation that may occur from the bulk density calculation of the powder. Over this range of values the same trends were observed and the magnitude of the changes only slightly changed. Therefore, the selected segmentation method seems reliable for this study. This is discussed in more detail later

in the chapter. More details about segmentation and quantification can be found in the appendix A.

2-2-3- Examination of Individual Particles

A collection of particles was investigated with other imaging techniques at higher resolutions to complement the fCT data. These particles were epoxied to the end of a graphite rod and then allowed to react in higher w/s solutions. These more dilute solutions were used so that the *in-situ* reactions of the particles could be imaged. Reactions of cement particles in dilute solutions is reported to be quite rapid because of the undersaturation of the solution surrounding the particles [67]. To address this, the particles were immersed in 15 mM lime or saturated lime and gypsum solutions. These solutions were shown to have heat evolution curves comparable to suspensions with w/s from 0.5 up to 5.0 [34, 67]. The heat flow curves shown in Figure 2-1 also confirm this. TXM and nCT are used to investigate the microstructure change of the reacting particles, while SEM/EDS and nXRF are conducted to obtain chemical information of individual particles.

2-2-3-1- TXM

Radiographs were used to take in-situ projections of a few OPC particles epoxied to a graphite rod as they reacted at w/s = 10 in 15 mM lime solution. This allowed data complementary to the fCT to be gathered at a finer length scale (0.241 μm versus 1 μm). Figure 2-3 shows the experimental setup.

The rod was placed in a polyethylene tube and 15 mM lime solution and additional OPC particles were placed inside the container so that w/s = 10. All the testing was done in a N_2 environment to minimize carbonation. The tube was then capped with clay to prevent moisture loss and air

penetration. Radiographs were taken every 50 s over 2 h with a spatial resolution of 0.241 μm/pixel. The scan was performed with a Zeiss Xradia 410 Versa machine. Details of the settings can be found in Table 2-2.

The gray value in TXM datasets correlates to the transmitted X-ray intensity (I), which is a function of the mass attenuation coefficient (μ_m), density of material, and path length (x) according to the following equation:

$$\frac{I}{I_o} = \exp(-\mu_m \rho x) \qquad (2\text{-}1)$$

where I_0 is the original intensity of the X-ray beam, μ_m is the mass attenuation coefficient, ρ is density, and x path length [45]. The mass attenuation coefficient is a function of chemistry and density of the materials studied, and the energy level of the X-rays [68].

Unlike the tomography data, the most absorbent phases in a radiograph are dark and the solution filled space is light. The gray value in the radiograph is not only determined by the chemistry and density of the material but also related to the geometric length along the projection. In general, a radiograph is not as sensitive as a tomograph to detect the presence of the high absorption-material. However, it is still useful to provide supporting evidence. An Otsu segmentation method was used to find the high-absorption materials in the radiographs [69]. A constant threshold value was used to segment the high-absorption material for the time-series radiographs.

This experiment was repeated 12 times to investigate particles greater than 20 μm. Each experiment was investigated for up to 15 h and the increase of high-absorption materials was only observed in *one* of these particles. It is possible that this increase in high-absorption material occurred in other particles but the changes were not detectable by the technique at this w/s because they occurred too quickly to be imaged, or they occurred so close to the particle surface that they were not able to be detected. Another possibility is that the change may not be

significant enough to be consistently detected. Since the gray value in a transmission image is a function of the X-ray path length, the material investigated has to have enough mass to be detected in the transmission image. This means that the changes would need to occur over a large enough volume for the changes to be observed with this method. This makes the TXM less sensitive to this phenomenon. Despite the technique being less sensitive it still provides helpful insights.

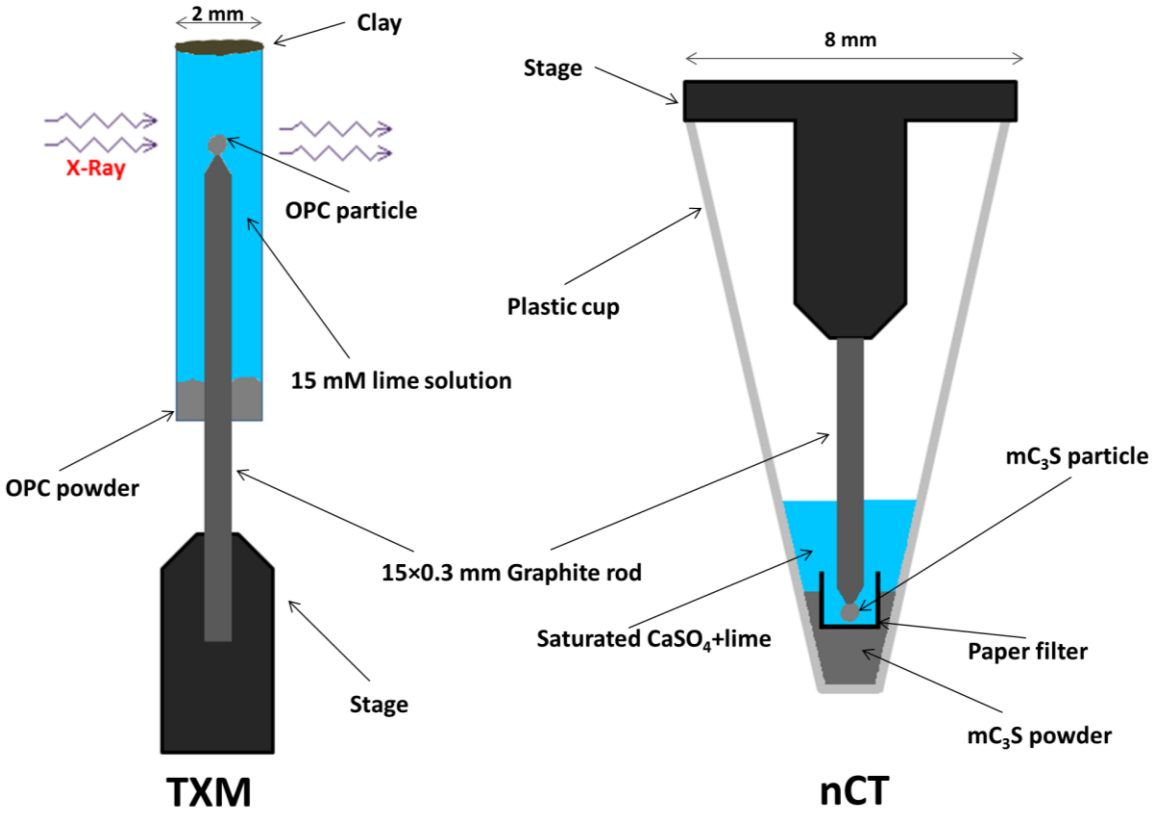

Fig. 2-3. Details of TXM and nCT experiments.

2-2-3-2- nCT

A 3D tomograph was acquired at nano scale resolution both before and after a certain period of reaction. The measurements were made using an UltraXRM-200 with an X-ray energy 8.3 keV at a resolution of 130 nm/pixel and with an Ultra 810 with an X-ray energy of 5.3 keV at 65 nm and

15 nm/pixel. The details of the instruments can be found in Table 2-2. The UltraXRM-200 was used to investigate the 10 h anhydrous sample. The lower X-ray energy levels of these imaging methods provide higher contrast to the X-ray absorption of the hydration products. This gives more insights to the hydration products which may not be able to be observed with the higher energy imaging methods such as fCT and TXM.

Two samples with a collection of particles on the tip of a graphite rod were investigated for hydration period of 2 h and 10 h with w/s = 5 in saturated lime and gypsum solution as shown in Figure 2-3. Both samples were imaged before and after reaction in order to compare their changes with their initial state. After the initial scan the sample was placed in a N_2 environment and then added to a sealed cell for the reaction. The cell was stored in the N_2 environment to protect it from carbonation as it hydrated. The reactions were then arrested by 99% isopropyl alcohol after the desired amount of hydration at the desired time and the sample was scanned again with nCT.

A computer algorithm for 3D image registration was created to align the two scans [19, 27]. A qualitative segmentation of the anhydrous C_3S and hydration product were completed by choosing gray values that adequately separated the materials and minimized background noise. The threshold values for anhydrous C_3S were chosen to match the border of the sample as found by the nXRF scans. Since the nXRF shows high contrast between material that is air and solid then this was useful to compare the data sets. This has been successfully used in the past [62].

2-2-3-3-Changes in Chemistry

2-2-3-3-1-SEM/EDS

To learn more about the changes in the surface chemistry, OPC and mC_3S particles were examined by SEM/EDS analysis in the same orientations and locations both before and after

being placed in dilute 15 mM lime solution with w/s = 10 and then subsequently in isopropyl alcohol. The test condition is similar to the TXM experiment. A typical sample can be seen in Figure 2-4.

Since the goal of this work was to investigate the changes in the surface chemistry at known locations, no sample preparation or surface coatings were used. Because the sample surface was not flat and the surface was not coated, the analysis is only qualitative. Previous work has shown that this method of investigation showed agreement with nano X-ray Fluorescence of hydration products and so a validation of the procedure is not presented [62].

For this analysis several samples were investigated both before and after hydration for OPC and mC_3S. The samples were carefully aligned after reaction so that the same orientation and locations were investigated. Different samples were investigated after 5 min, 10 min, 20 min, and 36 min of hydration in 15 mM lime solution with w/s = 10. Points were only investigated if the Ca/Si was less than 4. This is done because points outside this range are not likely C_3S.

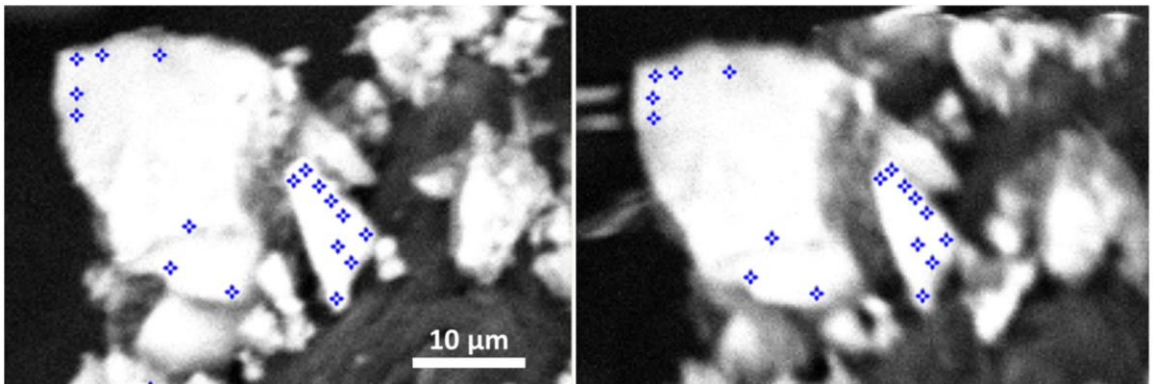

Fig. 2-4. Example of an OPC sample before hydration (left) and after 5 min of hydration (right), chemical compositions of several points (shown in blue) were obtained from SEM/EDS.

2-2-3-3-2- nXRF and nTACCo

The chemical composition of the reacted particles in nCT were investigated with nXRF. In this technique, a primary X-ray beam illuminates the sample and x-ray fluorescence radiation leaving the sample is detected with a four-element silicon drift diode detector that is perpendicular to the X-ray beam direction (Vortex ME4) [70]. Each element is characterized by its characteristic emitted fluorescence radiation. The collected X-ray fluorescence data were analyzed using the software package MAPS [71]. Also, fitting and quantification of the fluorescence data were completed with thin-film standards (National Bureau of Standards, Standard Reference Material 1832 and 1833). As an additional standard material, an anhydrous C_3S particle was utilized to improve the accuracy of the analysis.

An area close to the detector (less than 4 μm from the edge) was carefully selected to reduce the travel path of X-rays and so minimize the artifacts created by X-ray absorption. The measurements were conducted with an X-ray spot size smaller than 50 nm at the hard X-ray nano-probe beamline at sector ID-26 of the Advanced Photon Source (APS) and the Center of Nanoscale Materials (CNM) at Argonne National Laboratory. The instrument details are provided in Table 2-2. Additional details can be found in other publications [27, 70].

Nano-tomography assisted chemical correlation (nTACCo) is a technique that can combine nCT and nXRF data. By fusing the 3D structure information into the 2D chemical mapping, the chemistry information as elemental density with unit of g/cm^3 can be measured for intermixed phases at nano-length scale. First, the coordinate systems of nCT and nXRF datasets were aligned by matching the orientation using radiograph images from nCT with the Ca map from nXRF. The details of this procedure are given in previous publications [19, 27, 62]. Next, a region that was known to be more than 90% anhydrous C_3S was used to solve for the elemental density of anhydrous C_3S. Since the 3D geometry of the sample was well known from the nCT data and the

chemical density was well established for the C_3S this information could be combined to find the chemical density of the hydration products. Excessive values with Ca/Si >10 are excluded from the analysis as they are likely CH.

2-3-Results

2-3-1- Paste Samples

2-3-1-1- Changes in High-Absorption Material

Figure 2-5 illustrates the changes of the volume of high-absorption materials during hydration. These measurements are based on the volume of more than 60,000 particles. Since it took time to align the samples there are no tomography data for the early age hydration of the pastes. The theoretical volumes of the high-absorption materials for the OPC and mC_3S samples at time zero were calculated based on the known w/s, particle densities, and an assumed air content of 2%. These values are shown at time zero on the graph. Lines of interpolation are shown in a lighter color to connect the estimated initial values of high-absorption to the first measured value.

In all samples, the volume of the high-absorption materials continuously increased and reached a maximum value and then decreased and did not change. The initial increase was not observed in mC_3S with w/s = 0.45; however, this behavior could have occurred prior to the first tomograph at 70 min. It should be noted that the measured maximum volume of high-absorption materials was higher than the estimated volumes of the anhydrous powder at the time of mixing. The increase was higher for pastes with higher w/s.

The shape of the curve is similar for all four samples. This repeat behavior by different samples and materials suggests that there must be a repeatable event in the hydration of both mC_3S and portland cement and is not an anomaly. Furthermore, the observed changes are several times

higher than the variation after 5 h when the data is not changing. This suggests that these changes observed in the first 5 h of hydration are significant.

To examine the sensitivity of these measurements the gray values used for segmentation the gray value threshold values for mC_3S paste with w/s = 0.70 were varied by ±2.5%. The results are shown in Figure 2-6. The change in the threshold value seems to have a one-to-one correlation with the measured volume. While these changes did impact the magnitude of the measured values, they do not change the trend and timing of the curves. Therefore, the segmentation procedure seems to be robust enough for the conclusions drawn.

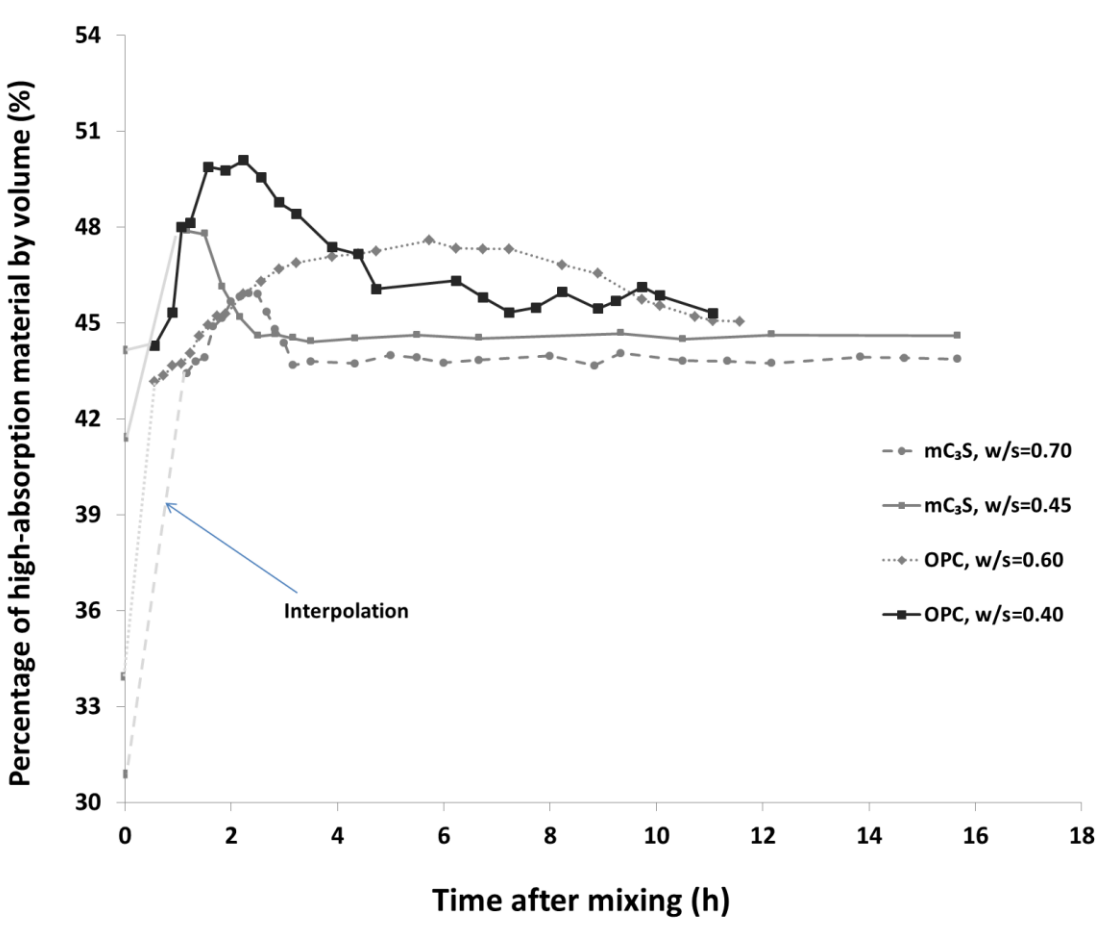

Fig. 2-5. Volume change of high-absorption material versus time after mixing.

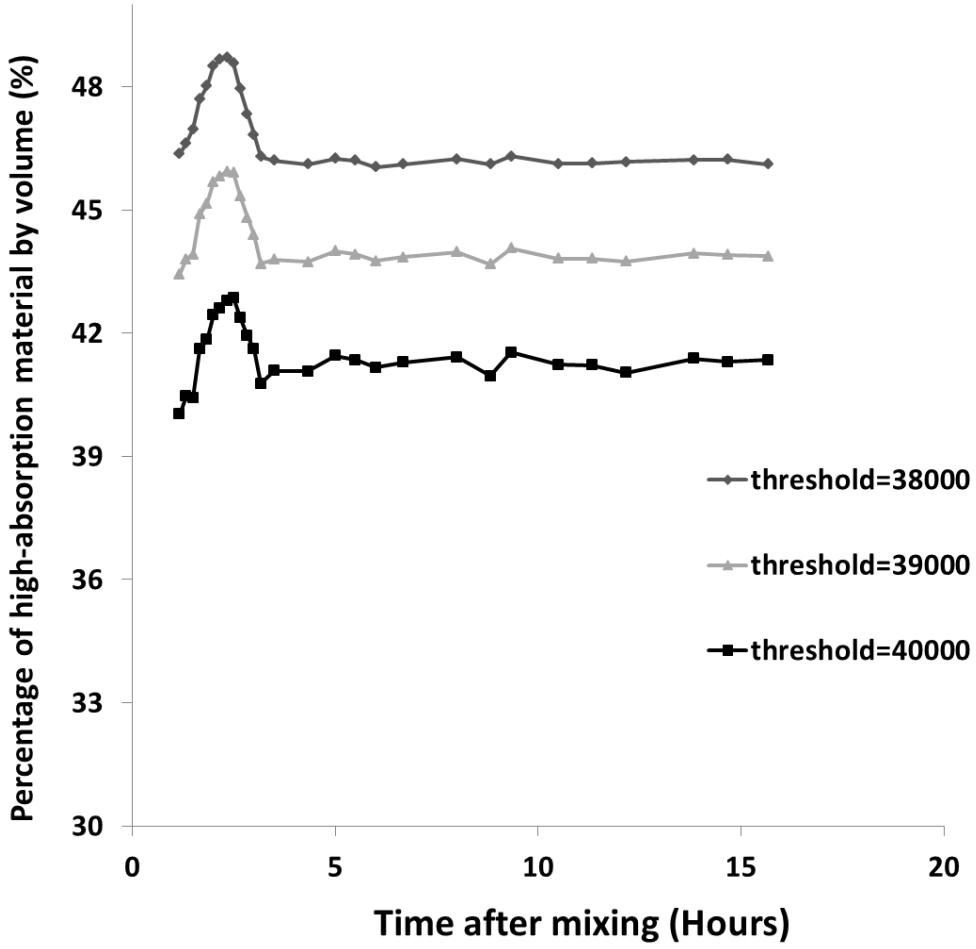

Fig. 2-6. Effect of threshold gray value on the trend of the hydration curves for mC_3S at w/s = 0.70. A threshold value of 39000 was chosen based on the segmentation method.

Figure 2-7 shows the isothermal calorimetry and the percentage of high-absorption material on the same plot. Since the preparation of the paste samples for fCT uses the same procedure as calorimetry experiment, these results from two different experiments should be comparable and provide insight into correlations between the microstructure changes and the rate of reaction.

The increase in the high-absorption material appears to closely match the beginning of the acceleration period. Others have suggested that hydration products begin forming as soon as solution is introduced to anhydrous particles [44, 46, 51]. If these hydration products form on the

surface of the original high-absorption material then this could explain why the material is observed to increase in size.

The decrease in the high-absorption material occurs at the beginning of the acceleration period. This suggests that high-absorption material that is forming is decreasing in volume over time. This could occur if the products are not stable. This also may occur if the local solution chemistry changes enough to cause these hydration products to dissolve or transform to another phase with different chemistry. The high-absorption material stays almost constant as the acceleration period continues; however, the calorimetry curves suggest the rates of reaction are still high. The OPC system has a greater volume increase as well as heat release than the mC_3S powder. This may occur because of the lower w/s, particle size distribution, differences in chemistry, and the simultaneous formation of multiple hydration products. While bulk observations of the change in high-absorption material are useful, investigation of individual particles could provide more insight to what is occurring.

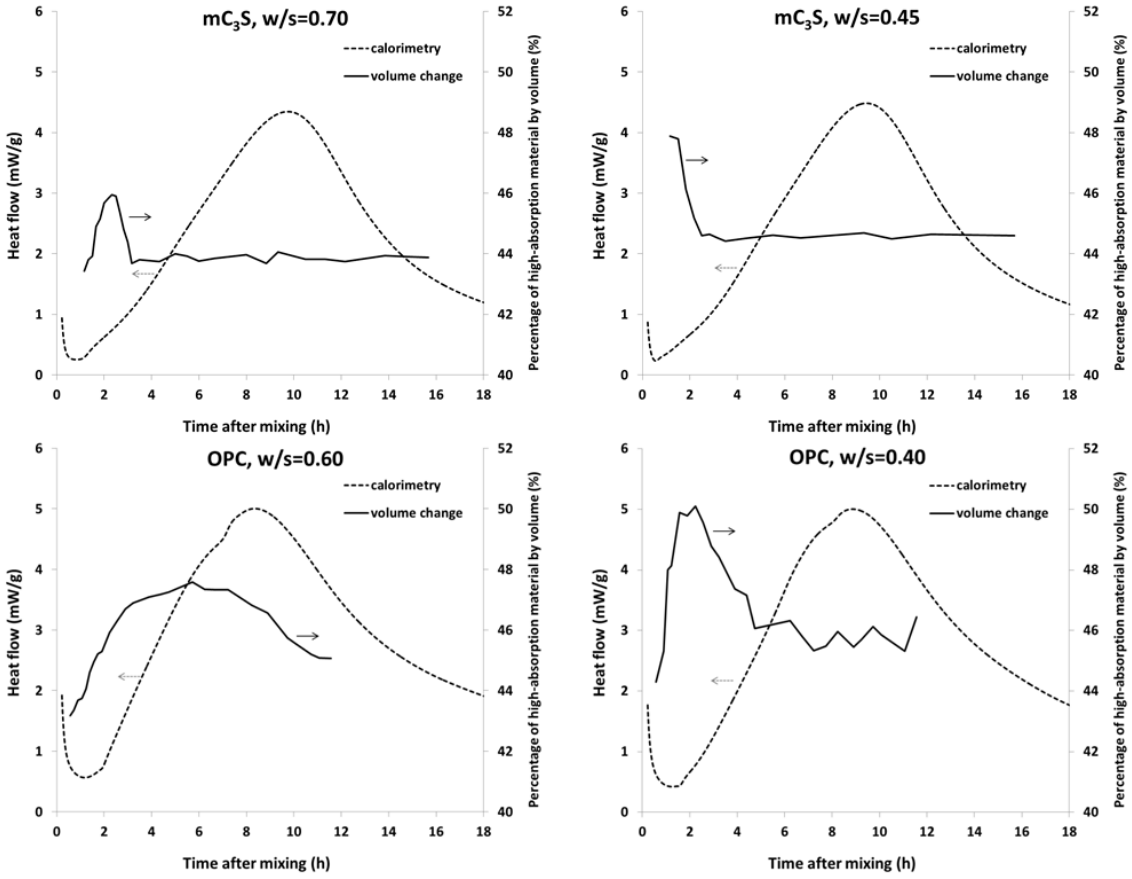

Fig. 2-7. Comparison of isothermal calorimetry to volume change of high-absorption material from fCT.

2-3-1-2- Volume Change of Individual High-Absorption Material

Single mC_3S and OPC particles were investigated to determine how particles of different sizes change over time. These particles were found by investigating the sample and finding particles that could be isolated and therefore easier to follow. The particles were categorized into three size ranges according to their average diameters. A summary of the data is shown in Table 2-4. Since small particles were shown to react rapidly, it was not possible to investigate particles smaller than 8 μm.

Table 2-4. Details of sample individual particles within pastes.

Paste type	Average diameter (μm)	Number of individual particles observed
OPC, w/s=0.40	8-20	13
	20-40	13
	40-60	11
mC_3S, w/s=0.70	8-20	11
	20-40	11
	40-60	10

Figure 2-8 shows the volume change of high-absorption materials of individual particles with respect to their volume in the first collected tomograph (70 min for mC_3S and 34 min for OPC). The absolute volume change was calculated by subtracting the volume of the particle at the target time period from the volume of the particle in the first measurement. Also, the percentage change was calculated by normalizing the absolute volume change to the initial volume of the particle. Each point shows the average volume change of the investigated particles. One standard error (SE) of the mean is also reported in the graphs. The standard error depends on both sample size and standard deviation and is useful to calculate a confidence interval around the mean [72]. The variations for the larger particles are wide because there was a large difference in the starting diameters of these particles. Despite this high variation the averages show that there are different performances of different sized particles.

The following observations can be made based on the graphs:

- All particles, except the smallest group in the mC_3S sample, had an increase in volume of high-absorption materials followed by a decrease.

- The volume percentage change of high-absorption materials in smaller particles was higher than for the larger ones over the period of the test.
- Absolute volume of high-absorption materials in the larger particles changed more than smaller particles.

The general performance of the individual particles was in accordance with the trends of the total particle volume except that a maximum value was not observed in the smallest particles of OPC. It is possible that the maximum observed high-absorption volume could have occurred before the first collected data set for this sample.

After the initial volume change, the larger particles seem to have negligible change in volume while the smaller particles are monotonically decreasing in volume. Since the smaller particles have a higher surface/volume ratio this would promote more rapid dissolution. Also, the larger surface area of the larger particles make them more likely to serve as points of nucleation and therefore appear to grow in size [73].

These results provide insights as to why the volume percentage change of high-absorption material can be almost constant while the calorimetry results suggest that there is continued reaction. First, the particles that are smaller than 8 μm that are not included in the analysis but likely continue to dissolve. Since the large particles account for the majority of the volume of the paste their behavior will govern the observed volume changes.

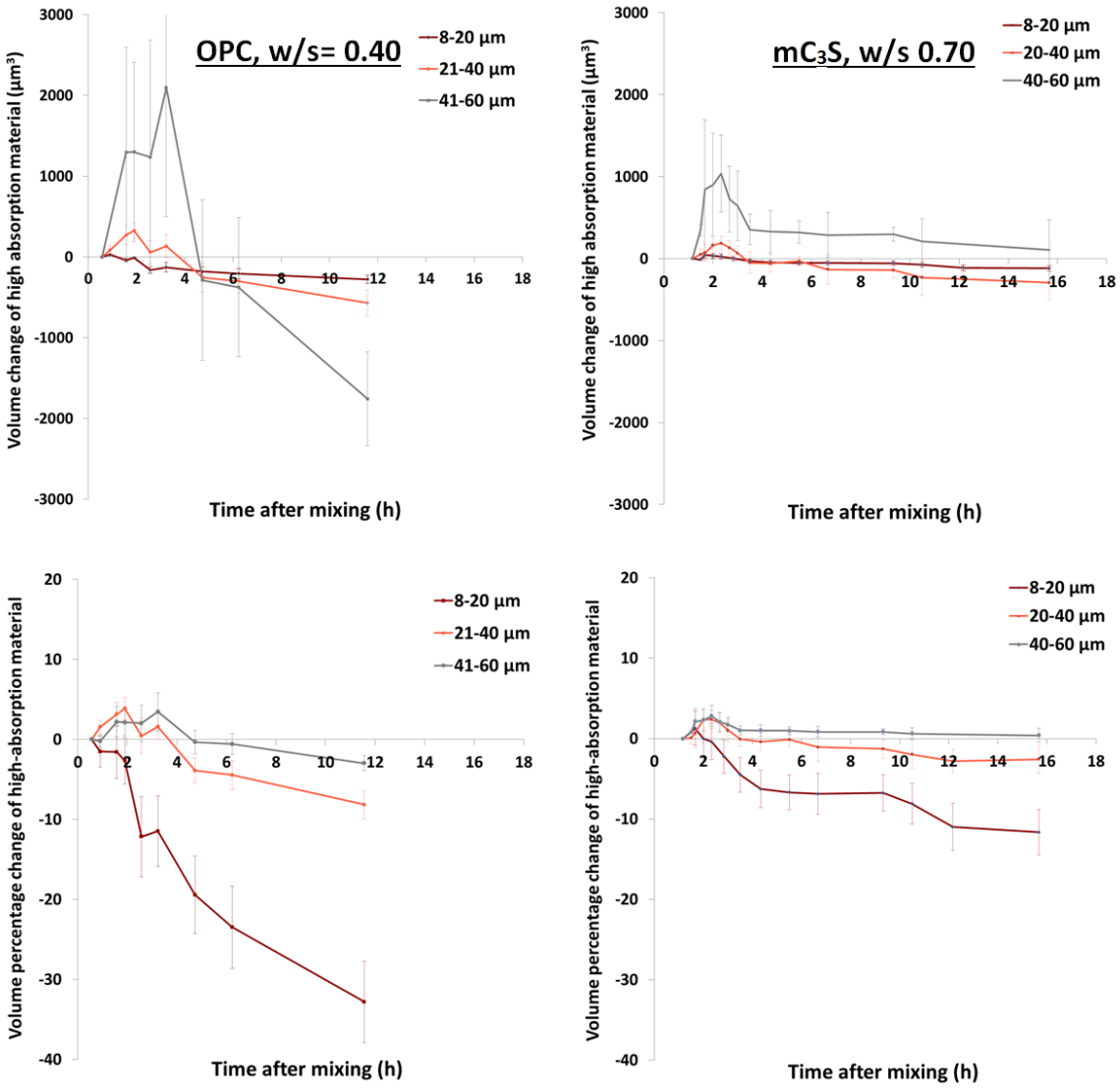

Fig. 2-8. Percentage and absolute volume change in individual high-absorption particles with respect to the initial volume at 34 min for OPC and 70 min for mC_3S pastes.

Three dimensional reconstructions of three mC_3S particles at w/s = 0.70 in different size ranges are shown in Figure 2-9. The volume of high-absorption material and average diameter are also reported. The particles are shown at the first measurement and then at different time periods that match critical times in hydration as suggested by the calorimetry curve. Regions that appear to have decreased X-ray absorption when compared to the earliest tomograph are shown in green. These regions are regions where part of the anhydrous particle is no longer detected. This space

may now be filled with fluid and/or low absorption hydration products. Also regions that appear to have increased X-ray absorption are shown in dark gray. The 3D renderings show that the regions near the surface of the anhydrous particles simultaneously increase and decrease in X-ray absorption. These regions of change seem to be found at only a few locations on the surface and do not occur uniformly. This could be attributed to higher crystallographic defects or mechanical damage as suggested in other publications [2, 3, 27, 36, 74-77]. This also shows that smaller high-absorption particles show more volume decrease and the larger particles show growth.

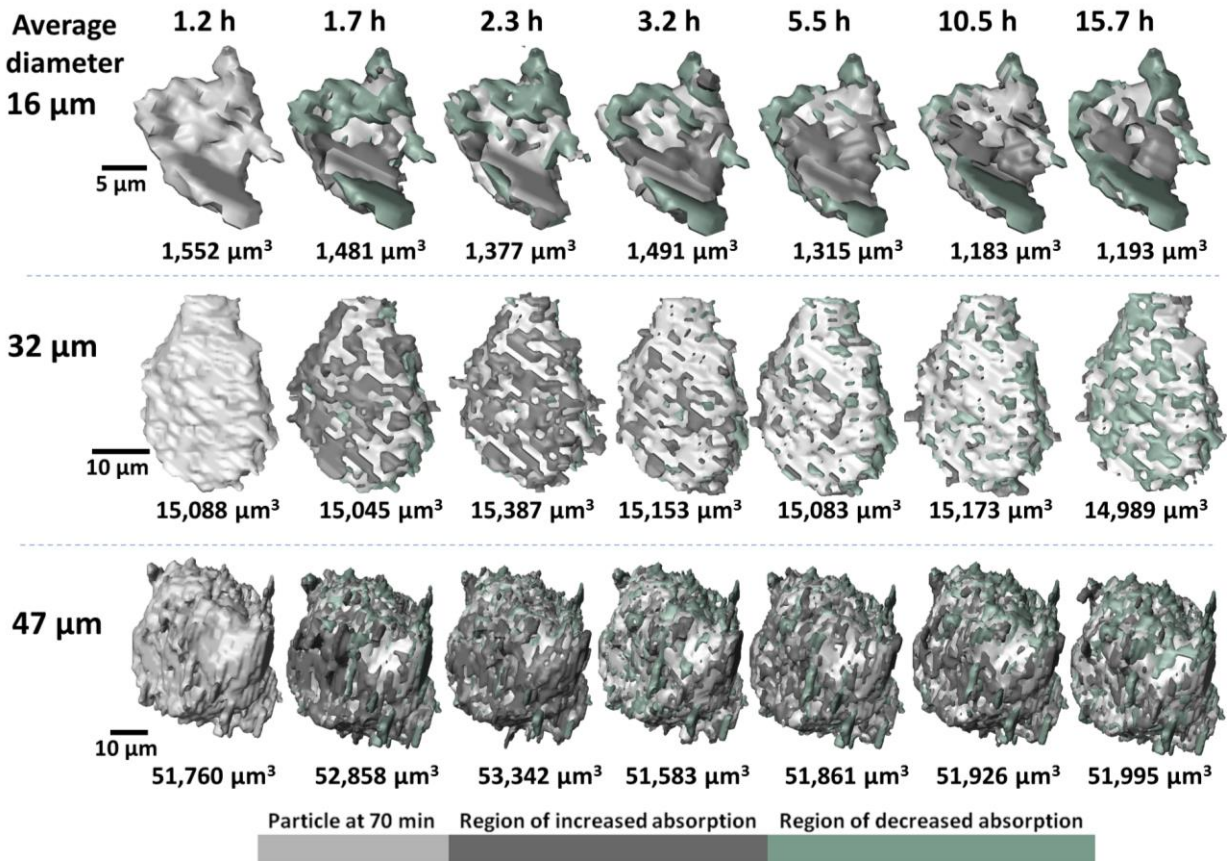

Fig. 2-9. Three Dimensional views of three mC_3S particles from different size ranges in critical time periods.

2-3-2- Complementary Experiments on Individual Particles

2-3-2-1- Microstructure Observations

2-3-2-1-1-TXM

The results from the TXM experiment with detectable changes are shown in Figure 2-10. The raw images are shown at the top of the image with the borders from the segmented images overlaid in the middle images. The lower plot shows the area change with time. Specific time periods are highlighted with a different color showing the border of the particles. These same colors are used in the area versus time plot to highlight when these images were captured. The raw measurements are shown by the jagged line and the smoothed line is a polynomial curve fit. The area change was similar to what was observed in the fCT data but over a shorter time period. This shows that a material of high X-ray absorption can be observed with a different in-situ imaging method. The difference in timing may be due to the differences in solution chemistry and the differences in the w/s.

The borders, defined by a constant threshold value, show that the change of the high-absorption material is not uniform around the particles. This non-uniform change around the OPC particle was also observed in the 3D observations of individual particles as shown in Figure 2-9. The irregular areas at the bottom of the particle had the most change. This could be caused by increased particle defects or a different crystal structure in these areas.

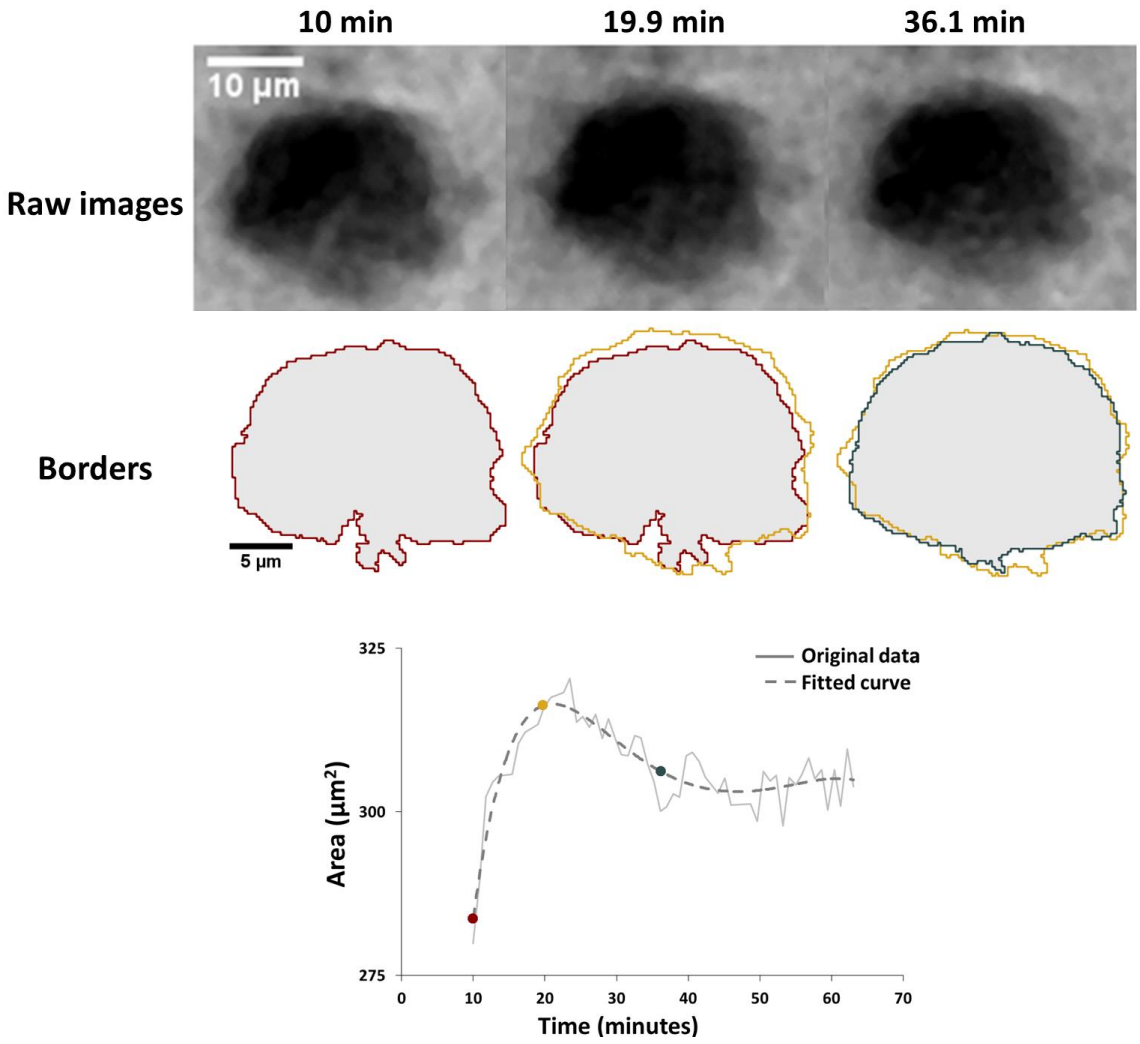

Fig. 2-10. Area change of high-absorption materials of OPC particle immersed in 15 mM lime solution at w/s = 10. The raw images are shown at the top, the overlaid borders are shown in the middle images, and then a graph of the area change over time is shown at the bottom.

2-3-2-1-2- nCT

The nCT results for a collection of mC_3S particles are shown in Figure 2-11 and Figure 2-12 for hydration periods of 2 h and 10 h. These periods show the evolution of the microstructure from the induction period to the end of the acceleration period. The slice images from three different

locations from both before and after hydration are labeled on the 3D model by dashed lines. The 3D models also show where hydration product has formed where it was not previously present.

The sample that has hydrated for 2 h shows that hydration product forms both directly on the surface of the particle and also extend over a micron away from the original particle. The hydration product that covers the surface of the anhydrous particle has a thickness between 60 nm to 100 nm. A product layer of this thickness would not be expected to be detected by the fCT experiments. However, the product that extends from the anhydrous particle surface could be detected. Furthermore, as particles hydrate in proximity to one another in lower w/s then this could create more extended product growth and be further detected. This has been observed in previous publications where collections of particles were observed in similar experiments [62].

It should also be noted that the observed product occurs on only certain local regions of the particle surface with other regions remaining almost unreacted. This non-uniform reaction of a pure anhydrous C_3S particle has been reported in previous publications to be caused by a high density or defects or different crystal structure [3, 27, 40-43].

After 10 h of hydration the isolated regions of hydration product that were observed at 2 h are no longer present. Instead, the sample shows a high degree of reaction with a decrease in the anhydrous boundary by as much as 1 μm. This change in the anhydrous particle dimensions will contribute to the decrease in high-absorption material observed in the fCT data.

Although the overall volume of the particle shows an increase in size from the formation of hydration product, if these products are made up of a hydration product with a low X-ray absorption then this may explain why they are not observed in the fCT dataset. This idea agrees with the observations of the individual particles in the fCT datasets shown in Figure 2-8. These observations show that particles that range in size from 8 to 20 μm show a significant decrease in the volume of high-absorption material at the end of the acceleration period. This could be

explained by the formed hydration product changing chemistry and/or structure over time. This will be addressed in more detail after discussing the chemistry of the hydration products.

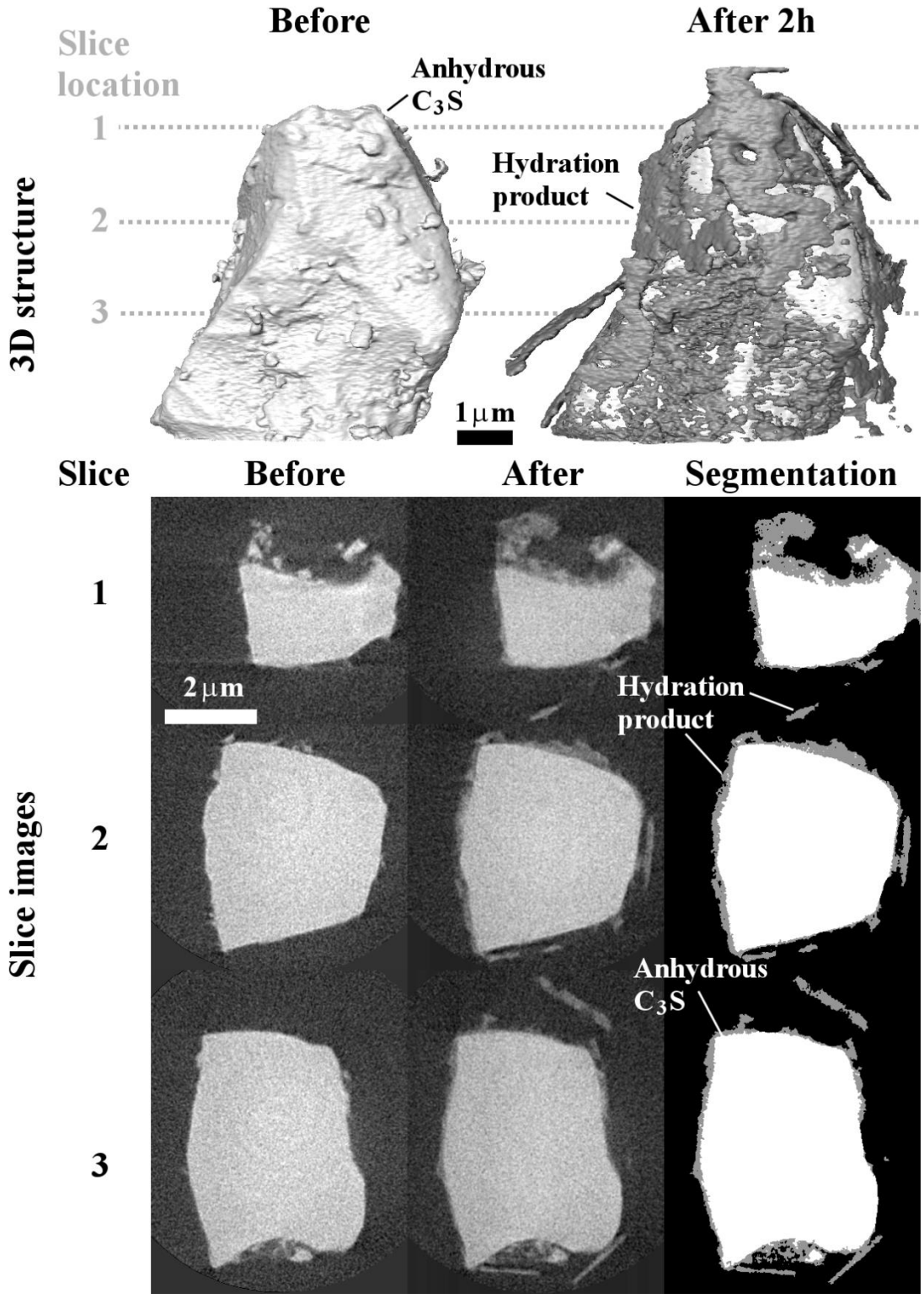

Fig. 2-11. The nCT dataset for a mC_3S particle showing 3D structure and three different cross sections before and after 2 h of hydration in saturated lime and gypsum solution.

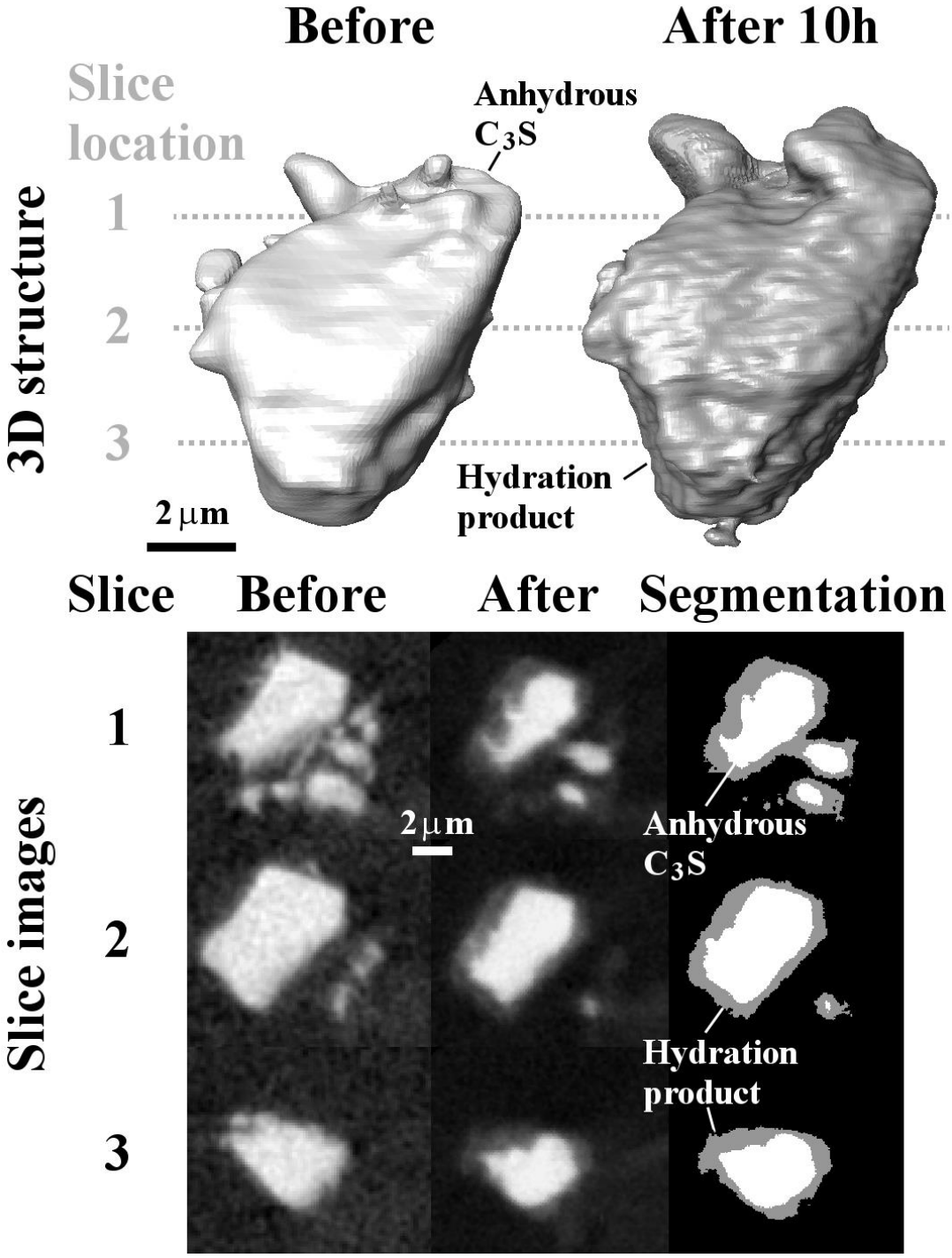

Fig. 2-12. The nCT dataset for a mC_3S particle showing 3D structure and three different cross sections before and after 10 h of hydration in saturated lime and gypsum solution.

2-3-2-2-Chemistry observations

2-3-2-2-1- SEM/EDS investigation

Analysis with SEM-EDS was used to provide a qualitative measurement of the chemistry of the surface materials. The method was first used to make repeated measurements on the surface of the anhydrous OPC and mC_3S particles to examine the repeatability of the method and obtain a baseline chemistry. Next several OPC and mC_3S particles were investigated both before and after hydration at 5 min, 10 min, 20 min, and 36 min in 15 mM lime solution with w/s = 10. These times and solution environment were chosen to complement the observation made by TXM experiment as shown in in Figure 2-10. As described in the methods the samples were carefully aligned before after reaction to measure the chemistry changes. The normalized percentage of Ca, Si, O, Fe, and Al both before and after hydration can be found in Table 2-5. The Ca/Si is used to provide additional insight and compare between other measurements. This ratio is used because this technique provides normalized elemental content and not actual concentrations.

Table 2-5. Average normalized percentages of the main components as measured by EDS analysis.

Powder type	Time		element %					Ca/Si	number of measurements
			Ca	Si	O	Al	Fe		
OPC	Anhydrous	mean	51.2	12.5	28.2	2.7	0.4	2.9	98
		SE*	0.8	0.2	0.9	0.4	0.1	0.0	
	Anhydrous Repeat	mean	50.4	12.7	26.7	7.0	0.8	2.8	31
		SE	0.9	0.3	1.2	0.7	0.2	0.1	
	5 min	mean	49.3	10.7	29.9	1.3	0.5	3.6	24
		SE	2.3	0.9	2.5	0.3	0.3	0.3	
	10 min	mean	60.1	11.9	22.1	1.5	0.7	3.6	14
		SE	3.4	0.4	3.4	0.3	0.3	0.2	
	20 min	mean	66.1	13.0	15.4	3.0	0.4	3.8	9
		SE	3.8	0.9	3.7	0.6	0.2	0.5	
	36 min	mean	51.8	11.4	31.1	1.4	0.5	3.3	20
		SE	2.3	0.6	1.8	0.3	0.2	0.2	
mC_3S	Anhydrous	mean	53.2	12.9	32.3	0.0	0.0	2.9	72
		SE	1.2	0.2	1.3	0.0	0.0	0.1	
	5 min	mean	51.3	13.0	33.7	0.0	0.0	2.9	27
		SE	2.1	0.5	2.1	0.0	0.0	0.2	
	10 min	mean	62.3	13.9	21.4	0.2	0.0	3.3	18
		SE	3.4	0.6	3.1	0.1	0.0	0.3	
	20 min	mean	54.3	12.2	31.2	0.0	0.0	3.4	15
		SE	3.1	0.8	3.7	0.0	0.0	0.4	
	36 min	mean	52.0	12.0	32.6	0.6	0.0	3.2	12
		SE	2.8	0.9	2.7	0.3	0.0	0.2	

* Standard Error

A repeat measurement of anhydrous OPC was completed and the results were almost identical except for Al. The average variation of Ca/Si between two repeat measurements of anhydrous materials was 0.1.

Figure 2-13 shows the change in the Ca/Si of the examined samples in different testing conditions. One standard error is also reported on the curves. The figure shows that the Ca/Si of the measurements on the anhydrous samples were close to 3.0 as expected. Subsequently, the

OPC particles hydrated for 5 min show that the Ca/Si changed from 2.8 to 3.5. These measurements could represent the initial precipitation of hydration products on the surface of the sample. However, the Ca/Si in mC_3S particles did not change considerably after 5 min. This may be caused by the higher reactivity of OPC compared to mC_3S as observed by the calorimetry curves shown in Figure 2-1 and volume change in fCT data from Figure 2-5.

In each system the measured Ca/Si increased until 20 min and then started to decrease. For the particles that hydrated for 20 min there was an observed increase in Ca/Si of 36% and 19% for OPC and mC_3S, respectively. This increase is greater than the standard error. Further investigation of Table 2-5 suggests that the Ca concentration seems to be increasing as the Si concentration is almost constant. This suggests that the hydration products have a higher amount of Ca. This could mean these materials are a mixture of C-S-H and CH with a larger amount of CH or possibly another hydration product that is rich in Ca. After 36 min of hydration, both materials showed a decrease of 10% and 6% with respect to 20 min in Ca/Si of OPC and mC_3S samples, respectively. Again, this seems to be a change in the amount of Ca in the material as the Si concentration does not change significantly.

The change of the Ca/Si shows the same pattern as the percentage of high absorption materials in XRM and fCT data. This suggests that the average Ca/Si in these regions is changing over time. This change in chemistry is an important observation that would change the X-ray absorption of the hydration products over time. This is further discussed in the upcoming sections.

Care has to be taken in interpreting these results as the conditions for conducting this experiment were not ideal for SEM/EDS measurements. Furthermore, the interaction volume of the electron beam could consist of a mixture of the hydration product and an unknown proportion of anhydrous C_3S. However agreement has been found for SEM-EDS on materials of similar age and nXRF for early age hydration products [62]. Also, there are very few techniques that are

capable of providing insights into the surface chemistry of particles at this fragile point in their hydration.

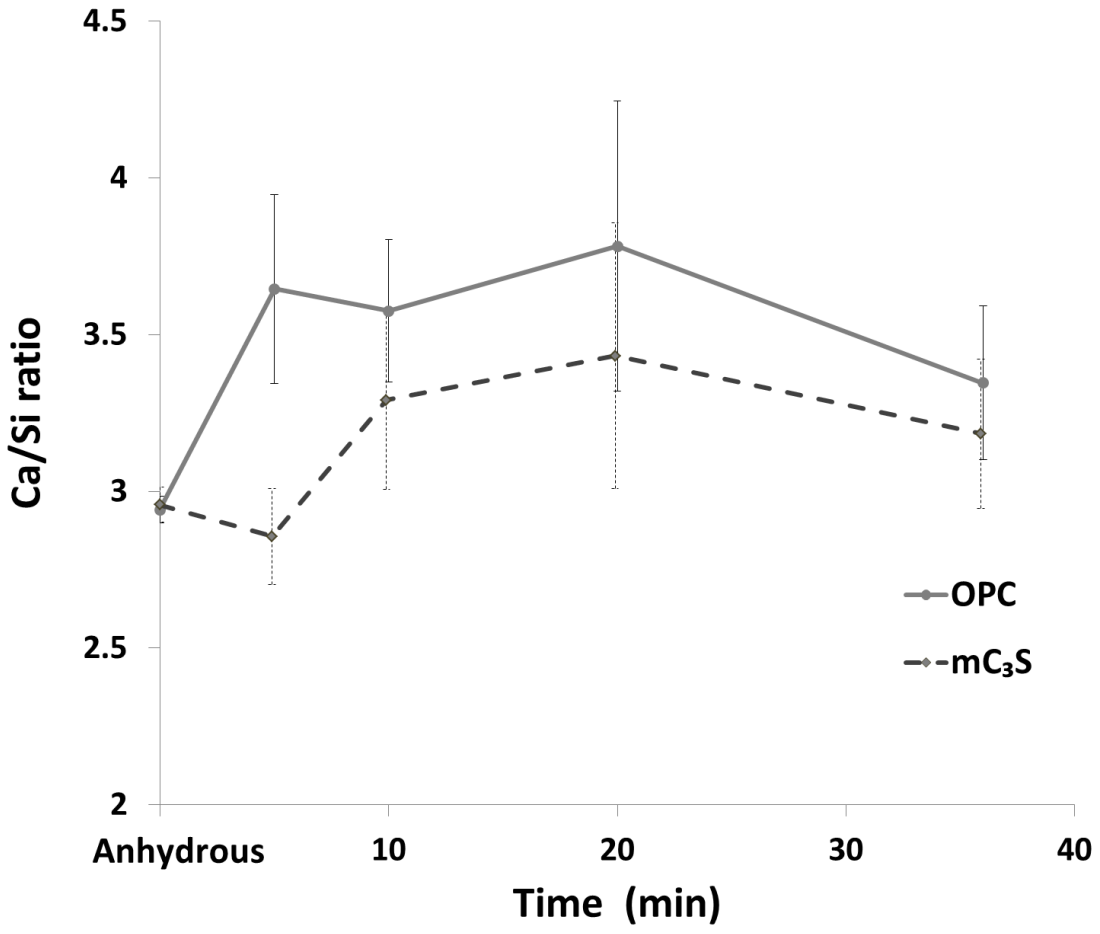

Fig. 2-13. The Ca/Si for different time periods after hydration for a collection of OPC and mC_3S particles in saturated lime water with w/s = 10 as measured by SEM/EDS.

2-3-2-2-2- nXRF and nTACCo

The elemental maps for Ca, Si, S and Ca/Si from nXRF are shown with the borders of the original particles highlighted by a white line in Figure 2-14. Also, results from nTACCo are given in Table 2-6. The average density and one standard deviation are reported for Ca, Si, S, and Ca/Si.

For the sample hydrated for 2 h the Ca/Si map shows that the hydration product was almost entirely above 4. Also, for this sample several locations were observed with a Ca/Si above 10. These regions are likely almost pure CH and were excluded from the analysis in Table 2-6 as they are not likely the same material. The results in Table 2-6 show that Si and S have comparable densities while the Ca density is about 6x greater. This suggests that the hydration product at 2 h could be a mixture of C$\underline{S}$, CH, and C-S-H.

However, for the 10 h data, the Ca/Si of the hydration product is around 2 and there were no regions of Ca/Si above 10 but there is a region where the Ca/Si is above 4. The average Ca/Si is 2.3 for the hydration product and the S density has decreased by 5x when compared to the hydration product at 2 h. This suggests that the hydration product at 10 h could be mainly C-S-H with only local intermixing of CH.

The decrease of Ca/Si of the hydration product from 2 h to 10 h indicates that there is an evolution of the chemical composition of the material. One explanation is that the hydration product at 2 h contains inclusions of CH and C$\underline{S}$ that dissolve before 10 h. This change in chemical composition alters the X-ray absorption of the material. Although the stoichiometry of C-S-H is variable as reported by others [78], a rough calculation of X-ray absorption of mixture of C-S-H and CH with H/S between 1.2 and 4 corresponding to dry and saturated condition of C-S-H. The mass attenuation coefficients of mixtures of C-S-H and CH, a mixture with Ca/Si of between ≈ 4 and 7.5 can have an X-ray absorption similar to anhydrous C_3S. The graph is shown in the appendix A. Therefore, the hydration product formed at 2 h with Ca/Si = 4.40±2.39 would be expected to have an X-ray absorption similar to C_3S. This is why the formation of this material would cause an apparent growth in the high absorption material.

As Ca/Si is reduced to 2.3±0.21 at 10 h, the X-ray mass attenuation coefficient of this material is expected to be between 20% and 27% lower than anhydrous C_3S and so its gray value in X-ray

imaging is lower than anhydrous C_3S and this material is identified as low-absorption material in image analysis. This could explain the changes observed in high-absorption material observed in the fCT data. This will be discussed in more detail in the next section.

Table 2-6. The elemental density and Ca/Si ratio from nTACCo analysis for mC_3S after 2h and 10h of hydration.

	Hydration product		Anhydrous C_3S	
	2 h	10 h	2 h	10 h
Ca (g/cm^3)	1.12±0.54	0.47±0.19	1.69±0.06	1.68±0.19
Si (g/cm^3)	0.20±0.17	0.14±0.08	0.40±0.08	0.42±0.06
S (g/cm^3)	0.173±0.093	0.037±0.027	0.028±0.013	0.01±0.013
Ca/Si (molar)	4.40±2.39*	2.31±0.21	3.08±0.64	2.77±0.08
*Excessive values (Ca/Si >10) are excluded as they are likely CH.				

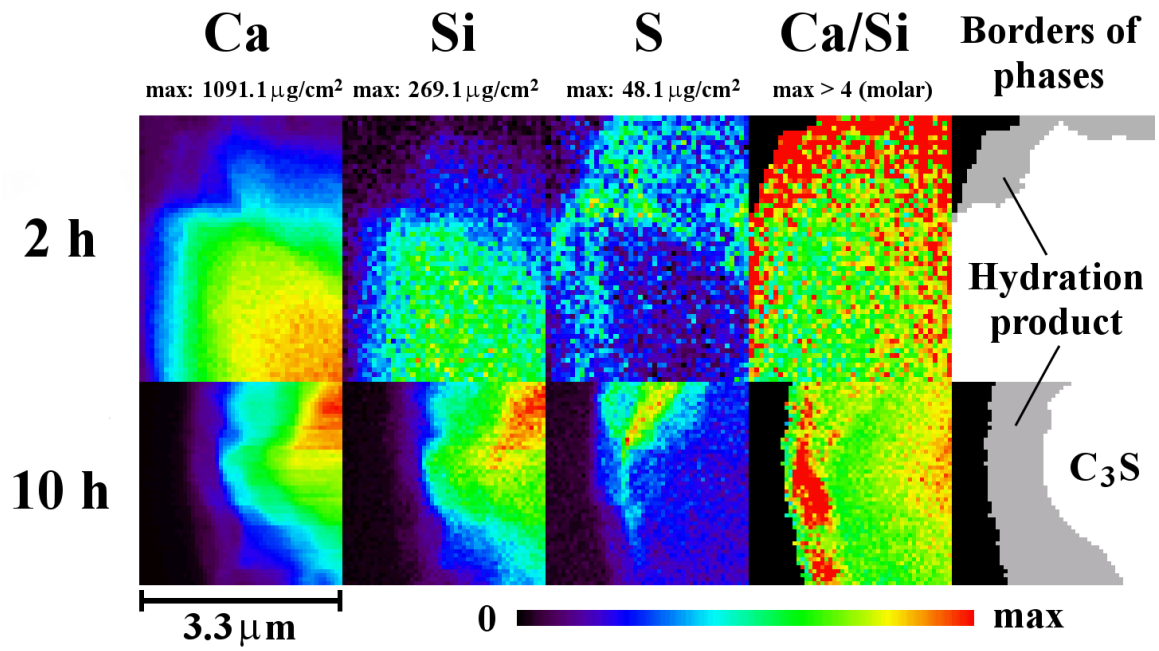

Fig. 2-14. The elemental maps from nXRF analysis after 2 h and 10 h of hydration for mC_3S of particles from Fig. 2-11 and Fig. 2-12. An image at the right from nCT results shows the boundary between the hydration product and the anhydrous region. A white line has been included in each plot to highlight this boundary.

2-4-Discussion

2-4-1- Change in High-Absorption Material

Based on the results from five different X-ray imaging techniques at multiple length scales with different solution environments, it appears that the hydration products formed within the first few hours have a different average chemistry than the hydration products after 10 h. The results show that the chemistry of these materials are different enough that they will increase the local X-ray absorption and these changes can be detected with fCT and TXM.

Measurements with fCT of over 60,000 particles for multiple systems and w/s have been used to investigate this change in X-ray absorption. The results show that the volume of the high-

absorption material increases during the induction period until a maximum value is reached near the start of the acceleration period. This increase in volume appears to be the formation of hydration products with Ca/Si > 4. Based on the SEM-EDS and nTACCo results these hydration products seem to be initially rich in CH and C$\underline{S}$. These could be precipitates that form within the pores of the C-S-H or some other hydration product.

Based on the changes of individual particles at industrially relevant w/s from fCT show that particles smaller than 20 μm seem to decrease in size with time while the larger particles appear to increase in size. This decrease in particle size is likely caused by a higher amount of dissolution than the formation of hydration products. This same process may be happening on all particle but the smaller particles may show these changes to a greater degree because of the larger density of defects and therefore higher reactivity of the smaller particles [75, 79] and/or the higher surface area to volume ratio.

One important observation in the particles larger than 20 μm is that the amount of high-absorption material seems to increase until the beginning of the acceleration period and then decrease. The nXRF and nTACCo results suggest that the Ca and S concentration in the hydration products is greater at 2 h of hydration when compared to 10 h. In fact, the Ca/Si at 10 h is 2.3±0.21. This decrease in chemistry and density will cause the X-ray absorption to decrease. This causes the material in the fCT results to appear to decrease. This is caused because the chemistry and density of the hydration products are decreasing. This will in turn decrease the X-ray absorption of the material and this will decrease the contrast in the fCT data and the amount of detected high-absorption material will decrease. Again, this apparent change in volume as measured by fCT is likely caused by changes in chemistry and density.

2-4-2- A Mechanism for the Cause of the Induction and Acceleration Period

Based on the findings from this work and others [27, 44, 46, 51, 62] a mechanism is proposed that explains the early processes of hydration that are backed by in-situ microstructural and chemical observations and bulk solution changes. Conceptual images of this process are included in Figure 2-15 to accompany the explanation.

Certain regions of anhydrous C_3S have been suggested to be more reactive than others. These regions are shown in Figure 2-15a. When these regions are exposed to solution they will cause etch pits in the surface of the reacting grains as shown in Figure 2-15b [3, 37, 40, 41]. The smaller particles may have a higher density of these regions and this could cause their rapid dissolution as shown with fCT data in this chapter.

Because of the pit geometry the ion concentration may become high enough that hydration products start forming within the pit as shown in Figure 2-15c. Experiments investigating hydration of triclinic C_3S with nTACCo during the induction period in w/s = 5 have found C-S-H with Ca/Si = 1.53 and 1.68 filling these pits [27]. The hydration products with this range of Ca/Si are identified as low-absorption material in fCT data. As the hydration products form they will slow the movement of ions by decreasing the volume of solution within the pit and also providing a physical barrier.

Over time the reactive surfaces will continue to react, although likely at a slower rate. The solids present will decrease the available solution at the reaction site and this will increase the local ionic concentration within the pit (Figure 2-15d). This will cause an increase in ions within the pit that could cause precipitates such as CH and C$\underline{S}$ to form (Figure 2-15e). Because these materials are forming within the pore structure of the C-S-H within the pit these materials would be expected to be <30 nm in size based on previous publications of the pore sizes within C-S-H [80, 81]. This observation is supported by data in this chapter as nXRF and nTACCo measurements

show high concentrations of Ca and S during this time period. This material will increase the X-ray absorption of the hydration products as high as the X-ray absorption of anhydrous C_3S and this is why the fCT and TXM results can observe these changes.

As the nano CH and C$\underline{S}$ forms within the hydration product this will reduce the porosity and slow the ion transport. This will slow the dissolution of the damaged regions and cause the induction period. While this slows the dissolution, it will not stop it. Ions will continue to escape and cause the ion concentration to increase in the pore solution. The average ionic concentration of Ca in the pore solution during the induction period suggests a continuous increase in Ca concentration [44, 46]. This will continue until hydration products start forming in the bulk solution as shown in Figure 2-15f. Previous publications have shown that hydration product formation coincides with the start of the acceleration period [44, 46, 52, 53].

The formation of these hydration products may cause the region within the pits to no longer be saturated with respect to Ca and S. This under-saturation may cause the CH and C$\underline{S}$ precipitates to dissolve into the surrounding solution as shown in Figure 2-15g. This would cause the X-ray absorption of the hydration product to decrease as these materials dissolve. This was observed by both fCT and TXM datasets as shown in Figure 2-5 and Figure 2-10.

As these hydrates slowly dissolve the ions will diffuse into the bulk solution and increase the porosity of the hydration products and allow the high reactive regions to begin dissolving. Since the fast reacting sites have been surrounded by local hydrates or exhausted, this makes the slower reacting sites available to the solution and this would promote dissolution and rapid formation of C-S-H and CH. This renewal of reaction is when the acceleration period will begin.

The 10 h nTACCo results suggest that the hydration product has a Ca/Si $\approx$ 2.3$\pm$0.21, which is much lower than the Ca/Si $\approx$ 4.4$\pm$2.39 that was observed at 2 h. This supports the idea that the chemistry of the hydration product is changing and lowering the X-ray absorption. Another

observation made at 10 h is that the particle surface is covered in hydration products (Figure 2-15h). These products may reduce the availability of solution to the surface and then slow the dissolution and therefore the reaction of the surface. This may be responsible for the deceleration period.

This mechanism provides a probable explanation of a series of events that could cause the onset of the induction period and then the rapid dissolution of the acceleration period and then the slowing of reaction in the deceleration period. This information is based on a large number of in-situ X-ray imaging methods to measure the structure and chemistry. This mechanism suggests that detailed understanding of both chemistry and structure are needed to accurately describe this phenomenon. Additional work is underway to make a larger number of observations of these critical periods as well as nano scale in-situ measurements that will help provide even more insight into this mechanism. Ultimately this work will be useful to build mechanistic based numerical models that can more accurately predict behavior of hydrating cement systems. This could also be used to provide new insights into admixture design and manufacturing processes of cements to improve performance.

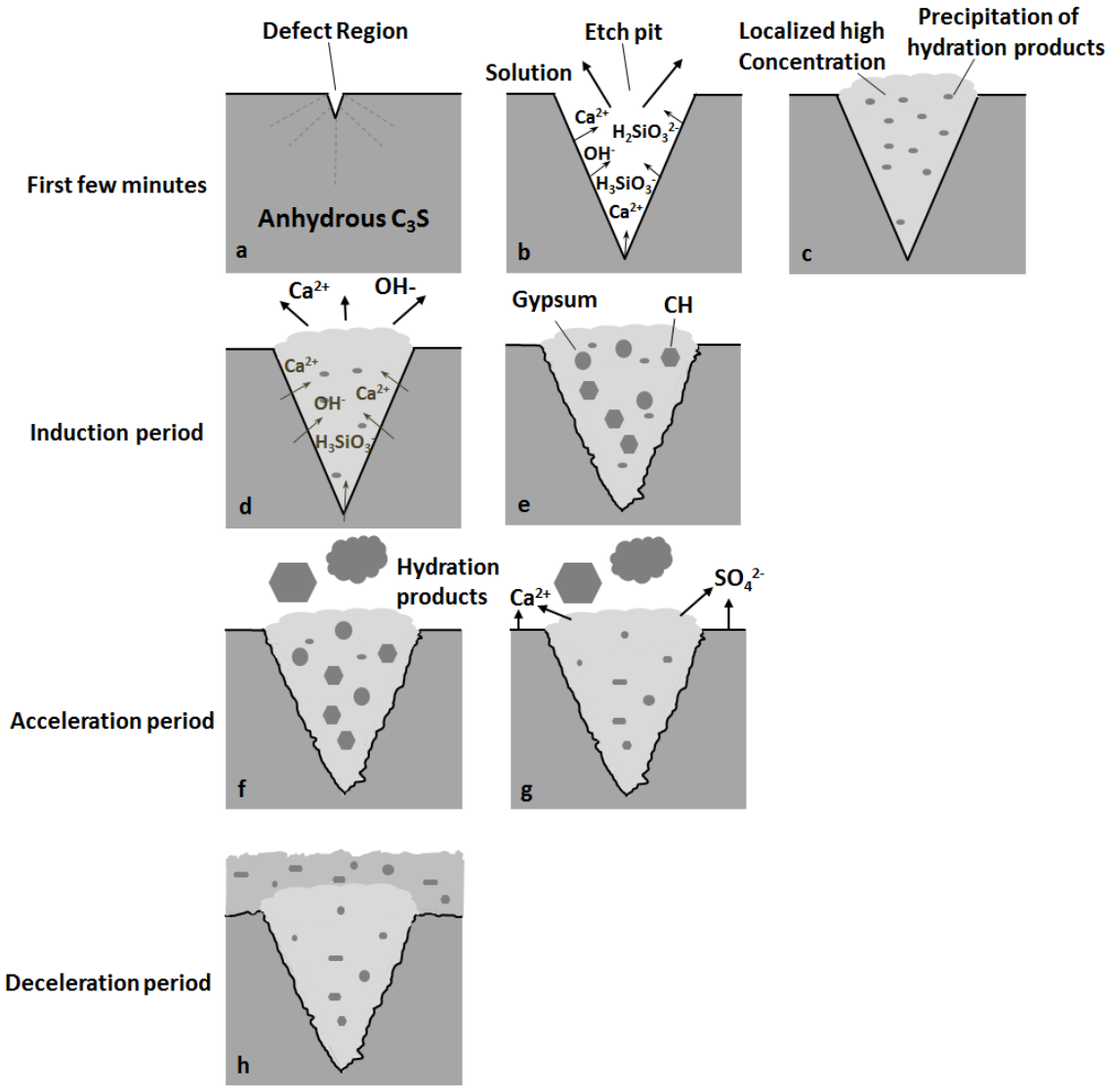

Fig. 2-15. Schematic demonstration of the proposed mechanism; a) region of defect on anhydrous cement particle, b) formation of etch pit with high ionic concentration within, c) increased ionic concentration within the pit and formation of hydration products, d) the region of defect continues to react but at a reduced rate and local ion concentration increases within the pit, e) ion concentration increase continues and CH and C$\underline{S}$ precipitates within the pores of the C-S-H, f) ion concentration builds in solution until hydration products form in the bulk solution, g) the hydration product formation in the bulk reduces ions in solution and causes the CH and C$\underline{S}$ precipitates to dissolve as well as the slower

reacting surface of the anhydrous particle, h) the surface of particle is covered by hydration products and this slows dissolution.

2-5-Conclusions

This chapter provides *in-situ* observations of the evolution of OPC and mC_3S during hydration over the first 16 h by using five different X-ray imaging methods. A strength of the current study is the use of fCT to observe 3D changes of roughly 60,000 particles with industrially relevant w/s = 0.40 to 0.70 at 1 μm resolution. These observations are then supported by nanoscale observations in dilute solutions with TXM and nCT. Also quantitative measurements of the chemistry and structure at the nanoscale were made by nTACCo. The following conclusions can be drawn from the findings of this study:

- All five experimental techniques suggest that the hydration product formed during the induction period had an average Ca/Si greater than 3.
- Micron scale measurements showed that the volume of the high X-ray absorption material increases during the induction period and seems to form on the surface of the particles larger than 20 μm while the particles smaller than 20 μm show primarily dissolution. These same measurements show that as the acceleration period begins the X-ray absorption of the hydration product decreases.
- Nanoscale measurements during the induction period for 2 h of hydration in a saturated lime and gypsum solution found an average Ca/Si of 4.4 (±2.39) while the same measurements on particles after 10 h of hydration found an average Ca/Si of 2.31 (±0.21).
- Regions at 2 h of hydration also showed regions with Ca/Si > 10 which are likely CH and regions with high S content. After 10 h of hydration these same areas were not observed.

The hydration products showed that the Ca and S decrease by 6x between 2 h and 10 h while the Si concentration decreased by ≈ 30%.

- The nanoscale measurements show that the hydration products form locally on the surface of the reacting particles and these extended a few microns away from the particle surface.

- The micron scale measurements also show non-uniform growth and dissolution were observed on each particle.

These observations suggest that the formation and subsequent change in chemistry of these early age hydrates is important to the mechanisms of hydration. The hydration product observed during the induction period is thought to be a mixture of C-S-H, CH, and C$\underline{S}$. A mechanism is proposed that explains how the formation and dissipation of this material may be responsible for the induction and acceleration period in cement hydration. Further experiments are needed to clarify the chemistry and nature of the changes that occur at the surface and in the surrounding fluid during this critical time period but these observations give important insights into the mechanisms.

CHAPTER III

DIRECT OBSERVATION OF VOID EVOLUTION DURING CEMENT HYDRATION

Abstract

This chapter follows the hydration of both portland cement and tricalcium silicate pastes between 30 min and 16 h of hydration. In-situ fast X-ray Computed Tomography (fCT) was used to make direct observations of the air-filled void formation in w/s of 0.40 to 0.70 with a micron resolution.

The results show that at the end of the induction period the volume of air-filled voids reaches a maximum value and then decreases during the acceleration period and stays constant. The void distribution changes from a few coarse voids to a large number of smaller and more uniformly distributed voids. This behavior is suggested to be controlled by changes in the ionic strength that cause exsolution of dissolved air from the pore solution.

Keywords: X-ray Computed Tomography; Cement Hydration; Void Evolution; Calorimetry; Induction Period

3-1-Introduction

The hydration of cement paste has received significant attention because the ultimate mechanical properties and durability of hardened concrete are controlled by the microstructure development [2-5]. Specifically, the porosity of cementitious paste directly impacts the mechanical properties, durability, and dimensional stability of concrete [2, 82-84]. Therefore, a better understanding of pore system development and the influencing parameters are of great importance.

Most conventional methods of measuring porosity, such as mercury intrusion porosimetry, sorptivity, gas adsorption, helium inflow, acoustic emission, and alternating current impedance spectroscopy, are useful to provide information about the total pore content and give insights into the bulk void size distribution [85-91]. However, these techniques cannot resolve details of the shape, size or spatial distribution of the voids. Moreover, most of these techniques cannot investigate the in-situ development and formation of pores at early ages without disturbing the sample. In recent decades, imaging techniques such as scanning electron microscopy (SEM) and transmission electron microscopy (TEM) are widely used to investigate the microstructure and pores at various ages in cement paste [14-17, 20]. Although SEM and TEM provide images with high resolution, the results are limited to the investigated 2D cross-section of the sample [18]. In addition, the required sample preparation such as polishing may cause artifacts in fragile samples.

X-ray computed tomography (XCT) is a powerful and non-destructive technique that can be completed in many cases with no sample preparation [19, 20, 26, 27, 62, 92-94]. This method has been used in numerous studies to identify the engineering properties of a cementitious system such as aggregate spatial distribution [95], transport properties [96, 97], determination of air void parameters [95, 98-101], and to examine leaching [93]. This equipment is also widely used in medicine to look at biological samples non-destructively [24, 25]. The methods used are the same, only at different length scales. A series of 2D X-ray radiographs are acquired from

different viewing angles and the data are used to build a 3D rendering of the sample. The 3D rendering can be used for morphological and quantitative analyses. The gray value in the produced images is a function of X-ray absorption and can indicate differences in chemistry and density of the materials [26-28]. The contrast in gray value intensities can be used to evaluate XCT dataset quantitatively by separating the collected images into regions of different constituents. This process is called segmentation.

In spite of the powerful abilities of ordinary XCT, the necessary time for data acquisition at a micron length scale may be several hours and so it cannot be used to study rapidly evolving processes, such as what occurs during the first hours of hydration of cementitious paste [4, 29, 30]. Measurements show that the Ca concentration continuously increases over the first hours of hydration reaching a maximum at the end of the induction period and then decreasing [44, 46, 102]. These ionic concentration changes have been linked to changes in the microstructure and are important in hydration [3, 67, 94, 102, 103]. It is also important to note that previous experiments using acoustic emission have detected signals that were interpreted as void formation during the solidification of cement paste at early ages [91]. The acoustic emission technique is a bulk measurement, so it is not able to give detailed description of the void formation.

To study cement hydration at early ages, some researchers have collected tomographs from the first hours of hydration by lowering the exposure time and number of acquired projections [4, 104]. However, the results have significant artifacts and limited contrast. This has limited their findings. Consequently, previous XCT studies on porosity have focused on systems after initial set and have observed porosity decrease from infilling of hydration products [4, 18, 26, 105].

Recent breakthroughs in X-ray imaging now enable tomography data collection to be made at near video acquisition rates at the Advanced Photon Source (APS) at Argonne National Laboratory. The technique is named fast computed tomography (fCT). This advancement is

possible because of improvements in detectors, precision stages, and increased photon flux [29-33]. While this technique has been used to study many dynamic processes, there are few published works that have used fCT to investigate cement hydration [4, 94, 106, 107].

This chapter used fCT to investigate the air-filled void system evolution in cementitious pastes with industrially relevant w/s during the first 16 h of hydration. The data provide important insights about the void formation and can be useful to verify analytical models and improve their assumptions about mass transport.

3-2-Methods

3-2-1-Materials

Two cementitious materials were used in this study, portland cement 168 (hereafter termed OPC) from the Proficiency Sampling Program of the Cement and Concrete Reference Laboratory (Frederick, Maryland) and monoclinic tricalcium silicate powder (mC_3S) from Mineral Research Processing (Meyzieu, France). These powders were characterized by ASTM C114 testing method and X-ray diffraction (XRD) for chemical analysis of OPC; automated scanning electron microscopy (ASEM) was used for particle size distribution and chemical analysis of mC_3S.

The results of the chemical composition analysis, Blaine fineness (ASTM C204), and the density of the used materials are presented in Table 3-1. XRD analysis showed that mC_3S is close to pure C_3S. XRD analysis of OPC is available in another publication [64]. The details of the ASEM technique and the particle size distribution of both powders can be found in the appendix A. Based on the Blaine fineness and particle size distributions, OPC is finer than mC_3S.

Table 3-1. Specifications and bulk chemical composition of cementitious materials.

	Blaine (cm^2/g)	BET surface area (m^2/g)	Density (gr/cm^3)	Chemical Composition (%)						Phase concentration (%)			
				SiO_2	CaO	Al_2O_3	MgO	Fe_2O_3	SO_3	C_3S	C_2S	C_3A	C_4AF
OPC	4080	NA	3.15	19.91	62.27	5.11	3.87	2.15	3.49	54.5	15.7	8.0	7.0
mC_3S	3588	0.86	3.12	26.54	71.97	0.94	0.06	0.48	-	≈100	-	-	-

3-2-2-Sample Preparation

The mixing procedure was the same for all samples examined by fCT, isothermal calorimetry, or chemical shrinkage. First, water was added to 5 g of the powder. After adding the water, the mixture was stirred by a stainless steel rod ten times clockwise and then ten times counterclockwise in a glass vial. Then the vial was shaken by a vortex mixer (produced by Stuart-Staffordshire, UK) with a speed of 1000 rpm for 3 min. After mixing, a 1.5 mm diameter by 6 mm length polyethylene tube was pushed into the fresh paste. The tube was inserted to capture about 4 mm of paste. A finger was then used to cover the end of the tube and it was removed from the fresh paste. The generated vacuum in the sealed tube held the fresh paste within the tube as it was removed. The tube was then sealed with clay to minimize vapor transport and loss of mixing water during scanning. Finally, the sample was compacted by holding the sealed sample in one hand and clapping it into other hand ten times.

Five paste samples were produced for examination and the details of the tests are presented in Table 3-2. Four paste samples were produced with deionized water as a mixing liquid, while the fifth sample was made with OPC and de-aired water with w/s = 0.60. To produce the de-aired water, the deionized water was boiled and then cooled to room temperature in a He environment. Helium was used because of its low solubility in water [108]. While still in the He environment the de-aired water was added to the OPC powder by a syringe and then mixed as per the standard procedure.

The first tomograph was acquired after sample preparation and alignment of the instrument. This took between 34 to 70 min for each sample.

Table 3-2. Details of fCT paste samples.

Cementitious material	w/s	Water type	Time for first tomograph (min)	Time for last tomograph (h: min)
mC_3S	0.70	Deionized	70	15:40
mC_3S	0.45	Deionized	70	15:40
OPC	0.60	Deionized	34	11:34
OPC	0.40	Deionized	34	11:34
OPC	0.60	de-aired	43	9:47

3-2-3-Isothermal Calorimetry and Chemical Shrinkage

Isothermal calorimetry was used to measure the heat of hydration. This test was conducted with a Tam Air Isothermal Calorimeter on samples at a constant temperature of 25 °C over 18 h. The assumed heat capacity of OPC and mC_3S was 0.753 $Jg^{-1}K^{-1}$, and the capacity of deionized water was 4.1814 $Jg^{-1}K^{-1}$. The samples were made in the same way as the fCT experiments, except that 3 g of powder was used. After mixing, the vials containing the fresh paste were capped and added to the calorimeter.

The chemical shrinkage measurements were made in the same manner as other samples in this chapter but the mixture used 20 g of powder and the chemical shrinkage was measured for 18 h. In this method, a sensitive differential pressure sensor is used to measure the water level drop caused by chemical shrinkage in a capillary tube. More details can be found in other publications [109, 110].

3-2-4-Fast X-Ray Computed Tomography

The fCT was conducted at the 2-BM beamline at the Advanced Photon Source (APS) at Argonne National Laboratory. This technique allows collection of tomographs in less than 5 s; however, the tomographs were collected at 10 min intervals in a room with constant temperature of 25 °C. The instrument settings for the scans are provided in Table 3-3. More details about the facilities can be found in other publications [31, 32].

Table 3-3. Instruments settings for fCT instrument.

Resolution	1 μm/pixel
Source energy	30 kev
Total scan time	5 s
Number of projections	1500
angular increments	0.125°
projection dimensions	2016 pixel×1536 pixel
Reconstruction algorithm	Gridrec

3-2-5-Reconstruction and Segmentation

The 2-D radiographs were reconstructed using a Fast Fourier Transforms (FFT) algorithm [32]. The same instrument and reconstruction settings were used for all subsequent tomographs to make quantitative comparisons. Figure 3-1 shows a typical data set from mC_3S with a w/s = 0.70 as well as a typical cross section and a segmented image that highlights the voids. The segmentation process will be discussed further later in the chapter.

Each image is made up of individual pixels with a 16-bit gray value. The variation of gray value within the scanned sample is caused by the differences in the atomic electron density and/or the bulk density of the imaged material [22]. Absorption tomography is defined by the Beer-Lambert Law:

$$\frac{I}{I_o} = \exp(-\mu_m \rho x) \qquad (3\text{-}1)$$

where I is transmitted intensity, I_0 is incident intensity, μ_m is X-ray linear attenuation coefficient, ρ is density, and x is the length travelled by the X-rays [68].

To reduce computational efforts, 100 slices out of 1500 were analyzed from each data set. Moreover, the inner section of the sample was investigated to avoid edge effects. This space contained roughly 60,000 anhydrous particles to be imaged in each tomograph [94]. To reduce noise in the data, a median filter with a radius of 2.5 μm was applied to all slices. This filter is used to preserve image edges with minimal signal distortion. It has been widely used by others [65, 66, 111, 112].

While there are many possible segmentation algorithms, one common method is to use a single gray value that separates a target material in the images. This study aims to track the evolution of air-filled voids. This means that the method needs to be used to track how the air-filled voids changed in comparison to the rest of the paste. To determine which gray value should be used to separate air-filled space in each sample, at least 30 individual air-filled voids from various locations of region of interest (ROI) and from different time periods were identified by an operator and the average gray value of each one was determined. This process was repeated for each sample to find the average gray value of voids for that specific sample. A histogram of the measured data on OPC w/s = 0.60 can be found in the appendix B.

The gray values within voids were found to be normally distributed. This means that 99.7% of the expected values are contained within three standard deviations of the mean and so this value was used for the void segmentation. This provided an easy approach that could be applied for each investigated sample while still providing a high level of confidence in the data. Fig. 1 shows a region of a slice obtained from mC_3S with w/s = 0.70 before and after the segmentation of air-

filled voids. More details of the reconstruction and image processing can be found in the appendix B.

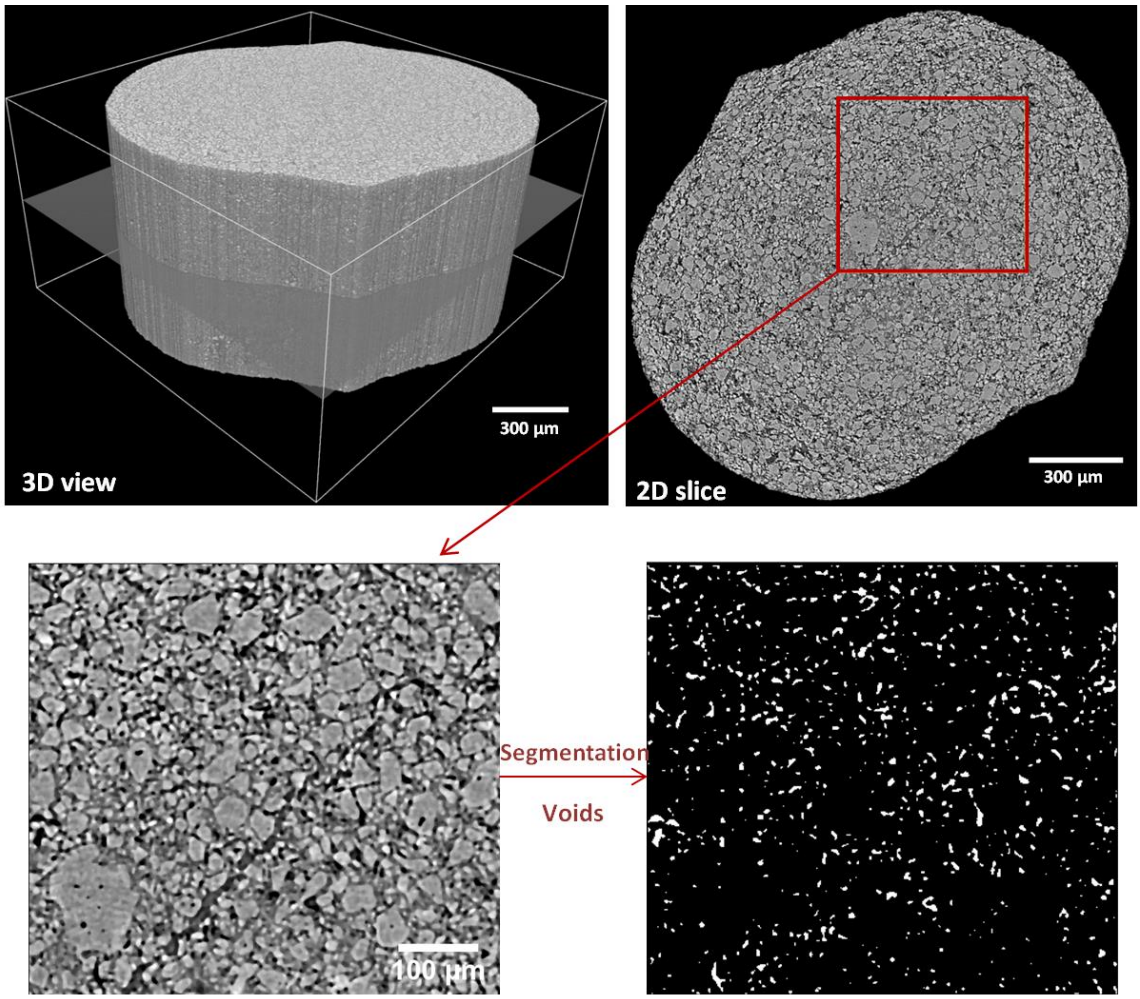

Fig. 3-1. Typical data sets from fCT of the 3D model and region of interest. The result of the segmentation for the air filled space is shown for mC_3S paste with w/s=0.70.

3-2-6-Measuring Void Spacing

The uniformity of void distribution is quantified by estimating the average nearest-neighbor distance between individual voids at different time periods. This was investigated by measuring

center-to-center nearest-neighbor distance for each individual void within each tomograph corresponding to a specific time period. Then, the average and standard error of all measured distances are calculated in the tomograph and reported as the average nearest-neighbor distance of voids in the sample at the corresponding time period.

3-3-Results and Discussion

3-3-1- Isothermal Calorimetry and Chemical Shrinkage

Figure 3-2 demonstrates the heat flow results of four examined pastes over the 18 h of hydration. The results of the OPC samples are shown by black lines, while gray color is used to show the results of mC_3S. This same nomenclature is used throughout the chapter. The w/s was chosen to match the values used in the fCT experiments. The OPC system showed a higher heat release compared to the mC_3S system. This difference may be attributed to the different chemical composition, w/s, and particle size distribution of the examined powders.

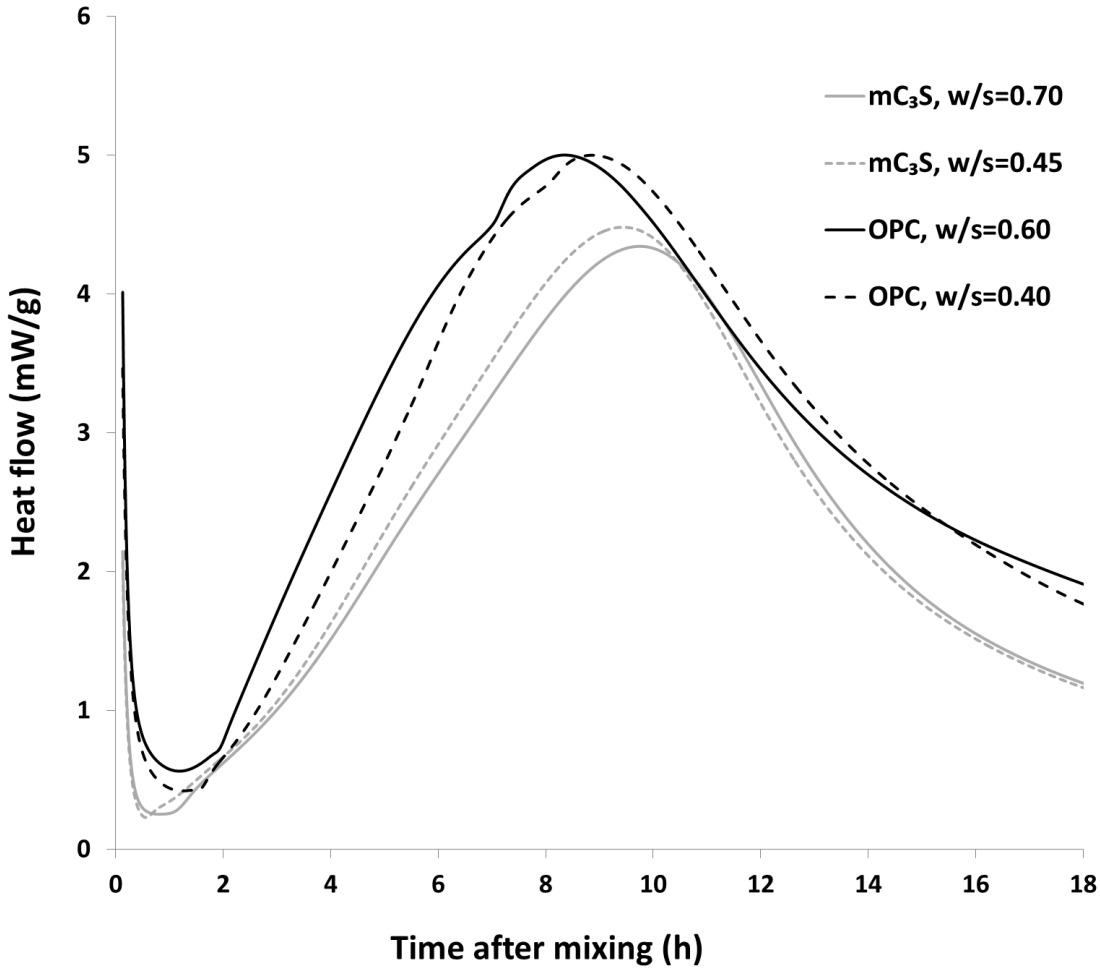

Fig. 3-2. Heat evolution curve of the examined pastes made with deionized water.

As can be seen in the Figure 3-3, OPC with w/s = 0.60 has the lowest shrinkage over the first 16 h, while mC_3S with w/s=0.70 showed the highest shrinkage among the examined samples. Also, there is a significant difference between the chemical shrinkage in mC_3S w/s = 0.45 and mC_3S w/s = 0.70, while the difference in two examined OPC pastes is not significant. The mC_3S sample with w/s = 0.70 seems to have a very different performance over the first 2 h that may be due to experimental error.

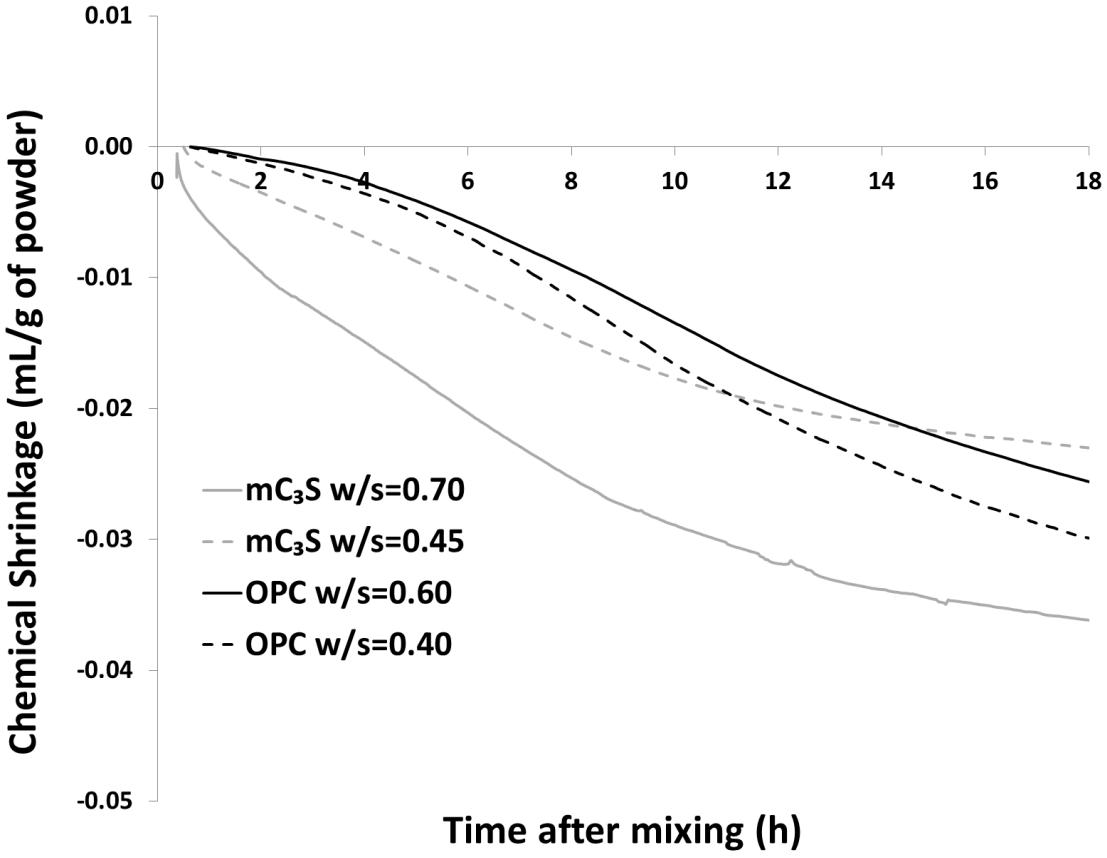

Fig. 3-3. Chemical shrinkage of the examined pastes made with deionized water.

3-3-2-Volume Change of Air-Filled Voids and Heat of Hydration

Figure 3-4 demonstrates the changes in total volume of the air-filled voids over the first 16 h of hydration. Each point in the graph represents the volume percentage of the air-filled voids at each time period.

For all of the samples investigated the air content increases and then decreases to a constant value. It is probable that a peak has occurred in mC_3S with a w/s = 0.45 before the first collected tomograph at 70 min. The samples made with lower w/s seem to have reached their peak earlier than those with a higher w/s.

The sample with de-aired water had the lowest measured volume of air and showed minimal volume change during the time investigated. The observed volume change is slightly higher than the almost constant volume of air that was measured for the samples with deionized water with mC_3S at w/s of 0.70 and 0.45 and OPC at w/s of 0.40. It is expected that some air filled space would be trapped during mixing and there may be only a slight increase in the observed volume. This suggests the de-aired water is important to the mechanism causing the void volume increase. This will be discussed in more detail later in the chapter.

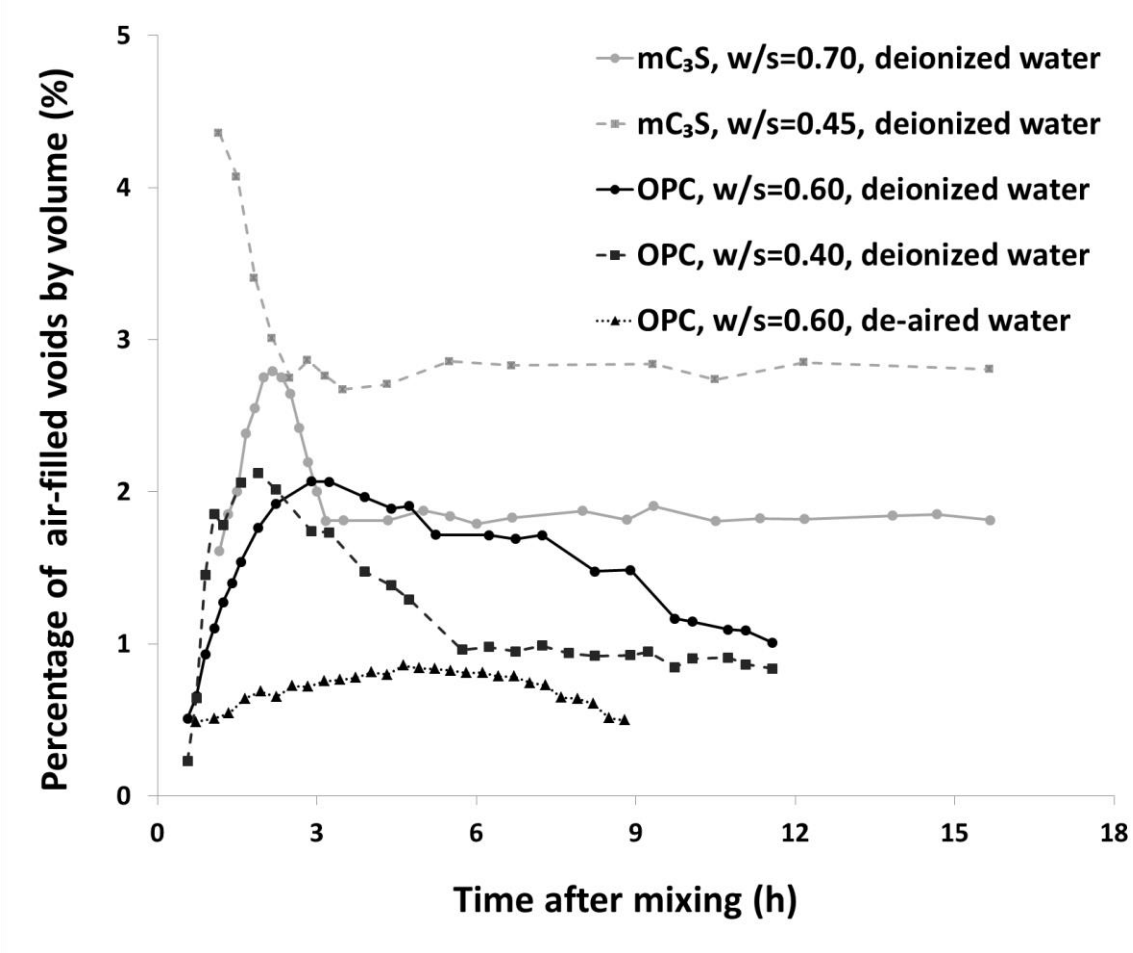

Fig. 3-4. Volume change of air-filled voids over time.

Figure 3-5 combines the volume change of the air-filled voids for the samples that did not use de-aired water with the isothermal calorimetry curves. The total volume of air-filled voids is increasing during the induction period. The peak void volume seems to correspond to the initiation of the acceleration period. Later, the total volume of voids apparently decreases during the acceleration period. Finally, the bulk volume stays almost constant. This may be caused by initial set.

Another study discussed in chapter 2 on the same data set showed that the increase in void content coincides with formation of a hydration product with a high X-ray absorption near the surface of the hydrating grains [94]. These phenomena are likely related. This will be discussed further in section 3-4.

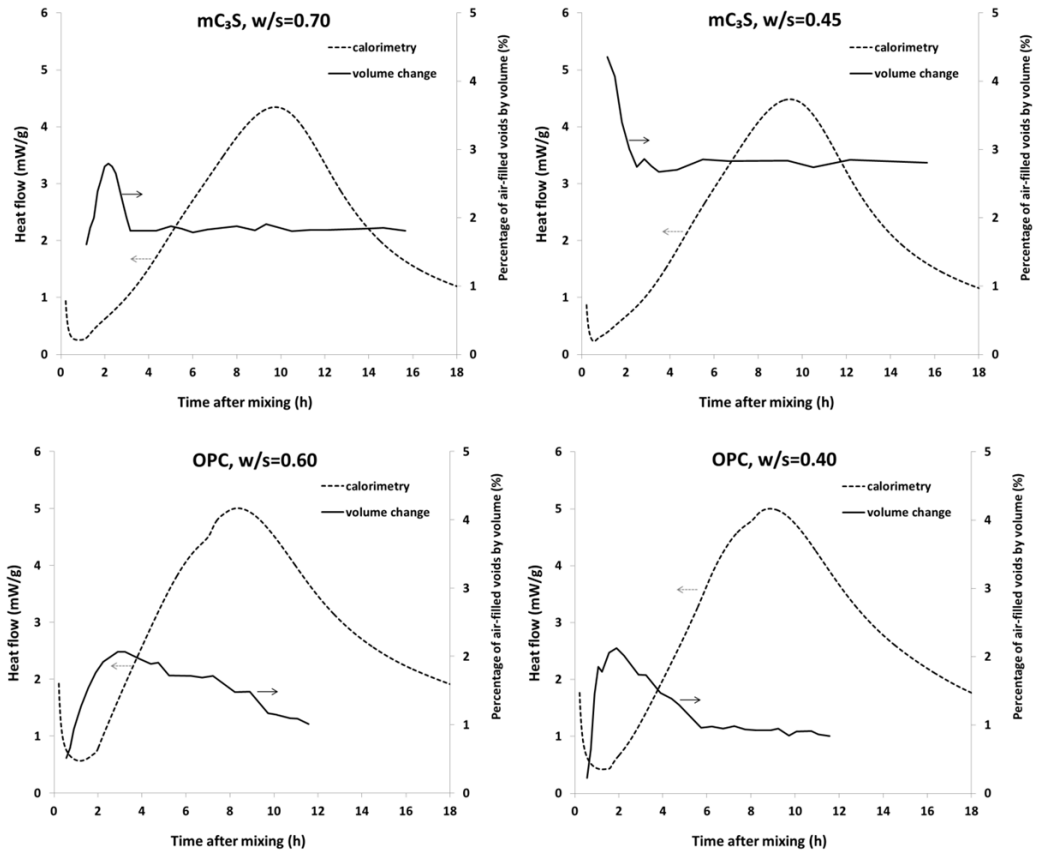

Fig. 3-5. Comparison of heat release to volume change of air-filled voids in samples made with deionized (not de-aired) water.

3-3-3- Spatial Distribution of Voids

The evolution of voids in OPC w/s = 0.40 and mC_3S w/s = 0.70 is shown in 3D and with representative 2D slices in Figures. 3-6 and 3-7. The raw data from a 2D slice are shown at the left with the segmented image in the middle showing the air-filled voids as a binary image. The 3D renderings are shown on the right where the volumes of the voids are shown with different colors. The voids larger than 200 μm^3 are shown in red and those smaller than 25 μm^3 are green. Other sizes are shown by colors between red and green and details can be found in the legend.

These images help the reader to visualize the results and make general observations. Similar observations are made for both mC_3S and OPC at different w/s and so the observations will be jointly discussed. More quantitative data will be given later in the chapter. Both images show that voids smaller than $\approx$100 μm^3 are forming between 0.6 h and 2.5 h, while the larger voids are observed to decrease in size.

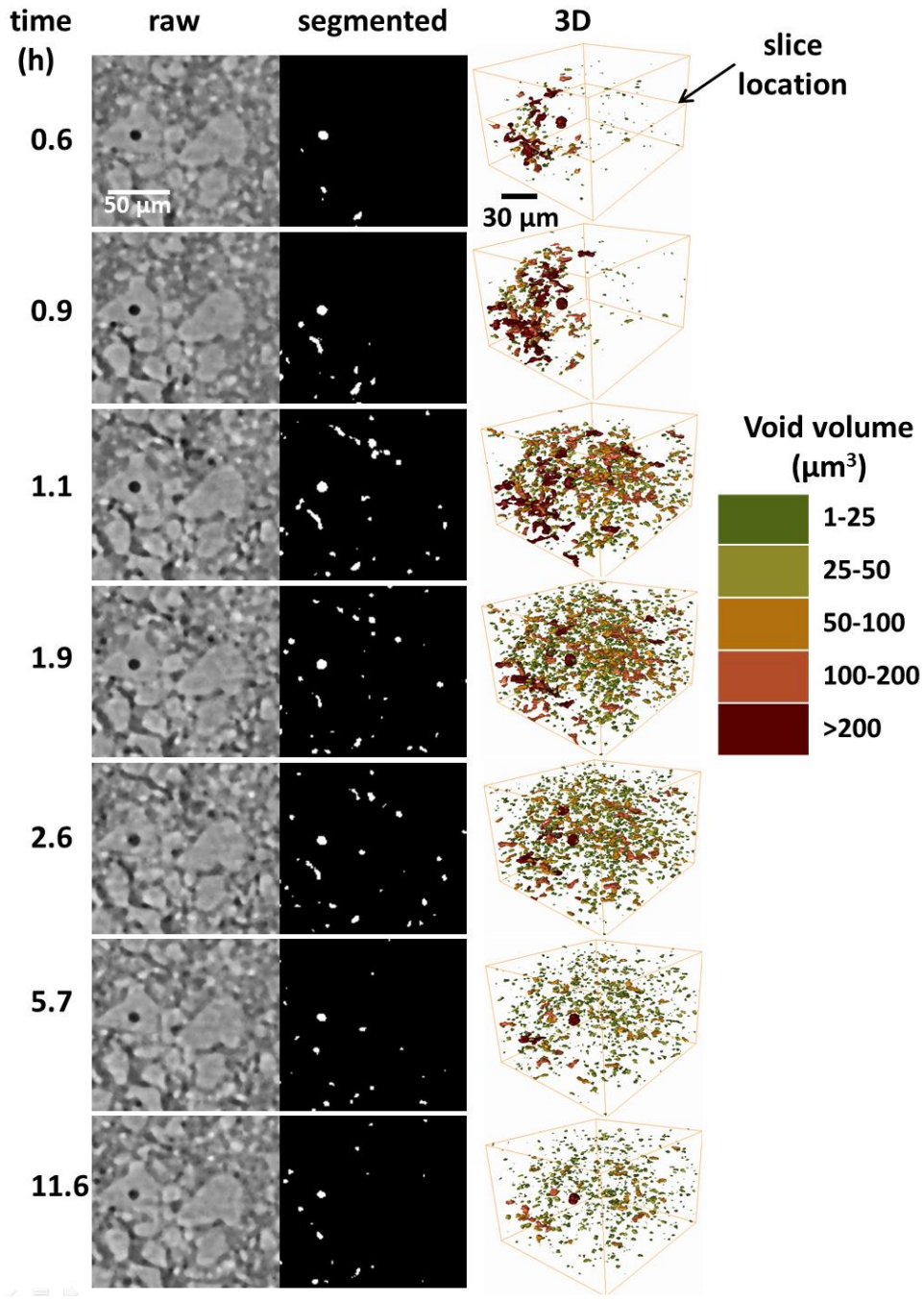

Fig. 3-6. 3D view of void size distribution in critical time periods of OPC w/s = 0.40.

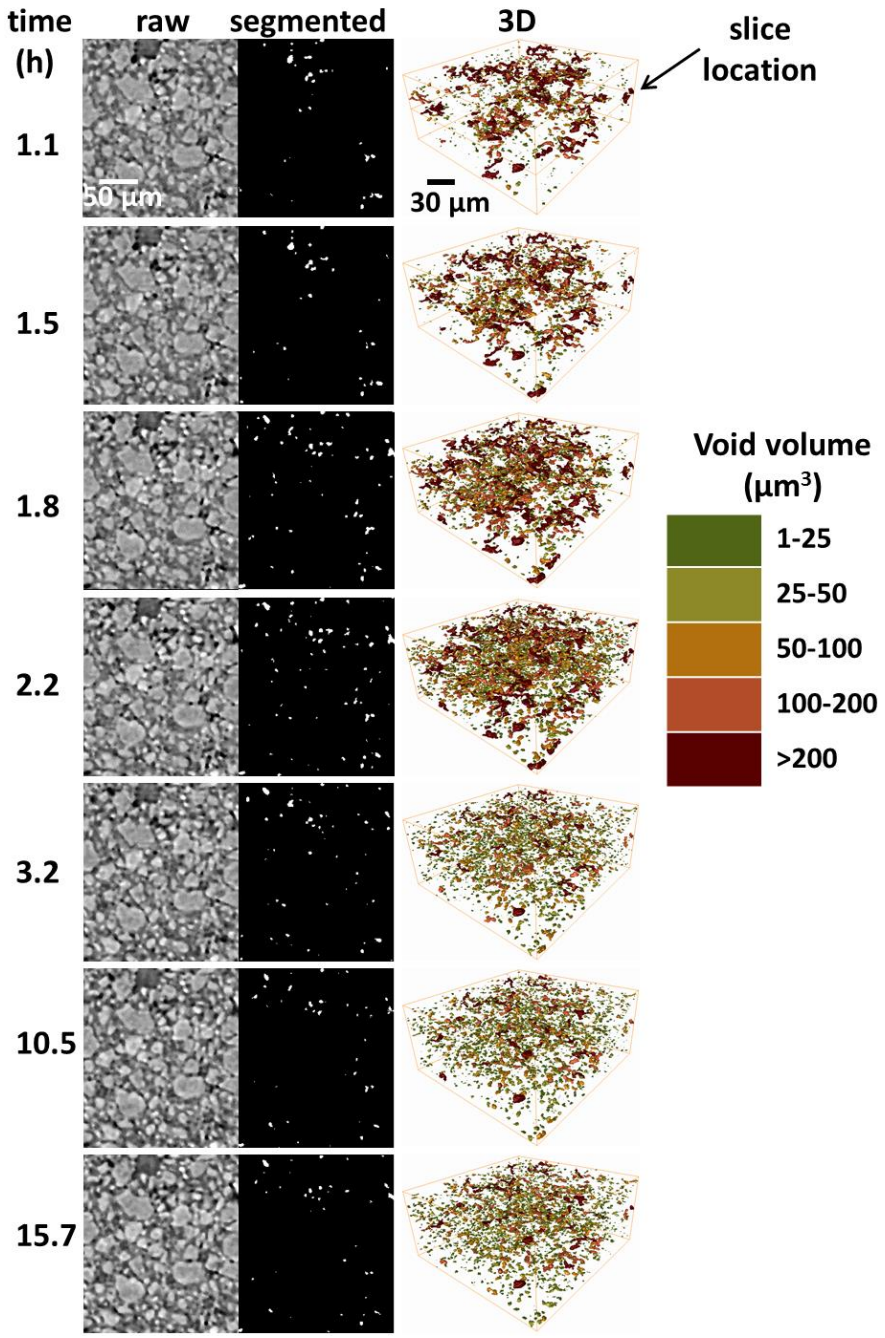

Fig. 3-7. 3D view of void size distribution in critical time periods of mC_3S w/s = 0.70.

It also appears that the spatial distribution of the voids changes over time. Figure 3-8 shows the change in the average nearest-neighbor distance between individual voids in different time periods of the experiments. Each point in the graph is an average of the calculated nearest-

neighbor distance for all individual voids in the corresponding time period. One standard error is also reported.

The average distance between voids in samples made with deionized water is higher before ≈ 2.5 h, which is during the induction period. Over time, the average distance for all samples reaches a constant value, such that the spatial distribution of the voids is almost constant after ≈ 4 h. This supports the observations made in Figures 3-6 and 3-7.

The distance between voids in the sample made with de-aired water was significantly higher than the other samples. This was expected since this sample has the lowest amount of air-filled voids. As a result, the number of voids should be lower and therefore their spacing is higher. If the void formation is caused by exsolution of dissolved gas in the liquid then the nucleation location and frequency will be dependent on the ionic concentration of the liquid. This will be discussed in the next sections.

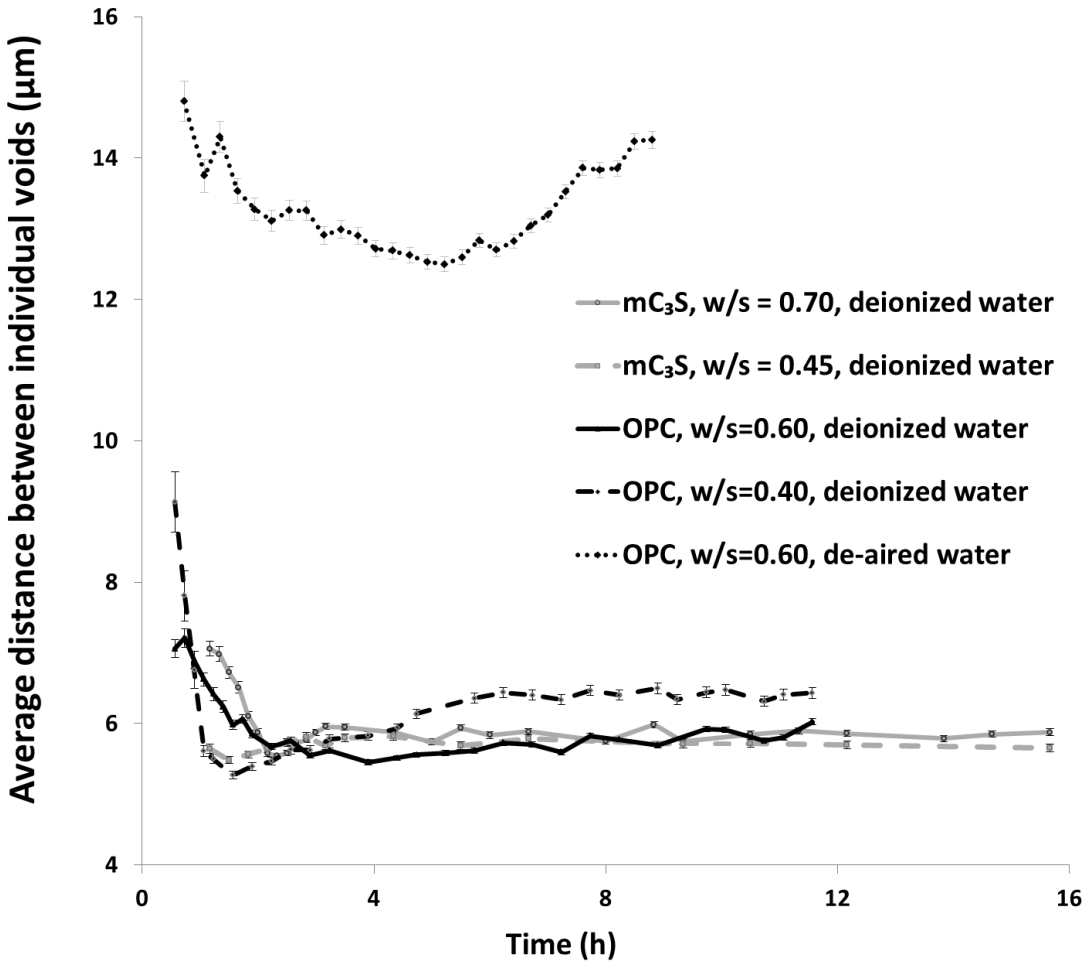

Fig. 3-8. Average nearest-neighbor distance between air-filled voids in different time periods.

3-3-4-Change in Individual Voids

The behavior of individual voids is further investigated by following a collection within mC_3S paste with w/s = 0.70. These voids have been separated into three different size groups based on their observed behavior. The results for all of the voids are included for comparison. The details are provided in Table 3-4 and the results in Figure 3-9.

Table 3-4. Number of individual voids in each size group.

Paste type	Average volume (μm^3)	Number of individual particles observed
mC_3S, w/s=0.70	50-200	40
	200-400	18
	>400	4

One standard error has also been included to show the variation. Since there were very few voids larger than 400 μm^3, the variation for this group is high. In general, the volume change of the single voids follows a similar trend to that of the overall system; however, they have some differences based on their size. The voids larger than 400 μm^3 showed a constant volume between 3 h and 16 h that was larger than the original volume at 70 min. The isolated voids smaller than 400 μm^3 decreased in volume after approximately 2 h of hydration and reached constant values that remained unchanged until the end of the experiments. The rate of change of the voids smaller than 200 μm^3 may be caused by the higher ratio of surface area to volume.

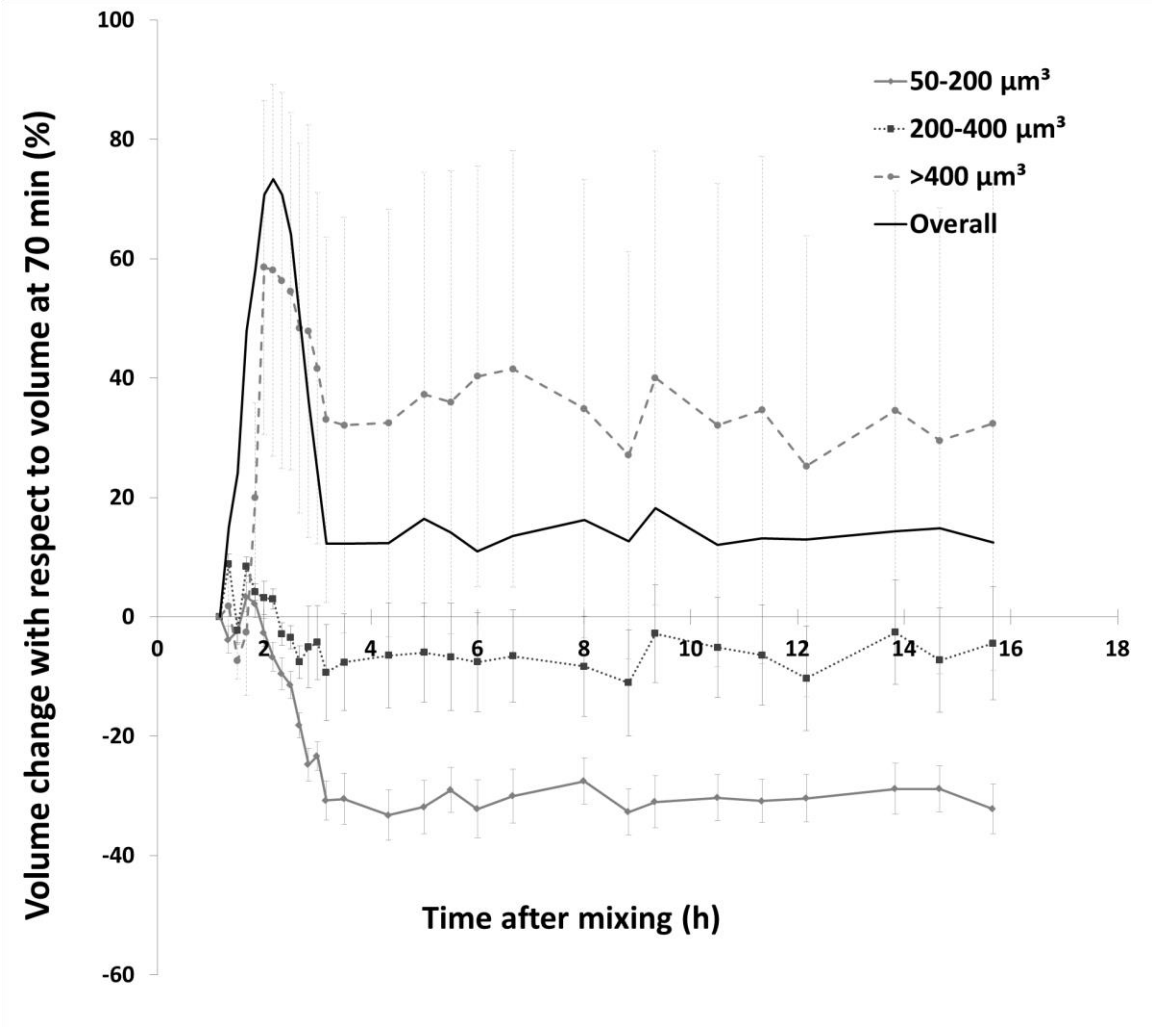

Fig. 3-9. Volume change in single air-filled void in mC_3S paste with w/s=0.70. One standard error has been shown for the different void ranges.

3-3-5-Change in Size Distribution

Further insights can be gained by observing the change in the total volume percentage over time for voids of different volumes as shown in Figure 3-10. These graphs have been normalized to the total volume of voids in the sample in the specific time periods. Over time the volume percentage of small voids increases while the volume percentage of the larger voids decreases. Arrows have been added to Figure 3-10 to highlight this. For example, after 1.2 h of hydration, the mC_3S paste

with w/s = 0.70 had about 18% of the total void volume contained in voids larger than 1000 μm^3. For this same sample only 2% of the volume was found in these voids after 15.7 h. Conversely, after 1.2 h about 9% of total void volume was contained in voids with a volume less than 15 μm^3. After 15.7 h this increased to 17%. Since these voids are so small this would indicate a significant increase in the number of voids. The formation of these < 20 μm^3 voids can be observed in Figure 3-6 and Figure 3-7. Similar behavior is observed in all of the samples made with deionized water. In contrast, negligible change has occurred in voids smaller than 100 μm^3 in the sample made by de-aired water, while the percentage of voids larger than 1000 μm^3 decrease from 37.5% at 0.7 h to 9.2% after 8.8 h. This is likely caused by the infilling of the hydration products over this time period.

The voids between 100-200 μm^3 do not change substantially for samples made with deionized water except OPC w/s = 0.40, which has a finer void distribution before 2.5 h compared to the other samples. This could be caused by the lower w/s.

The change in size distribution of samples made with deionized water is considerable over the first 2.5 h of hydration. However, the size distribution becomes stable during the acceleration period and then shows little change afterward. This matches the total volume changes observed in Figure 3-4 and Figure 3-5.

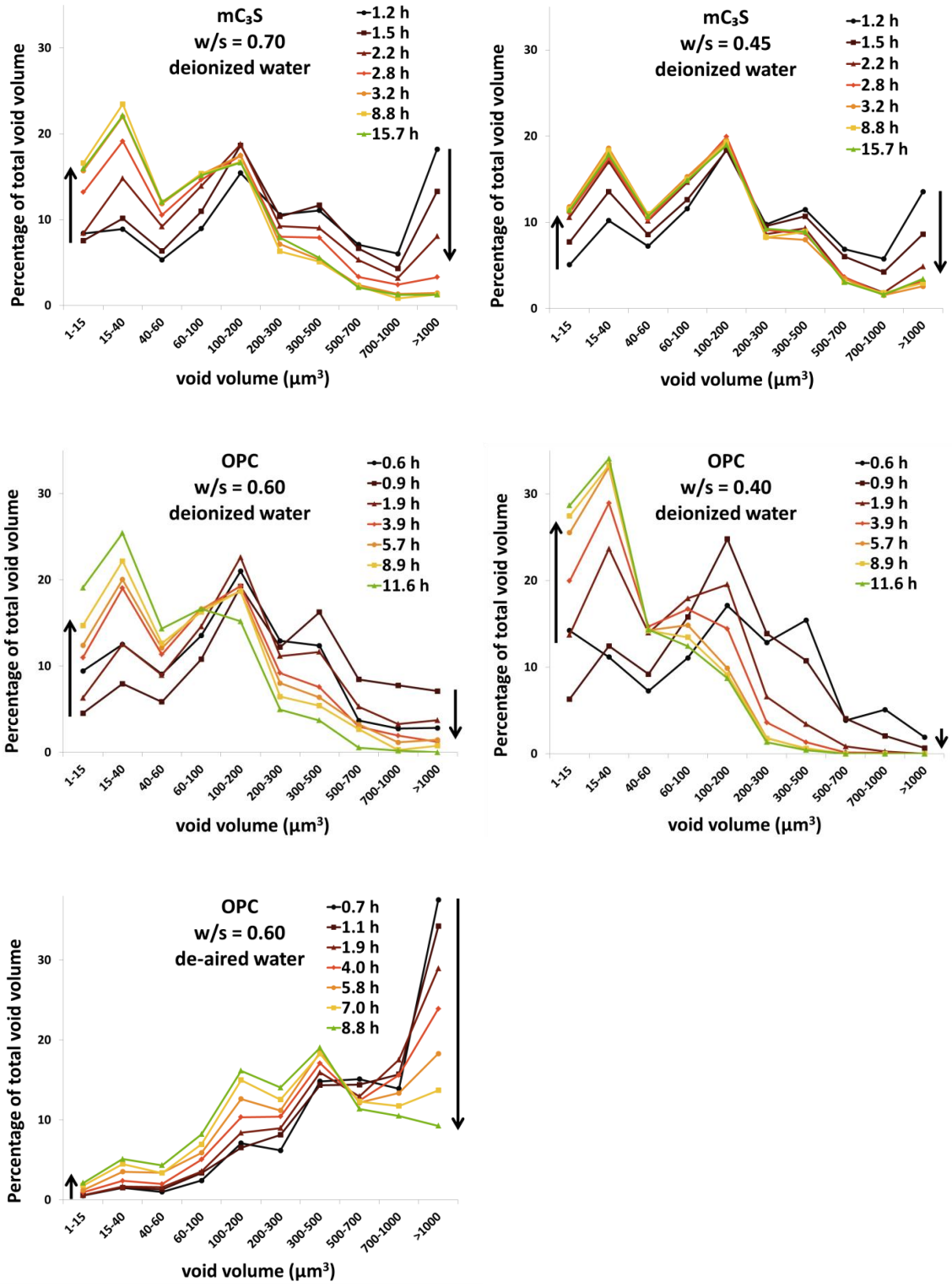

Fig. 3-10. Change in the air-filled void size distribution over time.

3-3-6- Comparison of Size Distribution Change over Time

Figure 3-11 takes the data presented in Figure 3-10 and compares the five samples at the same time periods. The samples made with deionized water were significantly different than the sample with de-aired mixing water. At 1.2 h of hydration, three of the samples have very similar void size distribution; however, the OPC with w/s = 0.40 has 33% of the void volume larger than 100 μm^3. The other three samples have almost double this. This might be caused by the closer spacing of the cement particles from the lower w/s, different compaction level, and the higher chemical reactivity of OPC compared to mC_3S. More observations are needed to better understand this.

At 2.5 h, the amount of air-filled voids larger than 100 μm^3 decreased in all samples. Since the OPC with w/s = 0.40 started with a lower amount of voids greater than 100 μm^3, the decrease in these voids caused this sample to have only 21% voids greater than 100 μm^3. The other samples made with deionized water had between 43%-48% of their voids larger than 100 μm^3. As mentioned earlier, the sample made with de-aired water is different than others and 92% of air-filled voids are greater than 100 μm^3. While this sample has the lowest volume of air-filled voids, the voids greater than 100 μm^3 constitute more than 90% of the air-filled space at 1.2 h and 2.5 h.

After 4.8 h and 9 h of hydration in samples made with deionized water, the samples with close w/s showed similar size distributions regardless of whether the paste was mC_3S or OPC. The samples with a higher w/s were found to have a lower amount of smaller voids and a higher amount of the larger voids after 9 h. For mC_3S with w/s = 0.70 and OPC with w/s = 0.60 between 60% to 64% of voids are smaller than 100 μm^3 and for the OPC with w/s = 0.40 and mC_3S with w/s = 0.45 over 82% of voids are smaller than 100 μm^3 after 4.8 h. These size ranges did not greatly change from 4.8 h to 9 h.

It should be noted that the samples with a w/s of 0.60 and 0.70 had between 27% to 34% voids greater than 100 μm^3 while the samples with w/s of 0.40 and 0.45 has < 11% of the voids in this

size range. This highlights the importance of w/s in the ultimate size distribution of voids in cement paste and will be discussed in more detail in the next section. In contrast, the sample with de-aired water has over 89% and 80% of the air-filled voids > 100 μm^3 after 4.8 h and 9 h, respectively. This highlights the importance of dissolved air on the microstructural evolution of portland cement systems. These mechanisms will be discussed further in this chapter.

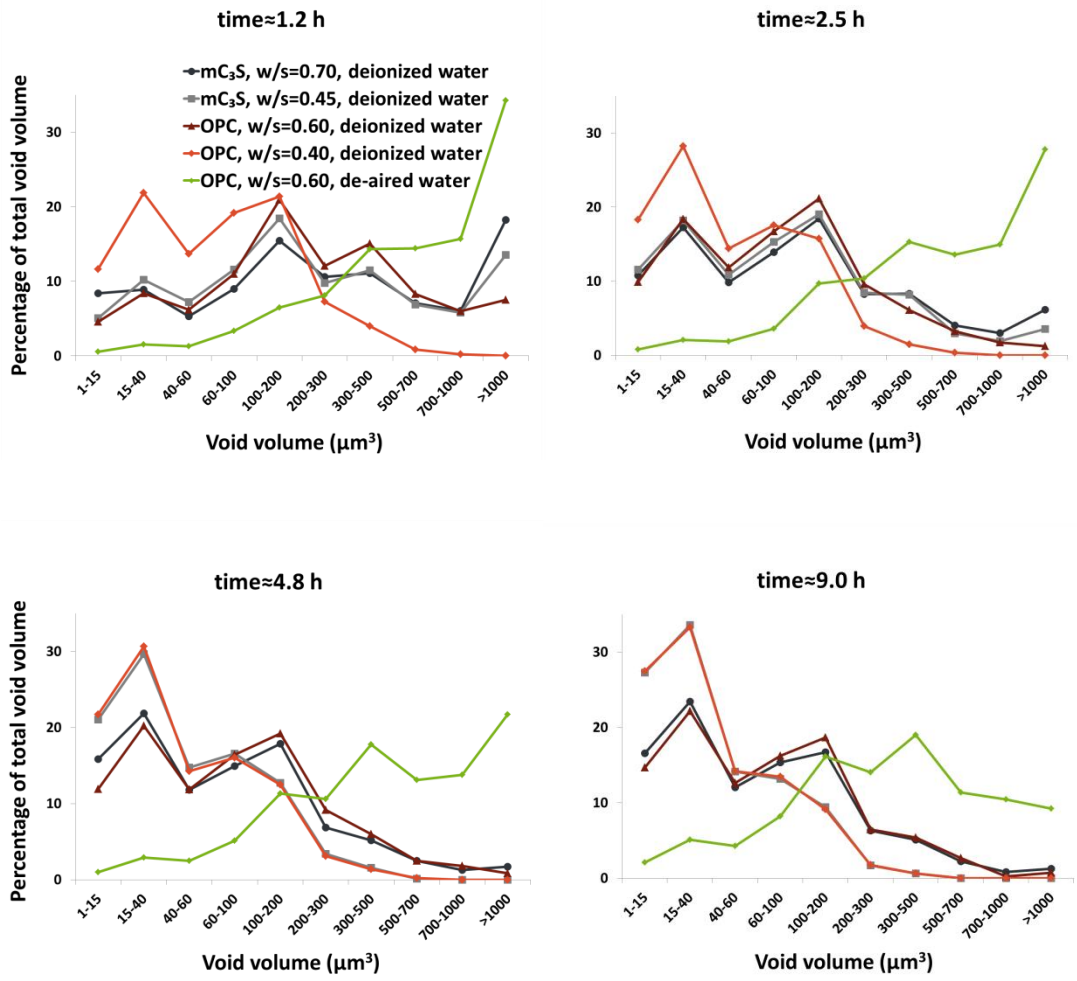

Fig. 3-11. Comparison of size distributions of the examined samples in different time periods.

3-3-7- Discussion of Findings

The trends in volume change shown in Fig. 4 are similar for all samples made with different materials and w/s except for the sample using de-aired water. In addition, the changes observed in the first 3 h of hydration are much higher than the variation in the constant portion of the curves observed after 3 h. This is a useful observation as it suggests that the changes that occur over the first 3 h are significant.

The sensitivity of the results to the segmenting value is examined by altering the threshold value by ±5% for mC_3S with w/s = 0.70. The difference was selected as it was a reasonable range of variation greater than the variability in the segmentation method. The results are demonstrated in Figure 3-12. The results show that while the different threshold values modify the magnitudes of curves, the variation in threshold does not change the general trend or timing of the curves. Therefore, the calculated thresholds seem to be reliable for comparing the different samples and investigating the general behavior in this study.

All tests were conducted in an environment with constant temperature and pressure. Because each scan was only 5 s in length, this means that each sample was only exposed to the X-ray radiation for roughly 7.5 min over roughly 15 h, so the damage from X-ray radiation is expected to be negligible. This is supported by other work done with the same instrument to investigate lithium-ion batteries [113]. In addition, the samples were all prepared in the same way, but the initial investigation was not done at the same time and the samples were investigated for different lengths of time. Despite these differences, the same trends were observed in all of the experiments and the void size distribution in Figure 3-11 was found to be quite comparable at similar time periods. This is not likely a coincidence. Finally, other research has inferred void formation during this time period through acoustic emission measurements. [91]. The sum of this

evidence suggests that the observations in this study are repeatable and not caused by beam artifacts.

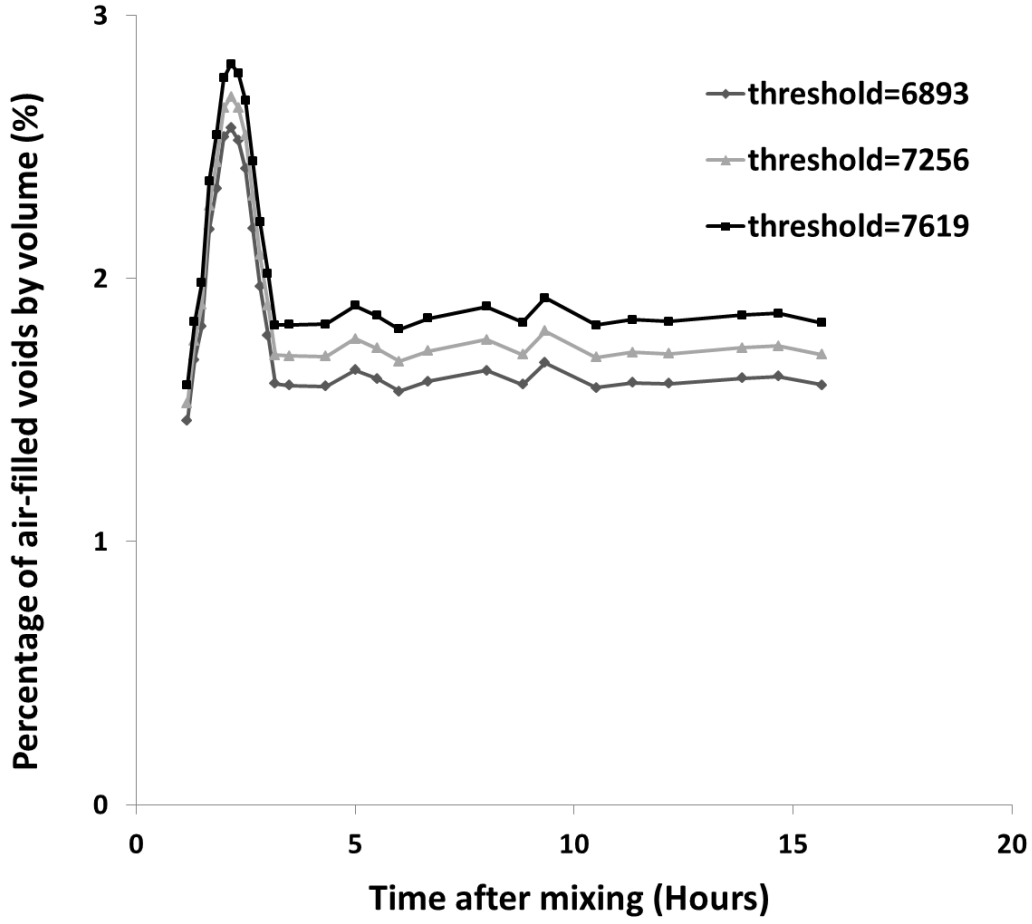

Fig. 3-12. Effect of different threshold gray values on the trend of the curves for mC_3S w/s = 0.70; the calculated threshold value was 7256 based on the segmentation method.

3-4- Proposed Mechanisms

The measurements show that the total volume of air-filled voids in samples made with deionized water increases continuously during the induction period and then decreases as the acceleration period begins. Also, during the acceleration period the voids stop changing in volume. The initial

voids observed may have been trapped by the mixing and consolidation of the sample. However, the formation and evolution of the air-filled voids are likely caused by another mechanism. In this section, two mechanisms will be discussed that could explain the observed changes: chemical shrinkage and change in ionic concentration of the solution. Each will be described and then assessed in terms of their compatibility with the experimental observations.

3-4-1-Contributions from Chemical Shrinkage

Some previous works have inferred some signs of bubble formation in cement paste slurry by observing acoustic events during the early age hydration [91, 114]. These studies have attributed the formation of the air bubbles to chemical shrinkage during early age hydration reactions. According to this hypothesis, water is consumed by the reactions to produce the hydration products. Since the hydration products occupy a smaller space than the original reactants, this will create empty spaces in the paste which are voids. It is further hypothesized that these bubbles that form may decrease in volume over time as water from the surface enters the sample to displace the voids [114]. It is also possible that the creation of the voids causes the paste to be unstable and then collapse and this causes the voids to decrease in size.

The total void content of samples with a lower w/s reached its maximum volume change earlier than the pastes with higher w/s as shown in Figure 3-4. These observations can be explained by chemical shrinkage. As w/s decreases, it is expected that the paste would shrink more and so a higher amount of air-filled void is formed in a shorter time period [83, 84, 91, 115]. The finer size distribution of voids in the low w/s samples may be attributed to the shorter initial inter-particle distance in these paste samples. However, there is minimal chemical shrinkage observed during the times when the void formation in the fCT data is the highest. Also, this hypothesis is unable to explain why the void volume change does not continue when the chemical shrinkage is higher at

the later ages. For example, Figure 3-3 shows that the total chemical shrinkage after 2.5 h is only between 0.0013 mL/g and 0.0111 mL/g but the fCT shows the highest rate of change in void volume in this same period. Moreover, the chemical shrinkage value reaches between 0.0136 mL/g and 0.028 mL/g after 10 h and the fCT shows negligible void change. Because of this, it is not likely that this could be a major cause of the air volume change that is observed in the four samples made with deionized water.

3-4-2-Contributions from Change in Ionic Strength

An alternative hypothesis is the destabilization of dissolved air within the pore solution caused by an increase in the ionic strength. Water typically contains 20 mg/L to 30 mg/L of dissolved air and the amount of air can be higher in water that has been pressurized [116-119]. The solubility of air in water depends on the temperature, pressure, and dissolved ions of the water [120-122]. For all samples, including the one made with de-aired water, the temperature and pressure of the testing environment were constant. Since the X-ray exposure is so short (5 s per scan every 10 min) it should have minimum impact on the sample temperature.

It is widely reported in the literature that the concentration of ions increases during the induction period. Dissolving cement grains will rapidly add significant amounts of ions to the solution in seconds and this will continue over time [44, 46, 52]. Many previous studies have shown that the Ca concentration will increase until reaching a maximum near the end of the induction period [44, 46, 51]. A study using triclinic C_3S with a w/s = 0.70 showed the average Ca concentration of the bulk solution to be ≈ 1700 ppm at the end of the induction period and then drop to ≈ 1450 ppm as the acceleration period begins [44]. The reader should be reminded that these bulk measurements are expected to be lower than local ionic concentrations near reacting anhydrous particles.

Many others have reported that air solubility decreases with an increase in the dissolved ions in the water [119, 123-127]. For example, seawater has a higher propensity to produce foam than fresh water because of the increased dissolved ions [126]. In the literature, this effect is attributed to various factors including the decrease in the surface tension of the water, reduction in the hydrophobic force of attraction between bubbles, and desorption of ions from the air-water interface that ultimately destabilize the bubbles [119, 124-126, 128-131]. While the mechanisms are not well understood, all of the publications agree that the increase in ionic concentration of the solution causes a decrease in the solubility of the air. Therefore, it is reasonable that the dissolved air in the pore solution will become less soluble and will form gas during the induction period. The gas may join other adjacent air-filled space or it may form a new void in water filled space. Based on the size distribution changes in Figure 3-10, it appears that the voids have formed in the water-filled space. This explains the continuous increase in total volume of air-filled voids over the induction period as seen in Figure 3-5.

Furthermore, the most significant data in support of this mechanism is that the sample made with de-aired water does not show a considerable change over time of the air-filled voids. This observation reinforces the importance of dissolved air in void formation of hydrating cement paste.

Calculations were done to estimate the volume of air that may be formed from the dissolved air. This was done by estimating the dissolved air in paste samples with w/s between 0.40 and 0.70 and knowing the densities of water and cement. The mixing water in the experiments was from a water deionizer that used pressure for distribution. If the assumed water pressure is between 1 atm and 4 atm, then the dissolved air in the deionized water is 20 mg/L to 120 mg/L [116-119, 132]. It is estimated that, depending on the w/s, enough air could be created to fill between 0.9% and 6.9% of the total sample volume. All calculations are outlined in the appendix B. These rough values are consistent with the observed void volume changes observed in Figure 3-4 as the

maximum volume changes from the experiments were between 1% and 1.8% for the different samples. Therefore, these calculations suggest that this phenomenon and the proposed mechanism based on the change in ionic concentration are probable. As the acceleration period begins, the ionic concentration decreases as hydration products are precipitated [44, 46, 51-53, 75, 94, 133]. This decrease in ionic concentration will change the solubility of the air and allow the air to dissolve. This could explain why the air leaves the bubbles and dissolves into the solution. This behavior was observed in both volume graphs and 3D images (Figures 3-4, 3-5, 3-6, and 3-7). This volume decrease could also be caused by the formation of hydration products.

It is expected that air would transfer from the smaller bubbles to the larger bubbles through Ostwald ripening [134]. However, it appears that both the large and small voids start shrinking simultaneously. This is not consistent with Ostwald ripening and emphasizes that the changes in the strength of the ionic solution must be a dominant in this mechanism. Furthermore, the changes in spatial and size distribution of air-filled voids may be explained by variation in ionic concentration. It is reported by several researchers that many electrolytes inhibit bubble coalescence above a certain transition concentrations depending on the type of solution [124-126, 128-130, 135-137]. This means that the average size of the air filled space is a function of the local dissolved ion content of the solution. This mechanism is explained further in other publications [131].

Observations from this work support this. The large air-filled voids available in the first collected tomographs as shown by Figures 3-6 and 3-7 suggest that there is more of a tendency for coalescence when the ionic concentration is low at the beginning of the tests. As the ionic concentration increases during the induction period, more bubbles are formed in the paste. The high ionic concentration may hinder coalescence of the bubbles in the slurry. These bubbles are dispersed and have a finer size distribution, because the solution concentration is not favorable for coalescence. This is shown by 3D images and size distribution graphs (Figures 3-6, 3-7, and

3-10). Also, a more uniform spacing of the voids is observed in Figure 3-8 after 3 h of hydration. Unlike the samples made with deionized water, over 80% of voids are > 100 μm^3 in the sample made with de-aired water, and the total volume and size distribution of voids do not change significantly over time.

Furthermore, the observed differences in samples with different w/s can be interpreted based on the change in ionic concentration. The pastes with the lower w/s can potentially contribute more ions to the solution because of the higher solid content in the solution [44]. This might be the reason that the total void content reaches its peak volume earlier then samples with a higher w/s.

The higher ionic concentration of slurry in low w/s samples can also prevent coalescence of the voids formed in the solution [126, 135-137]. Because these voids are less likely to coalesce at high ionic concentrations, they would be smaller and the number formed would be higher in samples with a lower w/s. The void volume, size distribution, and spacing stopped changing after about 3 h. This could be attributed to early stiffening or setting that occurs and may prevent change in the system.

Although this mechanism can explain most of the observations in this study, more details are needed in order to be able to model this phenomenon accurately. The reported solution concentrations in the literature are based on the average ionic concentration of the slurry. This will not be necessarily representative of the local ion concentration near the individual hydrating particles where the voids form. This makes the modeling of this phenomenon difficult. Research efforts are underway to make in-situ with high accuracy and resolution and fill this need.

3-5-Practical importance of the findings

This study follows the evolution of the void system in OPC and mC_3S pastes with different w/s. It is widely understood that the microstructure impacts the performance of materials. These findings suggest that as the microstructure is being formed, there is also a creation of voids that are important to the durability and mechanical properties of the concrete. These results also provide a deeper understanding on how w/s influences the void system of hardened paste and suggest that it contributes to important parameters at the micron scale.

In addition, these observations reinforce the importance of changes in ionic concentration during hydration and how they may impact the volume and distribution of voids within different cement systems. If methods could be developed to better control this void formation then improvements in the resulting properties of concrete could be made. This would allow increased durability, strength, and toughness of the material through manipulation of the hydration process.

While there are still discussions about the mechanisms of increasing ionic strength on void formation [126, 135-137], this technique can provide new insights into the current understanding of void formation and coalescence in other ionic solutions. This phenomenon is important for recognition of interactions in biological system, fluids, and slurries. The application may include drug design, protein crystallization, formulation science, oil recovery, food, and mineral flotation [129, 131, 135].

3-6-Conclusions

In this chapter, fCT was used to study the evolution of air-filled voids in cementitious pastes within the first 16 h of hydration. The change in the total volume and size distribution of air-filled

voids were investigated at a micron resolution. The following conclusions can be drawn for samples made with *deionized water*:

- The total volume of the air-filled voids continuously increased during the induction period. During the same time period, the average distance between individual voids decreased. A considerable amount of voids < 100 μm^3 were observed to form uniformly, while the larger voids decreased in size.

- The total volume of the voids started to decrease over the first hours of the acceleration period and ultimately reached a constant value after approximately 4 h. In this time period the spatial and size distribution of air-filled voids becomes more uniform.

- All samples regardless of w/s and whether they were OPC or mC_3S showed similar volume change and void distribution at comparable times. However, the samples with a higher w/s had a higher portion of voids > 100 μm^3.

The following conclusions can be drawn for samples made with *de-aired water*:

- A significantly lower volume of air-filled voids is observed in these samples and these voids do not significantly change in size or spacing over time.

- The size distribution of the voids in the sample with de-aired water mainly consisted of voids > 100 μm^3 and over time these voids decreased in volume.

- This performance is drastically different than the samples made with the same materials and binder that contained deionized water. This highlights the importance of dissolved air on the mechanism for the void formation.

Mechanisms have been discussed involving chemical shrinkage and changes in ionic strength and their contribution to the formation of air-filled space. The ionic strength mechanism is consistent

with the trends observed for the volume of air formed and the changes in size distribution, and provides insights into why the void formation is not observed in samples with de-aired water.

Furthermore, this study provides insights for improved understanding of void system development during hydration. It is noteworthy that the current study was limited by the resolution of the scans, and therefore only the voids greater than a few microns were considered. The method provides no insight into what occurs at the nanoscale.

Additional work is needed to investigate how other variables such as chemical and mineral admixtures can affect the void formation. This is an important area of ongoing research that has potential to improve the performance of concrete.

CHAPTER IV

STRESS INDUCED DISSOLUTION AND TIME-DEPENDENT DEFORMATION OF PORTLAND CEMENT PASTE

Abstract

While stress-induced dissolution of various minerals has gained attention as an important time-dependent deformation mechanism in other materials, this has only sparingly been investigated in portland cement systems. In this chapter, X-ray Computed Tomography (XCT) is used to make direct observations of the microstructural evolution in cement paste samples under different levels of stress during their first 60 h of hydration. Stiffness and creep measurements are also made while imaging the changes in the microstructure.

The results show that stress applied between 24 h and 60 h alters the hydration kinetics of portland cement. These loads cause early age creep, dissolution of individual particles near the loads, and an increase in stiffness. These measurements provide insights into the microstructural changes that occur due to early age stress applications during the hydration of portland cement.

Keywords: X-ray Computed Tomography; Hydration Kinetics; Segmentation; Creep; Dissolution

4-1-Introduction

Concrete is the second most used commodity in the world after water [1]. The wide availability and inexpensive nature of the required materials as well as desirable mechanical and durability performance make concrete a useful building material. Cement paste is used to bind the aggregates in a concrete mixture together and plays an important role in the strength, durability, and rheology of concrete.

Recent publications suggest a significant coupling between the mechanics and chemistry during the early age reactions or hydration of portland cement paste [138-142]. While stress induced dissolution has gained little attention as a mechanism for stress dependent deformation in cementitious materials, it has been studied extensively in various rocks and minerals [143-150]. Studies over gypsum [145, 149], halite [151], quartz [152, 153], limestone and sandstone [148], calcite [144], and some very soluble elastic/brittle salts (potassium alum and sodium chlorate) [154] all suggest that stress induced dissolution is an important mechanism for viscoelastic/viscoplastic (VE/VP) behavior.

Other publications suggest that stress may impact the thermodynamic equilibrium, hydration kinetics, and/or the VE/VP properties of concrete [142, 155-157]. Previous work measured the impact of stress on hydration of portland cement and C_3S by thermogravimetric analysis (TGA), BET surface area, and mercury intrusion prosimetry pore-size distribution [142]. The work found up to a 14% increase in C_3S degree of hydration of a paste with w/s = 0.50 and loaded by 6.8 MPa at 18 h as compared to a similar non-loaded sample after 48 h of hydration. BET surface area also showed a 15% decrease of the loaded cement paste compared to the non-loaded samples. Other work found that C_3S samples with w/s=0.55 that were cured under pressure showed an accelerated dissolution through measurements with a conductimeter, quantitative XRD, ^{29}Si and ^{1}H NMR, and TGA [155]. They showed that the maximum conductivity is reached

earlier under 850 bar compared to samples hydrated at 350 bar. The conductivity curve reaches its peak after ≈ 100 min when the sample is pressured by 850 bar, while the maximum conductivity was reached at ≈ 200 min for a sample pressured at 350 bar. Others have shown that 15 mm×15 mm×300 mm cement paste beam samples tested in 3-point loading showed approximately 8% higher Young's modulus than the non-loaded samples after 56 days of hydration [139].

Computational models have also been proposed to predict the influence of applied stress on VE/VP mechanisms in concrete. A recent work suggests that the stress induced dissolution of cement particles at early ages controls the time-dependent changes of the apparent VE/VP Poisson's ratio [140]. The significance of stress induced dissolution of cement particles on VE/VP properties of concrete is further discussed in other publications [141, 158, 159].

Although these studies suggest the importance of stress state on the physical properties of materials, these studies are based on either computational models or experimental techniques that make bulk measurements with no direct observation of changes in the microstructure caused by the loading during hydration. X-ray computed tomography (XCT) is a powerful tool to non-destructively visualize the internal structure of materials with a spatial resolution of as small as a few nanometers (nano tomography) [19-21] to several microns (micro tomography) [4, 22, 23]. XCT is widely utilized in medicine to visualize biological samples non-destructively [24, 25]. These methods are similar but the length scales are different. A series of 2-D radiographs are acquired at different imaging angles. A three-dimensional model is reconstructed from 2-D radiographs and the resulting dataset can be used for morphological and quantitative analyses [22]. The variations of gray values in the built images are originated from the electron density and bulk density of the imaged material [26-28]. The gray values of the images can be used for quantitative evaluation of XCT datasets by separating the regions into different constituents. This process is called segmentation.

This chapter uses XCT to study the dissolution rate and microstructural evolution of cement paste over the first 60 h of hydration, both with and without stress. This work makes direct observation of the differences in hydration of systems under different stress levels and simultaneously measures early age creep deformation, and changes in stiffness. The mechanisms and practical significance of the measurements are discussed.

4-2-Method and Experiment

4-2-1-Materials

NIST 168 portland cement (OPC) from the Cement and Concrete Reference Laboratory (Frederick, Maryland) was used to make the paste samples. Composition is presented in Table 4-1. The analysis was completed by ASTM C114 for chemical composition and ASTM C204 for Blaine fineness. The XRD pattern of this powder can be found in another publication [64].

Also, particle size distribution (PSD) was determined by Automated Scanning Electron Microscope (ASEM) [160]. The result showed that 95% of OPC particles are smaller than 8 μm. The PSD graph and more information about ASEM technique can be found in the appendix A.

Table 4-1. Specifications and phase composition of OPC.

	Blaine (cm^2/g)	BET surface area (m^2/g)	Density (gr/cm^3)	Chemical Composition (%)						Phase concentration (%)			
				SiO_2	CaO	Al_2O_3	MgO	Fe_2O_3	SO_3	C_3S	C_2S	C_3A	C_4AF
OPC	4080	NA	3.15	19.91	62.27	5.11	3.87	2.15	3.49	54.5	15.7	8.0	7.0

4-2-2-Sample Preparation

The samples were produced with a water to solid ratio (w/s) of 0.50 (3 g of OPC powder and 1.5 g of deionized water). Water was added to the dry powder, and then they were mixed by a

stainless steel rod 10 times clockwise and 10 times counterclockwise in a glass vial. Next, the vial was shaken with a speed of 1,000 rpm for 3 minutes on a vortex mixer produced by Stuart (Staffordshire, UK). This mixing procedure ensures that the slurry is well-mixed and consistent in all samples produced.

The slurry was placed in manufactured polyethylene cylindrical molds with a diameter of 1.19 mm to 1.58 mm and a height of 9 mm. The variable diameter was caused by differences in manufacturing. The mold was then gently tapped by a steel rod to compact the samples. A wet paper towel was then placed on the mold for 24 h to keep the sample moist and provide a favorable condition for curing. All cylindrical samples were carefully demolded after 24 h and covered by petroleum jelly to minimize the loss of moisture during data collection. This means that moisture is likely present to promote hydration. The entire width of the samples is imaged, but the analysis is performed on a region of interest that is 800 μm in diameter. This region was chosen as it was away from the boundaries which may potentially have artifacts or inadvertently exposed to the surrounding environment. Approximately 10 identical samples were produced from each batch and the best three were used based on visual examination.

4-2-3-Loading Setup

The loading stage used is shown in Figure 4-1. The stage uses gravity loading through a platen and lead weights. The stage is calibrated by a load cell accurate to 0.1 g. The top and bottom 500 μm of the sample is embedded in the steel platen and fixed by epoxy in order to ensure sufficient load transfer, equal load distribution, and to minimize the movement of the top of the sample. Because the top portion was embedded in the platen no information can be reported for this region.

First, two cylindrical specimens were broken by loading them axially with the loading stage to determine their 24 h compressive strength (f_{1day}). Then, another sample from the group was placed on the loading stage and XCT was used to collect three consecutive tomographs with a resolution of 1.45 μm/pixel. Each tomograph, except the non-loaded sample, took approximately 11.5 h to collect. A 0.5 h rest period between each loading step was used to allow for deformations to occur in the load stage and sample. Because of this, each tomograph was captured between 24 h to 36 h, 36 h to 48 h, and 48 h to 60 h after hydration.

One sample was loaded with only the platen for the three time periods. The platen caused 12% of the measured f_{1day} stress. This sample is called OPC-PL. Three samples were loaded with the platen between 24 h to 36 h, then 50% of the f_{1day} stress between 36 h to 48 h, and then the platen again between 48 h to 60 h. These samples are known as OPC-1, OPC-2, and OPC-3. The load was held constant during the collection of each tomograph by the lead weight. The platen caused between 8% and 15% of the f_{1day} depending on the sample diameter. Single radiographs at a fixed angle from each tomograph were used to measure the deformation of the sample while under a fixed load or the creep strain. These measurements will be discussed in more detail later in the chapter.

The reader is reminded that not all samples had the same diameter because of differences in fabrication. These levels of stress were selected because they were thought to be high enough to create a measurable change in hydration kinetics without causing damage to the samples. No cracking was observed in the 3D tomographs and so these assumptions appear to be sound.

One sample that was never loaded was investigated as a control. This sample is labeled OPC-NL. The scan time for this sample was 6.5 h for each tomograph. This scan time was shorter because the instrument could be reconfigured so that it was closer to the sample when the load stage was

not used. Because the scan time was shorter the time between the tomographs was extended to 5.5 h so that all of the tomographs started at the same time for all the samples examined.

After completion of the last tomograph at 60 h of hydration, the sample was loaded to 50% of f_{1day} three times and the deformations were measured with radiographs with a resolution of 300 nm/pixel. This allowed the Young's modulus to be estimated by using a linear regression model with the stress and strain data.

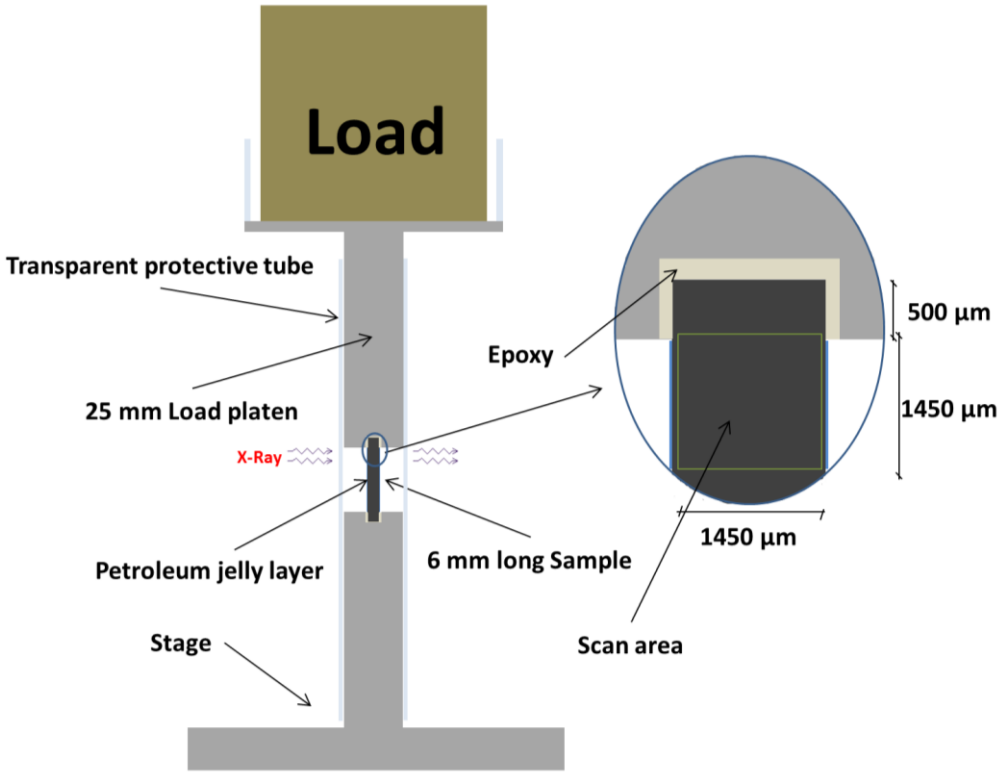

Fig. 4-1. Schematic of the loading setup.

4-2-3- X-Ray Computed Tomography (XCT)

The experiments were performed by a ZEISS Xradia 410 Versa with photon energy of 55 keV and a resolution of 1.45 µm/pixel. This high resolution limits the scan window to 1.45 mm below the surface of the platen as shown in Figure 4-1. The details of the XCT machine settings can be

found in Table 4-2. Also, XMReconstructor-Cone Beam-10 software was used to reconstruct the data into a stack of 2D slices.

The gray value in the radiographs correlates to the transmitted X-ray intensity (I) according to the Beer-Lambert law:

$$\frac{I}{I_o} = \exp(-\mu_m \rho x) \qquad (4\text{-}1)$$

where I_0 is the original intensity of the X-ray beam, μ_m is the mass attenuation coefficient, ρ is density, and x path length [68]. Therefore, difference in gray values can be used to segment the acquired images into different constituent phases.

Table 4-2. Instrument settings for XCT instrument.

Resolution	1.45 µm/pixel
Source energy	55 keV
Optical magnification	10X
Total scan time	11 h: 30 min
Number of projections	2800
Exposure time	12.5 s

4-2-4-Image Processing and Segmentation

The analysis of the 3D datasets was completed by MATLAB codes, ImageJ, and Amira 4.1.1 software. First, a median filter with a radius of 2 pixels was used to smooth images and reduce noise. This filter is widely used in signal processing because of its ability to reduce noise while preserving edges. The details of the application and algorithm of the filter can be found in other publications [65, 66, 111, 161, 162]. The gray values of the second and third tomographs were transformed so that their histograms matched with the first tomograph. The transformation function is determined after obtaining the histograms and cumulative distribution functions of the

tomographs and following a procedure described in [163, 164]. This minimizes gray value shift from one tomograph to another. No information can be given from the top 500 μm of the sample since it is embedded in the platen. Also, the first 10 slices (14.5 μm) near the load platen were discarded because of artifacts caused by the platen. Next, the Otsu method was used for segmentation. This method is based on minimizing the mean square errors between the original and binarized images. More details about the method can be found in the literature [69, 165, 166].

The paste samples consist of anhydrous cement particles, hydration products, and voids. In a tomograph collected from a cement paste sample, anhydrous cement particles usually have the highest X-ray absorption (highest gray values), while voids have the lowest absorption (lowest gray values) [4, 167]. The term "high-absorption material" is used in this chapter to describe a combination of anhydrous cement particles and dense hydration products with X-ray absorption similar to or higher than the anhydrous cement particles. To segment the high-absorption materials from the rest of the paste, certain regions of interest (ROI) with high amounts of high-absorption materials were isolated from different tomographs and the threshold values of these regions were determined by the Otsu method. Figure 4-2 shows an example of this process. This was repeated for several regions and the average of at least 40 ROIs was used to segment high-absorption materials in all three collected tomographs. Figure 4-3 demonstrates the satisfactory performance of the utilized segmentation method for one slice in different loading conditions in OPC-2 sample. This data is provided to allow the reader to judge the quality of the segmentation. The raw data is shown in the top row and the segmented data is shown beneath it.

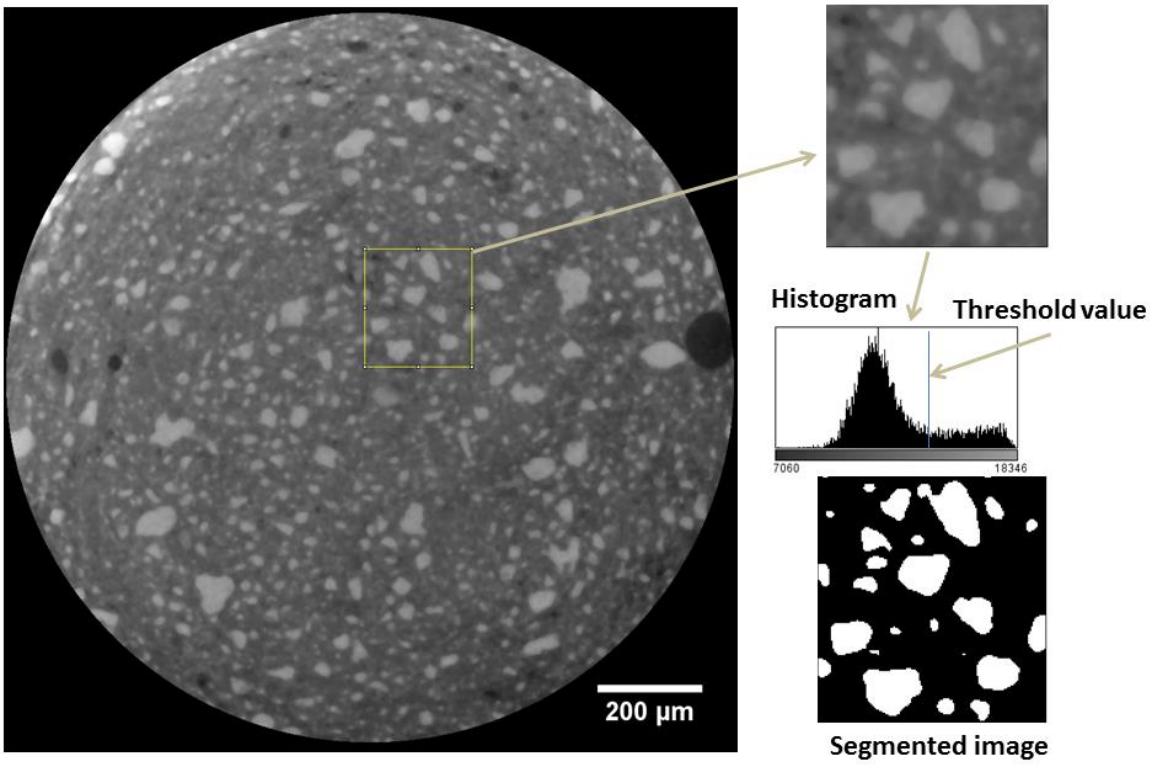

Fig. 4-2. An overview of a raw image of a slice and segmentation steps for high-absorption materials in an ROI.

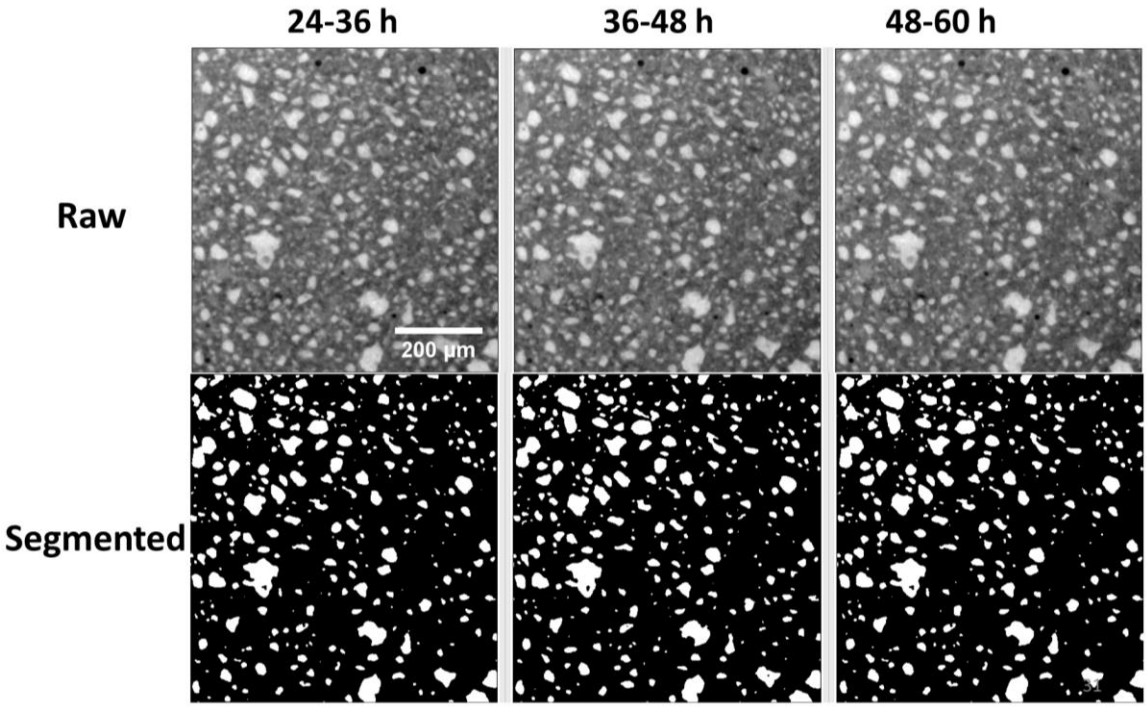

Fig. 4-3. One slice from OPC-2 sample before and after segmentation of high-absorptions in three different time periods.

4-2-5-Deformation Calculation from Radiographs

Since the steel platen has a high X-ray absorption compared to cement paste this can be used to segment the steel platen in the images. Since the platen and sample are in intimate contact, the movement of the platen could be used to calculate the deformation of the sample. The strain of the sample is calculated by dividing the sample deformation by the sample length.

The deformation of the samples was determined over the scanning period from the radiographs collected at a fixed angle every ≈ 14 min while the sample was under load. The strain is calculated with respect to the initial length of the sample at the beginning of each scan. The strain values discussed throughout the chapter were taken as zero at the beginning of each scan.

Because of the shorter scan time for the non-loaded sample, the strain data is only available for the first 6.5 h. Also, the strain rate for the first loading period is taken between 30 h and 36 h because of early age movement of the frame. This is discussed in more detail in the results section.

4-2-6-Volume Change of High-Absorption Materials

The percentage volume change of the high-absorption materials in each tomograph is calculated by:

$$\Delta V = \frac{V_2 - V_1}{V_1} \times 100 \quad (4\text{-}2)$$

where V_1 and V_2 are volumes of the high-absorption material in the first and second collected tomographs, respectively. This calculation is done for isolated high-absorption materials. These high-absorption materials are anhydrous cement particles and any high-absorption hydration products. These volume changes are plotted with respect to distance from the top of the sample. Two sets of volume change graphs are produced:

1. Volume change of high-absorption material from the first loading stage (ΔV_a) measured between 24 h to 36 h (V_1) compared to the second loading stage measured between 36 h and 48 h (V_2):

$$\Delta V_a = \frac{V_2 - V_1}{V_1} \times 100$$

2. Volume change of high-absorption material from the second loading stage (ΔV_b) measured between 36 h to 48 h (V_2) to the third loading stage measured between 48 h to 60 h (V_3):

$$\Delta V_b = \frac{V_3 - V_2}{V_2} \times 100$$

The number of individual high-absorption materials used for these calculations is between 4,000 and 5,000 for each sample. More details about the number of regions investigated can be found in the appendix C. If a negative number is found for this calculation, then it means that this high-absorption material has decreased in volume. This would occur when the particle is primarily dissolving. If a positive number is found then that means there is more growth of high-absorption hydration products than dissolution.

4-3-Results and Discussion

4-3-1-Stiffness

Table 4-3 shows the calculated Young's modulus for the samples after 60 h of hydration. The stress history and the coefficient of determination (r^2) are also reported. Since the r^2 values are close to one, this shows that a linear model is appropriate for this data. Data is reported for all samples but not for the sample that was not loaded. For the non-loaded sample the platen was not fixed to the sample until right before the modulus testing at 60 h after hydration. For the other samples the epoxy was placed at 24 h of hydration. This means that the epoxy in the loaded samples has a longer time to react before loading. This caused the stiffness of the epoxy to be very different between the two samples and this made it not possible to compare the results from the tests.

Samples OPC-1, OPC-2, and OPC-3 have quite similar modulus values and had similar stresses during hydration. These samples received higher loading and also had a higher modulus compared to the samples that were only loaded with the platen. The higher loaded samples had a modulus that was between 1.36 to 1.64 times higher than the sample that was only loaded with

the platen. This suggests that the higher applied load between 36 h and 48 h of hydration had a significant impact on the mechanical properties. These changes in mechanical properties could be caused by the load changing the kinetics of hydration and therefore the microstructure of the materials may be different. This will be further investigated in the upcoming sections.

Table 4-3. Stress history and modulus of elasticity after 60 h.

Sample code	Sample diameter (mm)	Stress history (MPa) and percentage of f_{1day}			Young's modulus (GPa)	r^2
		24-36 h	36-48 h	48-60 h		
OPC-NL	1.50	0	0	0	N/A	N/A
OPC-PL	1.28	2.5 (12%)	2.5 (12%)	2.5 (12%)	3.9	0.99
OPC-1	1.19	2.9 (15%)	9.7 (50%)	2.9 (15%)	5.3	0.99
OPC-2	1.58	1.6 (8%)	10.7 (50%)	1.6 (8%)	6.4	0.97
OPC-3	1.57	1.6 (9%)	10.4 (50%)	1.6 (9%)	5.6	0.98

4-3-2-Time-Dependent Deformations

Figure 4-5 shows the change in strain over time during each tomograph. This is also known as the creep strain. The strain is calculated by dividing the change in length by the original length of the sample. The zero point on the graph corresponds to the point of first measurement for that loading stage. This was done because the deformation before and just after applying the load was not measured. This means that the values in Figure 4-5 are not absolute and are instead are change in strain.

The graph shows the behavior during three different loading stages. Each loading stage is separated by a vertical dashed line. The stress applied to each sample is shown near the top of the graph. A negative strain value means the sample is shrinking and a positive value means it is

swelling. Samples OPC-1, OPC-2, and OPC-3 are shown with solid lines, while OPC-PL and OPC-NL are shown with dashed gray lines.

The samples that were loaded showed an initial strain up to 240 με over the first 3 h of measurement. This initial growth could be caused by the thermal changes in the loading stage from placing it in the XCT. A heater is used in the XCT to keep the internal chamber at 28 °C. This improves the image quality by reducing movement of the imaging stage. The load stage was at room temperature before placing it in the instrument. Although the room temperature was not measured it was roughly 23 °C. The coefficient of thermal expansion of steel is reported to be 12×10^{-6} $(°C)^{-1}$ [168]. This means that if the frame temperature raised by 2 °C then this could cause a change of roughly 240 με. This value is similar to what was observed in the testing and so this is a probable explanation for the observed change in strain. This highlights the care that is needed in making measurements in these experiments.

The strain rate of a sample is found from the slope of a linear model fit to each data set. Because of the initial movement of the load frame from temperature changes a linear model is fit between 30 h and 36 h. These results are presented in Table 4-4. Also, the strain at the end of each load stage or 35.5 h, 47.5 h, and 59.5 h is used to compare the samples. A negative value means shrinkage while a positive value is growth. The data for the first loading stage should be interpreted with care because of the early age movement from temperature changes. The reader should be reminded that not all of the samples were of the same diameter and so this caused different stresses even though the samples carried the same load. Since these samples were small these differences can cause significant changes in the stress.

In OPC-NL the strain rate is very close to zero for all loading stages. While some growth (≈ 50 με) was observed between 48 h and 60 h, this was within the resolution of the scan and so it is not

significant. Since this sample is not loaded then these small changes are in line with what is expected.

The OPC-PL sample is under a constant 2.5 MPa or 12% of f_{1day} between 24 h to 60 h or for all three of the tomographs. For each scan period the slope of the line or the strain rate decreases over time despite the load being the same. Between 24 h and 36 h the strain rate is 58.4 με/h, then between 36 h and 48 h the strain rate decreases by 50% to 29.4 με/h, and then between 48 h and 60 h the strain rate decreases by 22.4% to 22.8 με/h. This is likely caused by a refinement of the microstructure over time caused by hydration.

For samples OPC-2 and OPC-3, the samples, between 24 h to 36 h were loaded at 1.6 MPa and OPC-1 and OPC-PL were loaded at 2.9 MPa and 2.5 MPa, respectively. This difference in the stress level is caused by ≈ 25% smaller diameter of OPC-1 and OPC-PL compared to OPC-2 and OPC-3. The results show that the strain rate of samples with the 70% higher loading is almost half of strain rate in OPC-2 and OPC-3. This result is not expected but has been observed in multiple samples. The difference in diameter can alter the stress distribution in the samples and this may cause the variation observed. The stress distribution and diameter relationship is further discussed in later sections. As mentioned earlier, the initial growth observed can influence both the calculated strain and strain rate (slope of the lines) and so this comparison should be interpreted with care.

As the loading is increased to 50% of f_{1day} for OPC-1, OPC-2, and OPC-3 between 36 h to 48 h, the creep deformations increase in magnitude. The differences between the observed strains in OPC-1, OPC-2, and OPC-3 could be caused by a difference in stress history.

The creep strain at the end of the second loading period is between 2,190 με and 2,650 με. Previous work done with cement pastes with w/s = 0.50 and stressed to 30% of f_{1day} at 24 h showed a total strain of 1614 με after 3 days of loading [138]. These differences could be

explained by differences in stress and time of loading. This work applied 50% of f_{1day} at 36 h and the reference used 30% of f_{1day} at 24 h.

The creep strain in the higher loaded samples is between 7.6x and 9.2x greater than the creep strain of the OPC-PL and the strain rate is between 5.9x and 6.8x of OPC-PL with a load of only 12% of f_{1day}. These results show the significant increase in early age strain as stress is increased to 50% of f_{1day}.

After reducing the stress for OPC-1, OPC-2, and OPC-3 between 48 h to 60 h, a creep strain of less than <400 με is observed under the platen weight. This is a reduction in the creep strain by 2.7x and 4.7x compared to 24 h to 36 h. Also, the strain rates for all of the samples between 48 h to 60 h were found to be between 2.9x and 8.9x smaller than the strain rates measured between 24 h to 36 h. These differences in behavior are likely caused by changes in hydration rate and the resulting microstructure from the external loading. Some insights into this are provided in the next section.

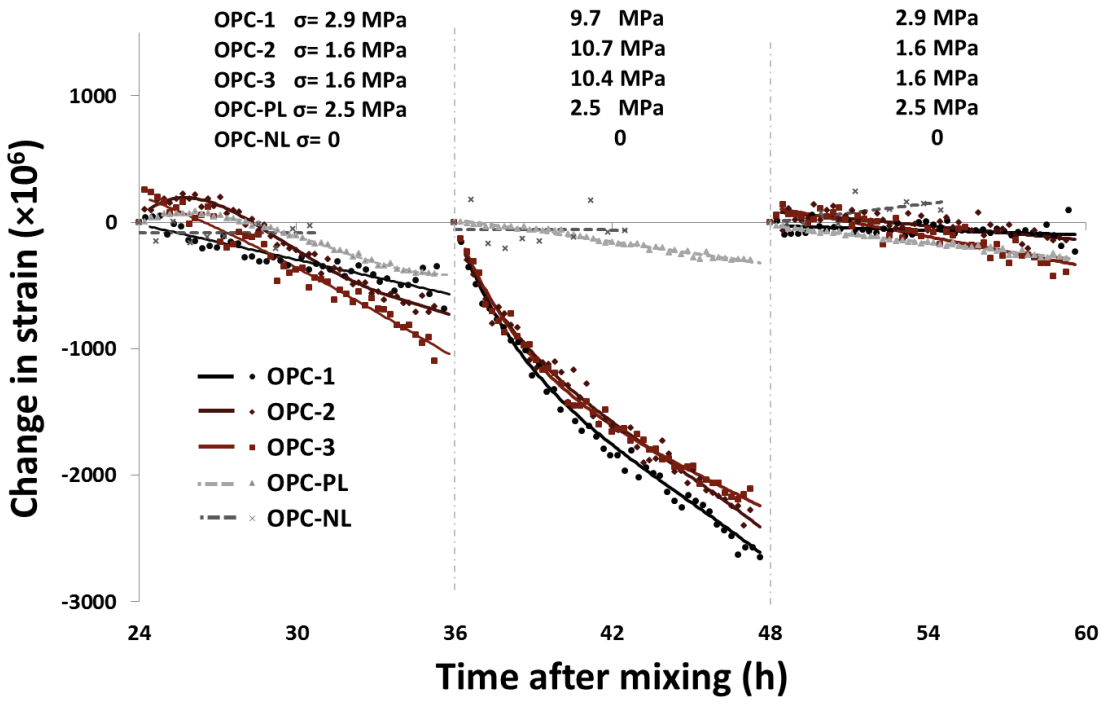

Fig. 4-5. Change in time dependent strain during the scanning of samples, the stress applied on the sample is shown at the top of the graph. The zero point on the graph corresponds to the point of first measurement.

Table 4-4. A summary of different strain values from the change in time-dependent loading tests shown in Figure 4-5. Negative values correspond to shrinkage and positive values are for swelling.

sample code	Time for tomograph collection								
	24 h - 36 h*			36 h - 48 h			48 h - 60 h		
	applied Stress (MPa)	strain rate (με/h)**	last measured strain (με)	applied Stress (MPa)	strain rate (με/h)	last measured strain (με)	applied Stress (MPa)	strain rate (με/h)	last measured strain (με)
OPC-NL	0	-1.1	-28	0	-1.2	-65	0	29.1	97
OPC-PL	2.5	-58.4	-402	2.5	-29.4	-289	2.5	-22.8	-283
OPC-1	2.9	-40.1	-687	9.7	-201.5	-2650	2.9	-4.5	-235
OPC-2	1.6	-91.0	-669	10.7	-183.9	-2397	1.6	-19	-141
OPC-3	1.6	-116.6	-1097	10.4	-174.4	-2190	1.6	-39.4	-395

* The initial growth observed in strain can significantly impact the calculated strain rate and ultimate strain at this time period.

**The slope is calculated for data between 30 h and 36 h.

4-3-3-Volume Change of High-Absorption Material

4-3-3-1-Change between the First and Second Load Stage

Figure 4-6 shows the change in volume percentage of high-absorption materials with respect to distance from the top of the sample between the first load stage between 24 h and 36 h and the second load stage between 36 h to 48 h. Each point on the plot shows the average volume and the standard error of the high-absorption material within a given region. A second degree exponential model is also shown. The intensity of stress applied during the first and second loading stage is

also included in the legend. Some locations are identified by horizontal dashed lines. These indicate locations of individual high-absorption materials that will be discussed later.

The results of the samples loaded to 50% f_{1day} are shown with dashed-lines, while the results of OPC-PL with a constant stress of 12% f_{1day} and OPC-NL is shown with solid lines. The load platen covers the top ≈ 500 μm of the sample and so no information is available from this region.

In the non-loaded sample, OPC-NL, and lightly-loaded sample, OPC-PL, the observed changes were less than ±1%. This means that these samples either showed very little change in the high-absorption material over the same period or the changes are below the resolution of the technique.

The samples loaded to 50% of f_{1day} have a higher percentage change of high-absorption material within 900 μm from the sample surface. These changes are not likely caused by elastic deformations. The Young's modulus of anhydrous cement particles are reported to be over 100 GPa [169]. At the level of stresses applied on these samples this would cause deformations of only a few nanometers. This means these observations are not likely caused by elastic deformation of these particles.

It is more probable that the volume change of the high-absorption material could be caused by the anhydrous particles showing a higher rate of dissolution from the external stress in this region. The maximum decrease in volume of high-absorption material was 3.9%, 6.3%, and 3.5% for OPC-1, OPC-2, and OPC-3, respectively. This variation may be caused by the complex nature of cement paste and differences in stress history and strength of the examined samples. In addition, the particles with different shape, size, orientation, and location might experience different levels of stress. More insights on the impact of stress on the kinetics of hydration will be provided in discussion section.

For OPC-1, OPC-2, and OPC-3 the volume change of the high-absorption material was almost constant after 600 μm, 900 μm, and 750 μm for OPC-1, OPC-2, and OPC-3, respectively. This

suggests that the impacts to the microstructure from the stress are more significant closer to the load application. The differences in the samples could be caused by differences in geometry and strength of samples as this will impact the stress distribution. This will also be discussed in more detail in later sections.

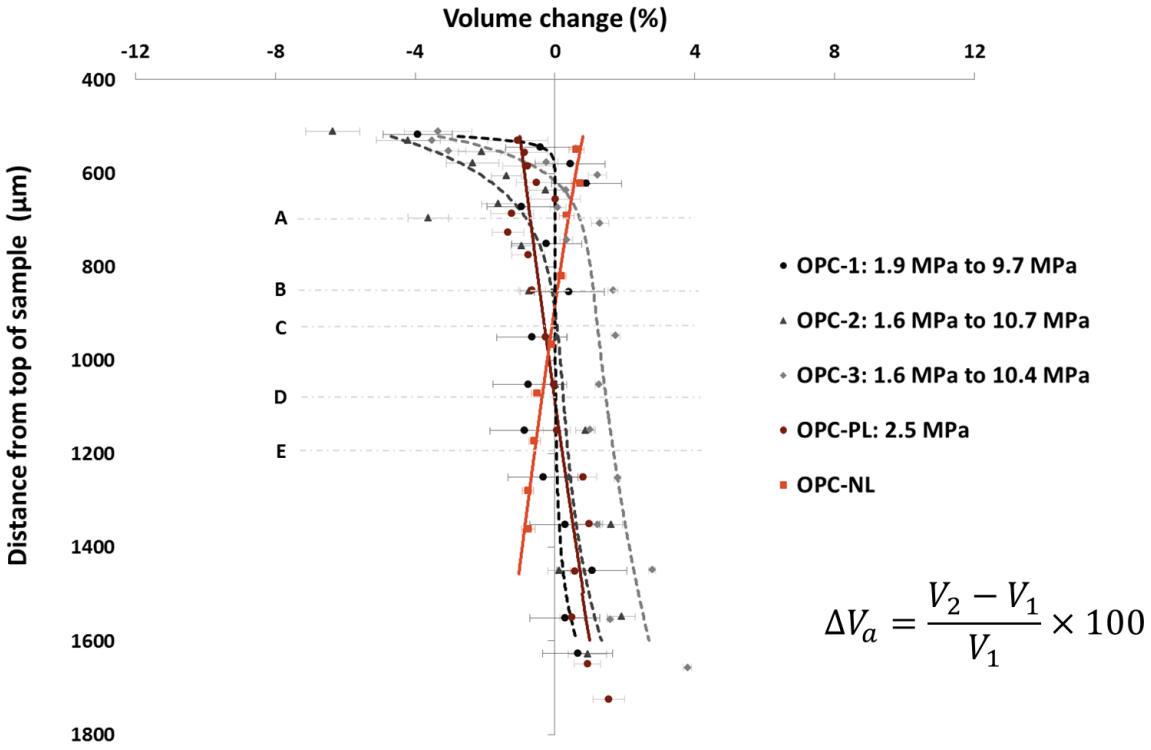

Fig. 4-6. Volume change of individual high-absorption materials with respect to their distance from the top of the samples between the first loading stage (24 h to 36 h) and the second loading stage (36 h to 48 h).

4-3-3-2- Change between the Second and Third Load Stage

The volume change from the second loading stage (36 h to 48 h) and the third loading stage (48 h to 60 h) of individual high-absorption materials is shown in Figure 4-7. All the samples show very little volume change except for some growth of OPC-2 near the load platen. However, this

growth is very small and just greater than the sample that is not loaded. These measurements show that there is little change in the high-absorption materials from removing the loading.

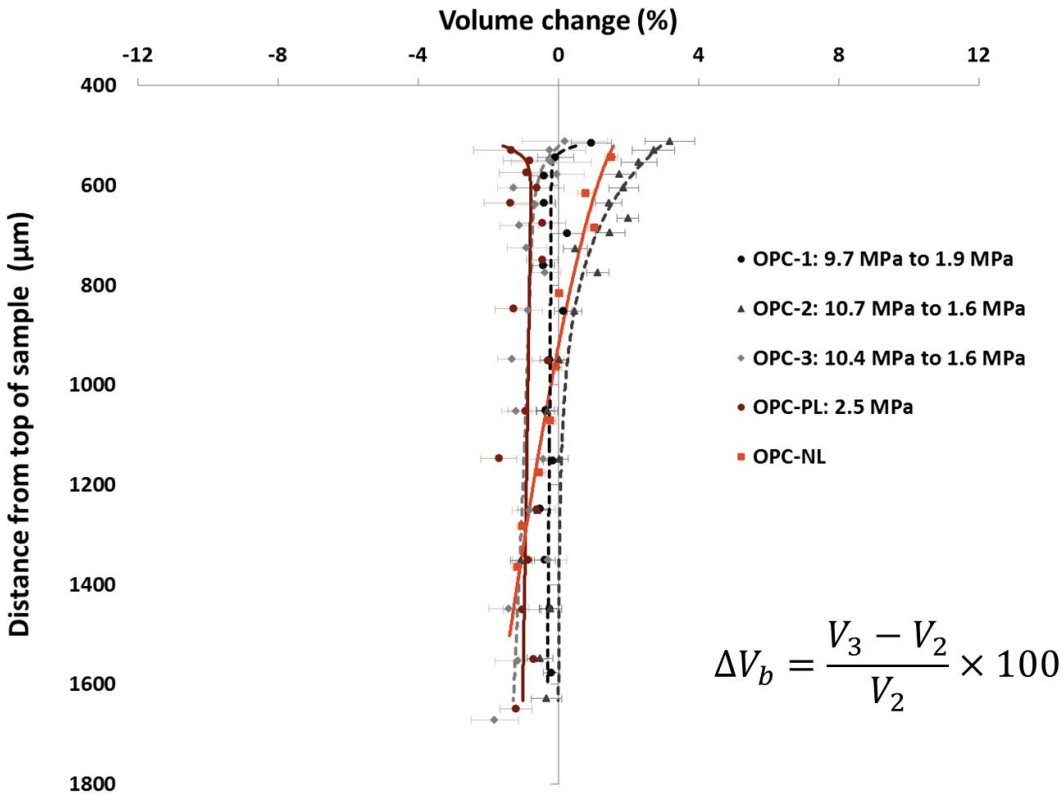

Fig. 4-7. Volume change of individual high-absorption materials with respect to their distance from the top of the samples from the second loading stage (36 h to 48 h) and the third loading stage (48 h to 60 h).

4-3-3-3-Three-Dimensional Investigation of Individual High-Absorption Materials

Five individual high-absorption regions from sample OPC-1 and OPC-2 at different distances from the top of the sample are shown in Figure 4-8 with the location of the particles shown in Figure 4-6. The time period and the stress applied are reported as well. The platen covers the top ≈ 500 µm of the sample and therefore no material could be investigated in this region. The

reviewer should be reminded that the isolated high-absorption regions are made up of anhydrous OPC particles but also could contain some hydration products with high X-ray absorption. The boundary of the high-absorption material between 24 h to 36 h is shown in light gray. Regions that appear to have decreased X-ray absorption when compared to the first tomograph are shown in green. These regions are regions where part of the high-absorption material is no longer detected and this is likely a region of dissolution. Regions with increased X-ray absorption are shown in dark gray. These are regions where hydration products of increased X-ray absorption may have formed.

The individual high-absorption materials show similar trends to the volume changes in Figure 4-6 and Figure 4-7. For example the first high-absorption particle is located at 680 μm from the top of the sample and it shows a decrease in volume of 3.7% under a 10 MPa load and then it appears to grow by 1.5% after the load is removed to 2 MPa. The other isolated high-absorption materials that are closer than 950 μm show similar trends with a decrease in magnitude with distance from the point where the load is applied. The high-absorption material that was greater than 950 μm showed a change of less than 1% by volume.

The 3D renderings show that the regions near the surface of the anhydrous particles both increase and decrease in X-ray absorption. These areas of local dissolution may be attributed to higher crystallographic defects or mechanical damage caused by grinding as suggested in other publications [2, 3, 27, 36, 74-77].

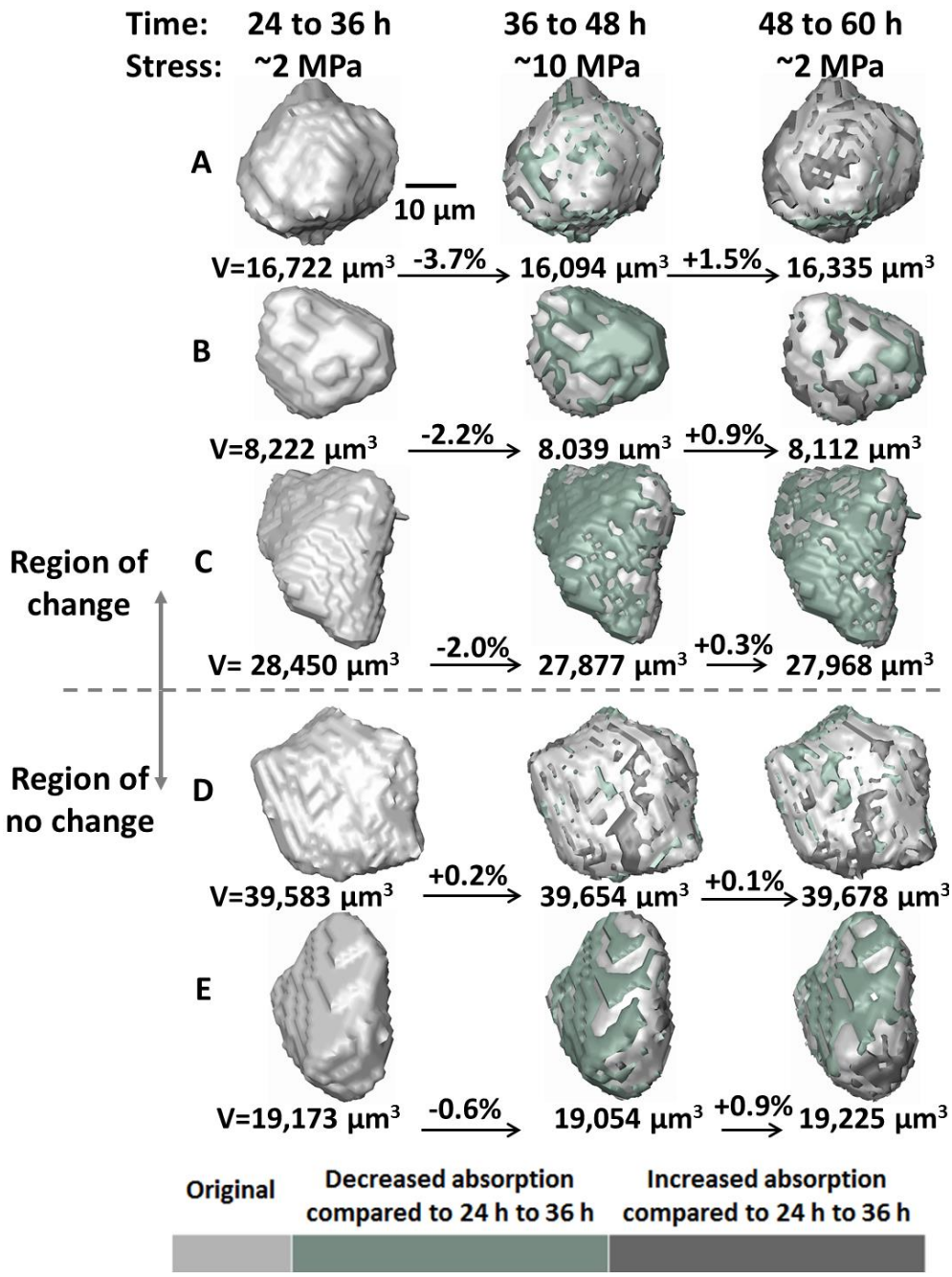

Fig. 4-8. Three dimensional models of individual high-absorption materials in sample OPC-1 (A,B,C, and E) and OPC-2 (D).

4-4-The Relationship between Physical Properties and Microstructural Changes

All samples loaded by 50% of f_{1day} between 36 h and 48 h had a Young's modulus that was 1.6x higher than the sample that was only loaded with 12% of f_{1day}. This apparent stress-induced increase in stiffness is also observed by others [138, 139, 142] and is at least partially attributed to the higher degree of hydration and compaction of the system caused by the loading. The higher loaded samples also showed an increased creep strain as compared to the samples with lower stress. These lower values are expected because of the higher stresses that are applied; however, these higher strain rates could cause changes in the hydration rate and the resulting microstructure.

Based on previous literature about stress dissolution and the modification of thermodynamic strain energy, it is expected that a higher stress would cause changes in the rate and volume of the hydration products that form. Although this work could not observe the nature of the hydration products because of limitations in the measurement methods, observations were made that suggest that this is likely occurring.

For example, the high-absorption materials found within 400 μm from the load platen for the samples that were loaded to 50% of f_{1day} showed a higher amount of dissolution compared to the particles farther than 400 μm from the platen. This difference in the amount of dissolution can be caused by a stress gradient. The stress gradient is caused by elastic equivalence of load or Saint-Venant's Principle [170-173]. This concept suggests that the magnitude of stress is several times higher near the point of load application because the load is not applied uniformly at the surface of the sample and the stress becomes uniform some distance away from the load point [170, 171]. It is also reported that this unequal pressure distribution extends approximately one diameter away from the loaded end in a stressed cylinder [174]. Thus, the stress distribution will depend on the diameter of cylinder.

In addition, The Riecke Principle states that under crystals under pressure have a greater solubility compared to a stress-free crystal [175]. Because anhydrous cement is a crystal, it is expected to follow this principle. The results obtained from this study showing the higher dissolution of high-absorption materials near the load is consistent with what is expected to occur according to both Saint-Venant's and Riecke Principles. The high-absorption materials that are under a higher stress level lost volume or dissolved faster than these same regions away from the load. In addition, the minimal changes observed in the non-loaded sample (OPC-NL) and the small changes observed in the lightly loaded sample (OPC-PL) as shown in Figure 4-6 and Figure 4-7, reinforces this concept that the magnitude and sample geometry impacts the hydration kinetics where the magnitudes are great enough.

As suggested by Saint-Venant's Principle the diameter of the sample is expected to impact the stress distribution and hence the dissolution of the high-absorption materials. OPC-1 has a diameter that is 25% smaller than OPC-2 and OPC-3 and also shows about 30% difference in the height of the region that shows a higher dissolution rate of high-absorption materials. This observation is also consistent with Saint-Venant's Principle.

Also, the investigation of changes of the high absorption material of isolated material shows that the changes are not uniform. This is in accordance with recent publications suggesting etch pit formation in certain regions of cement particles cause non-uniformly distributed reactions on the surface of cement grains [3, 27, 37, 45, 75, 176]. This may be attributed to the different reactivity sites on the surface of the particle as well as possible differences in stress state on the surface of particles since they do not have a regular shape.

These differences between dissolution rates are expected to increase the ions in solution and then the amount and nature of the hydration products. These differences would be expected to alter the physical properties of the paste and there the measured mechanical properties such as the

modulus and creep strain. There are a limited number of publications that suggest this. In a previous work based on micro-indentation and vertical scanning interferometry experiments, and molecular dynamics simulations, it is proposed that concrete creep is originated from dissolution-precipitation mechanism [177]. Another work suggested that load-induced hydration affects the early age short-term creep of hardening cement paste by measuring the degree of hydration and creep of loaded samples [138].

The accelerated stress induced dissolution of cement particles could be responsible for a portion of the creep measured in the highly-loaded samples. This is shown to occur in areas of higher stress near the load platen. These results can be seen in Figures 4-6 and 4-7. This could be caused by the anhydrous OPC forming hydration products that occupy a smaller space than the original reactants [83, 84, 91, 115].

While there is still missing information about the structure and chemistry of the hydration products that form during this period, it is likely that these materials have different properties than products formed under non-stressed conditions. In fact, previous publications have suggested that hydration products may be less likely to form in areas of high stress. In addition, there could be other influential phenomena like sliding of the paste phases over each other, and increased levels of compaction for samples under stress that are not able to be observed at this length scale. More insights may be able to be gained by investigating these changes at the nanoscale. Several publications have started to make measurements of coupled chemistry and structure at this length scale [19, 27, 62, 94, 108]. These are the subjects of future research.

Regardless of the shortcomings of these measurements, they provide an important introduction to new measurement methods that can be used to provide new insights into these problems and serve as the basis for numerical modeling that can combine many different phenomena together.

4-5-Conclusions

This study uses direct measurements by XCT over the first 60 h of hydration and provides insights into microstructural changes of anhydrous cement particles and high X-ray absorption hydration products as well as the stiffness and creep strain of these materials while under this early loading. The following conclusions are drawn from the findings:

- The Young's modulus of elasticity of the samples loaded to 50% of f_{1day} was between 1.4x and 1.6x greater than the samples only loaded to 12% of f_{1day} after 60 h of hydration.
- The creep strain of the samples loaded to 50% of f_{1day} were 8x greater than the samples loaded to 12% of f_{1day} at 48 h and the non-loaded sample did not deform.
- The sample loaded constantly at 12% of f_{1day} showed a decreased strain rate from 58.4 με/h over 30 h to 36 h, 29.4 με/h over 36 h to 48 h, and then 22.8 με/h over 48 h to 60 h. This stiffness gain over time is likely due to microstructure refinement from hydration.
- For the samples loaded to 50% of f_{1day}, the high-absorption material between the load platen and between 100 μm and 400 μm into the sample showed a decrease in high-absorption material compared to the regions further away from the platen and for the high-absorption material found in the samples under lower stress levels.
- Non uniform dissolution and formation of high absorption material was observed over 60 h of hydration.

The localized decrease in volume of the high-absorption material is likely due to higher stresses explained by Saint-Venant's Principle and the increased dissolution rate of strained crystals as explained by Riecke Principle. This means that there should be a relationship between the early age time-dependent deformation of paste under load and the dissolution of individual cement particles. However, more experiments are needed to more quantitatively couple these two

phenomena appropriately. Works are underway to complement the current work by studying the effect of stress application on the reactions of hydration products particularly calcium hydroxide crystals as one of the major products and also repeat these experiments at different length scales. These results will be presented in future publications.

CHAPTER V

CONCLUSION

This dissertation provides direct observations of the evolution of OPC and mC_3S paste over the first three days of hydration by using different X-ray imaging methods. The fCT was used to observe 3D changes of roughly 60,000 particles with industrially relevant w/s = 0.40 to 0.70 at 1 μm resolution during the first 16 h of hydration. Complementary nanoscale observations were made to measure the chemistry and structure of individual particles in dilute solutions. The same fCT data were used to study the evolution of air-filled voids within the first 16 h of hydration. The change in the total volume and size distribution of air-filled voids were investigated at a micron resolution. Finally, XCT was used for direct measurements over the first 60 h of hydration and provided insights into microstructural changes of anhydrous cement particles and high X-ray absorption hydration products as well as the stiffness and creep strain of the samples while under early age loading. The following conclusions are drawn from the findings:

5-1-Change in High-Absorption Materials:

- All experimental techniques suggest that the hydration product formed during the induction period had an average Ca/Si greater than 3.
- Micron scale measurements showed that the volume of the high X-ray absorption material increases during the induction period and seems to form on the surface of the

particles larger than 20 μm while the particles smaller than 20 μm show primarily dissolution. These same measurements show that as the acceleration period begins the X-ray absorption of the hydration product decreases.

- Nanoscale measurements during the induction period for 2 h of hydration in a saturated lime and gypsum solution found an average Ca/Si of 4.4 (±2.39) while the same measurements on particles after 10 h of hydration found an average Ca/Si of 2.31 (±0.21).

- Regions at 2 h of hydration also showed regions with Ca/Si > 10 which are likely CH. After 10 h of hydration these same areas were not observed. In the other hydration products both the Ca and S was observed to decrease by 6x between 2 h and 10 h while the Si concentration decreased by ≈ 30%.

- The nanoscale measurements show that the hydration products form locally on the surface of the reacting particles and these extended a few microns away from the particle surface.

- Both micron and nano scale measurements show non-uniform growth and dissolution were observed on each particle.

- The observations suggest that the formation and subsequent change in chemistry of these early age hydrates is important to the mechanisms of hydration.

- A mechanism is proposed that explains how the formation and dissipation of this material may be responsible for the induction and acceleration period in cement hydration.

5-2-Evolution of Air-Filled Voids:

For the samples made with *deionized water*:

- The total volume of the air-filled voids continuously increased during the induction period. During the same time period, the average distance between individual voids decreased. A considerable amount of voids < 100 μm^3 were observed to form uniformly, while the larger voids decreased in size.

- The total volume of the voids started to decrease over the first hours of the acceleration period and ultimately reached a constant value after approximately 4 h. In this time period the spatial and size distribution of air-filled voids becomes more uniform.

- All samples regardless of w/s and whether they were OPC or mC_3S showed similar volume change and void distribution at comparable times. However, the samples with a higher w/s had a higher portion of voids > 100 μm^3.

For the sample made with *de-aired water*:

- A significantly lower volume of air-filled voids is observed in these samples and these voids do not significantly change in size or spacing over time.

- The size distribution of the voids in this sample mainly consisted of voids > 100 μm^3 and over time these voids decreased in volume.

- This performance is drastically different than the samples made with the same materials and binder that contained deionized water. This highlights the importance of dissolved air on the mechanism for the void formation.

- A proposed mechanism based on the ionic strength is consistent with the trends observed.

5-3-Cement Paste samples under Stress:

- The Young's modulus of elasticity of the samples loaded to 50% of f_{1day} was between 1.4x and 1.6x greater than the samples only loaded to 12% of f_{1day} after 60 h of hydration.

- The creep strain of the samples loaded to 50% of f_{1day} were 8x greater than the samples loaded to 12% of f_{1day} at 48 h and the non-loaded sample did not deform.

- The sample loaded constantly at 12% of f_{1day} showed a decreased strain rate from 58.4 με/h over 30 h to 36 h, 29.4 με/h over 36 h to 48 h, and then 22.8 με/h over 48 h to 60 h. This stiffness gain over time is likely due to microstructure refinement from hydration.

- For the samples loaded to 50% of f_{1day}, the high-absorption material between the load platen and between 100 μm and 400 μm into the sample showed a decrease in high-absorption material compared to the regions further away from the platen and for the high-absorption material found in the samples under lower stress levels.

- Non-uniform dissolution and formation of high absorption material was observed over 60 h of hydration.

- It is proposed that the localized decrease in volume of the high-absorption material is likely due to higher stresses explained by Saint-Venant's Principle and the increased dissolution rate of strained crystals as explained by Riecke Principle.

5-4-Future works:

While the observations made in the dissertation give important and unprecedented insights into the mechanisms and kinetics of cement hydration, there is still missing information in this important area of ongoing research. The list of future works is as follows:

- Further experiments are needed to clarify the chemistry and nature of the changes that occur at the surface and in the surrounding fluid of cement particles during critical time periods. Particularly, an in-situ measurement of chemical composition changes would provide important insights.

- Additional work is needed to investigate how other variables such as chemical and mineral admixtures can affect the void formation.

- More experiments are needed to more quantitatively couple dissolution of cement particles and early age strain.

- The effect of stress application on the reactions of hydration products particularly calcium hydroxide crystals should be studied. This will require a greater contrast of the imaging methods.

- It would be important to repeat the loading experiments at different length scales to make a greater number of observations.

REFERENCES

[1] J.P. Mercier, G. Zambelli, W. Kurz, Introduction to materials science, Elsevier, Paris, 2012.

[2] J.W. Bullard, H.M. Jennings, R.A. Livingston, A. Nonat, G.W. Scherer, J.S. Schweitzer, K.L. Scrivener, J.J. Thomas, Mechanisms of cement hydration, Cement Concrete Res, 41 (2011) 1208-1223.

[3] P. Juilland, E. Gallucci, R. Flatt, K. Scrivener, Dissolution theory applied to the induction period in alite hydration, Cement Concrete Res, 40 (2010) 831-844.

[4] M. Parisatto, M.C. Dalconi, L. Valentini, G. Artioli, A. Rack, R. Tucoulou, G. Cruciani, G. Ferrari, Examining microstructural evolution of Portland cements by in-situ synchrotron micro-tomography, J Mater Sci, 50 (2015) 1805-1817.

[5] J.J. Thomas, J.J. Biernacki, J.W. Bullard, S. Bishnoi, J.S. Dolado, G.W. Scherer, A. Luttge, Modeling and simulation of cement hydration kinetics and microstructure development, Cement Concrete Res, 41 (2011) 1257-1278.

[6] D.H.C. Harris, C.G. Windsor, C.D. Lawrence, Free and Bound Water in Cement Pastes, Mag Concrete Res, 26 (1974) 65-72.

[7] B. Lothenbach, F. Winnefeld, C. Alder, E. Wieland, P. Lunk, Effect of temperature on the pore solution, microstructure and hydration products of Portland cement pastes, Cement Concrete Res, 37 (2007) 483-491.

[8] I. Pane, W. Hansen, Investigation of blended cement hydration by isothermal calorimetry and thermal analysis, Cement Concrete Res, 35 (2005) 1155-1164.

[9] X.Y. Pang, P. Boul, W.C. Jimenez, Isothermal calorimetry study of the effect of chloride accelerators on the hydration kinetics of oil well cement, Constr Build Mater, 77 (2015) 260-269.

[10] J. Stark, Recent advances in the field of cement hydration and microstructure analysis, Cement Concrete Res, 41 (2011) 666-678.

[11] J. Bensted, Some applications of conduction calorimetry to cement hydration, Adv. Cem. Res, 1 (1987) 35-44.

[12] M.D. Andersen, H.J. Jakobsen, J. Skibsted, Characterization of white Portland cement hydration and the C-S-H structure in the presence of sodium aluminate by Al-27 and Si-29 MAS NMR spectroscopy, Cement Concrete Res, 34 (2004) 857-868.

[13] E.T. Rodriguez, I.G. Richardson, L. Black, E. Boehm-Courjault, A. Nonat, J. Skibsted, Composition, silicate anion structure and morphology of calcium silicate hydrates (C-S-H) synthesised by silica-lime reaction and by controlled hydration of tricalcium silicate (C3S), Adv Appl Ceram, 114 (2015) 362-371.

[14] A. Bazzoni, M. Cantoni, K.L. Scrivener, Impact of Annealing on the Early Hydration of Tricalcium Silicate, J Am Ceram Soc, 97 (2014) 584-591.

[15] K.O. Kjellsen, H. Justnes, Revisiting the microstructure of hydrated tricalcium silicate - a comparison to Portland cement, Cement Concrete Comp, 26 (2004) 947-956.

[16] K.O. Kjellsen, B. Lagerblad, Microstructure of tricalcium silicate and Portland cement systems at middle periods of hydration-development of Hadley grains, Cement Concrete Res, 37 (2007) 13-20.

[17] D. Menetrier, I. Jawed, T.S. Sun, J. Skalny, Esca and Sem Studies on Early C3s Hydration, Cement Concrete Res, 9 (1979) 473-482.

[18] L. Wang, B. Yang, A. Abraham, L. Qi, X.Y. Zhao, Z.X. Chen, Construction of dynamic three-dimensional microstructure for the hydration of cement using 3D image registration, Pattern Anal Appl, 17 (2014) 655-665.

[19] Q. Hu, M. Aboustait, M.T. Ley, J.C. Hanan, V. Rose, R. Winarski, Combined three-dimensional structure and chemistry imaging with nanoscale resolution, Acta Mater, 77 (2014) 173-182.

[20] Q.N. Hu, M.T. Ley, J. Davis, J.C. Hanan, R. Frazier, Y.L. Zhang, 3D chemical segmentation of fly ash particles with X-ray computed tomography and electron probe microanalysis, Fuel, 116 (2014) 229-236.

[21] M.T. Ley , Q. Hu, M. Aboustait, T. Kim, M. Moradian, J. Hanan, V. Rose, R. Winarski, J. Gelb, Combining Nano X-ray Tomography and Nano X-ray Fluorescence to Create Time-dependent Three Dimensional Constitutive Maps, 2nd International Conference on Tomography of Materials and Structures,Quebec City, Canada, 2015.

[22] F. Fusseis, X. Xiao, C. Schrank, F. De Carlo, A brief guide to synchrotron radiation-based microtomography in (structural) geology and rock mechanics, J Struct Geol, 65 (2014) 1-16.

[23] A. Momose, T. Takeda, Y. Itai, K. Hirano, Phase-contrast X-ray computed tomography for observing biological soft tissues (vol 2, pg 473, 1996), Nat Med, 2 (1996) 596-596.

[24] P.M. Rao, J.T. Rhea, R.A. Novelline, A.A. Mostafavi, C.J. McCabe, Effect of computed tomography of the appendix on treatment of patients and use of hospital resources, New Engl J Med, 338 (1998) 141-146.

[25] W.C. Scarfe, A.G. Farman, P. Sukovic, Clinical applications of cone-beam computed tomography in dental practice, J Can Dent Assoc, 72 (2006) 75-80.

[26] E. Gallucci, K. Scrivener, A. Groso, M. Stampanoni, G. Margaritondo, 3D experimental investigation of the microstructure of cement pastes using synchrotron X-ray microtomography (mu CT), Cement Concrete Res, 37 (2007) 360-368.

[27] Q. Hu, M. Aboustait, T. Kim, M.T. Ley, J. Bullard, G. Scherer, J.C. Hanan, V. Rose, R. Winarski, J. Gelb, Direct measurements of 3d structure, chemistry and mass density during the induction period of C3s hydration, Cement Concrete Res, 89 (2016) 14-26.

[28] P. Trtik, A. Diaz, M. Guizar-Sicairos, A. Menzel, O. Bunk, Density mapping of hardened cement paste using ptychographic X-ray computed tomography, Cement Concrete Comp, 36 (2013) 71-77.

[29] J.J. Williams, Z. Flom, A.A. Amell, N. Chawla, X. Xiao, F. De Carlo, Damage evolution in SiC particle reinforced Al alloy matrix composites by X-ray synchrotron tomography, Acta Mater, 58 (2010) 6194-6205.

[30] X.D. Zhang, C.J. Xia, X.H. Xiao, Y.J. Wang, Fast synchrotron X-ray tomography study of the packing structures of rods with different aspect ratios, Chinese Phys B, 23 (2014).

[31] F. De Carlo, P.B. Albee, Y.S. Chu, D.C. Mancini, B. Tieman, S.Y. Wang, High-throughput real-time X-ray microtomography at the advanced photon source, International Symposium on Optical Science and Technology, International Society for Optics and Photonics, (2002) 1-13.

[32] F. De Carlo, B. Tieman, High-throughput X-ray microtomography system at the advanced photon source beamline 2-BM, In Optical Science and Technology, the SPIE 49th Annual Meeting, International Society for Optics and Photonics, (2004) 644-651.

[33] N.D. Parab, B. Claus, M.C. Hudspeth, J.T. Black, A. Mondal, J.Z. Sun, K. Fezzaa, X.H. Xiao, S.N. Luo, W.N. Chen, Experimental assessment of fracture of individual sand particles at different loading rates, Int J Impact Eng, 68 (2014) 8-14.

[34] J.G.M. Dejong, H.N. Stein, J.M. Stevels, Hydration of Tricalcium Silicate, J Appl Chem, 17 (1967) 246-250.

[35] H.M. Jennings, P.L. Pratt, Experimental Argument for the Existence of a Protective Membrane Surrounding Portland-Cement during the Induction Period, Cement Concrete Res, 9 (1979) 501-506.

[36] I. Odler, H. Dorr, Early Hydration of Tricalcium Silicate .2. Induction Period, Cement Concrete Res, 9 (1979) 277-284.

[37] K.L. Scrivener, P. Juilland, P.J.M. Monteiro, Advances in understanding hydration of Portland cement, Cement Concrete Res, 78 (2015) 38-56.

[38] H.N. Stein, J.M. Stevels, Influence of Silica on Hydration of 3cao,Sio2, J Appl Chem, 14 (1964) 338-+.

[39] M.E. Tadros, J. Skalny, R.S. Kalyoncu, Early Hydration of Tricalcium Silicate, J Am Ceram Soc, 59 (1976) 344-347.

[40] J.W. Bullard, G.W. Scherer, J.J. Thomas, Time dependent driving forces and the kinetics of tricalcium silicate hydration, Cement Concrete Res, 74 (2015) 26-34.

[41] P. Juilland, E. Gallucci, Morpho-topological the mechanisms and kinetic regimes of alite dissolution, Cement Concrete Res, 76 (2015) 180-191.

[42] F. Bellmann, T. Sowoidnich, H.M. Ludwig, D. Damidot, Dissolution rates during the early hydration of tricalcium silicate, Cement Concrete Res, 72 (2015) 108-116.

[43] L. Nicoleau, M.A. Bertolim, Analytical Model for the Alite (C3S) Dissolution Topography, J Am Ceram Soc, 99 (2016) 773-786.

[44] P.W. Brown, E. Franz, G. Frohnsdorff, H.F.W. Taylor, Analyses of the Aqueous Phase during Early C3s Hydration, Cement Concrete Res, 14 (1984) 257-262.

[45] K.L. Scrivener, A. Nonat, Hydration of cementitious materials, present and future, Cement Concrete Res, 41 (2011) 651-665.

[46] J.F. Young, H.S. Tong, R.L. Berger, Compositions of Solutions in Contact with Hydrating Tricalcium Silicate Pastes, J Am Ceram Soc, 60 (1977) 193-198.

[47] G.W. Groves, Portland-Cement Clinker Viewed by Transmission Electron-Microscopy, J Mater Sci, 16 (1981) 1063-1070.

[48] P.J.M. Monteiro, S.J. Bastacky, T.L. Hayes, Low-Temperature Scanning Electron-Microscope Analysis of the Portland-Cement Paste Early Hydration, Cement Concrete Res, 15 (1985) 687-693.

[49] D.M.F. Orr, Application of the Scanning Electron-Microscope to the Study of the Initial Hydration of Portland-Cement Paste, Cement Concrete Res, 13 (1983) 146-148.

[50] L. Zhang, G.W. Scherer, Comparison of methods for arresting hydration of cement, Cement Concrete Res, 41 (2011) 1024-1036.

[51] J.B. Ings, P.W. Brown, G. Frohnsdorff, Early Hydration of Large Single-Crystals of Tricalcium Silicate, Cement Concrete Res, 13 (1983) 843-848.

[52] J.W. Bullard, R.J. Flatt, New Insights Into the Effect of Calcium Hydroxide Precipitation on the Kinetics of Tricalcium Silicate Hydration, J Am Ceram Soc, 93 (2010) 1894-1903.

[53] S. Garrault, E. Finot, E. Lesniewska, A. Nonat, Study of C-S-H growth on C3S surface during its early hydration, Mater Struct, 38 (2005) 435-442.

[54] M.C.G. Juenger, P.J.M. Monteiro, E.M. Gartner, G.P. Denbeaux, Soft X-ray microscope investigation into the effects of calcium chloride on tricalcium silicate hydration, Cement Concrete Res, 35 (2005) 19-25.

[55] E.E. Bernardes, E.V.M. Carrasco, W.L. Vasconcelos, A.G. de Magalhaes, X-ray microtomography (mu-CT) to analyze the pore structure of a Portland cement composite based on the selection of different regions of interest, Constr Build Mater, 95 (2015) 703-709.

[56] T.J. Chotard, M.P. Boncoeur-Martel, A. Smith, J.P. Dupuy, C. Gault, Application of X-ray computed tomography to characterise the early hydration of calcium aluminate cement, Cement Concrete Comp, 25 (2003) 145-152.

[57] S. Fan, M. Li, X-ray computed microtomography of threedimensional microcracks and self-healing in engineered cementitious composites, Smart Mater Struct, 24 (2015).

[58] L. Gao, F.J. Ni, H.L. Luo, S. Charmot, Characterization of air voids in cold in-place recycling mixtures using X-ray computed tomography, Constr Build Mater, 84 (2015) 429-436.

[59] K.Y. Kim, T.S. Yun, K.P. Park, Evaluation of pore structures and cracking in cement paste exposed to elevated temperatures by X-ray computed tomography, Cement Concrete Res, 50 (2013) 34-40.

[60] J.R. Kyle, R.A. Ketcham, Application of high resolution X-ray computed tomography to mineral deposit origin, evaluation, and processing, Ore Geol Rev, 65 (2015) 821-839.

[61] T. Ponikiewski, J. Katzer, M. Bugdol, M. Rudzki, X-ray computed tomography harnessed to determine 3D spacing of steel fibres in self compacting concrete (SCC) slabs, Constr Build Mater, 74 (2015) 102-108.

[62] Q. Hu, M. Aboustait, T. Kim, M.T. Ley, J.C. Hanan, J.W. Bullard, R. Winarski, V. Rose, Direct three-dimensional observation of the microstructure and chemistry of C3S hydration, Cement Concrete Res, 88 (2016) 157-169.

[63] M. Holt, R. Harder, R. Winarski, V. Rose, Nanoscale Hard X-Ray Microscopy Methods for Materials Studies, Annu Rev Mater Res, 43 (2013) 183-211.

[64] J.W. Bullard, B. Lothenbach, P.E. Stutzman, K.A. Snyder, Coupling thermodynamics and digital image models to simulate hydration and microstructure development of portland cement pastes, J Mater Res, 26 (2011) 609-622.

[65] D.R.K. Brownrigg, The Weighted Median Filter, Commun Acm, 27 (1984) 807-818.

[66] I. Pitas, A.N. Venetsanopoulos, Nonlinear digital filters : principles and applications, Kluwer Academic Publishers, Boston, 1990.

[67] D. Damidot, A. Nonat, P. Barret, Kinetics of Tricalcium Silicate Hydration in Diluted Suspensions by Microcalorimetric Measurements, J Am Ceram Soc, 73 (1990) 3319-3322.

[68] J.H. Hubbell, Photon Mass Attenuation and Energy-Absorption Coefficients from 1 Kev to 20 Mev, Int J Appl Radiat Is, 33 (1982) 1269-1290.

[69] N. Otsu, A threshold selection method from gray-level histograms, Automatica, 11 (1975) 23-27.

[70] R.P. Winarski, M.V. Holt, V. Rose, P. Fuesz, D. Carbaugh, C. Benson, D.M. Shu, D. Kline, G.B. Stephenson, I. McNulty, J. Maser, A hard X-ray nanoprobe beamline for nanoscale microscopy, J Synchrotron Radiat, 19 (2012) 1056-1060.

[71] S. Vogt, MAPS: A set of software tools for analysis and visualization of 3D X-ray fluorescence data sets, J Phys Iv, 104 (2003) 635-638.

[72] D.G. Altman, J.M. Bland, Statistics notes - Standard deviations and standard errors, Brit Med J, 331 (2005) 903-903.

[73] S. Garrault, T. Behr, A. Nonat, Formation of the C-S-H layer during early hydration of tricalcium silicate grains with different sizes, J Phys Chem B, 110 (2006) 270-275.

[74] J.N. Maycock, J. Skalny, R. Kalyoncu, Crystal defects and hydration I. Influence of lattice defects, Cement Concrete Res, 4 (1974) 835–847.

[75] L. Nicoleau, A. Nonat, D. Perrey, The di- and tricalcium silicate dissolutions, Cement Concrete Res, 47 (2013) 14-30.

[76] I. Odler, J. Schuppstuhl, Early Hydration of Tricalcium Silicate .3. Control of the Induction Period, Cement Concrete Res, 11 (1981) 765-774.

[77] T. Sakurai, T. Sato, A. Yoshinaga, The effect of minor components on the early hydraulic activity of the major phases of Portland cement clinker, 5th ISCC, (1969) 300-321.

[78] A. Nonat, The structure and stoichiometry of C-S-H, Cement Concrete Res, 34 (2004) 1521-1528.

[79] A. Navrotsky, Nanoscale Effects on Thermodynamics and Phase Equilibria in Oxide Systems, Chemphyschem, 12 (2011) 2207-2215.

[80] A.B. Abell, K.L. Willis, D.A. Lange, Mercury intrusion porosimetry and image analysis of cement-based materials, J Colloid Interf Sci, 211 (1999) 39-44.

[81] I.G. Richardson, The nature of C-S-H in hardened cements, Cement Concrete Res, 29 (1999) 1131-1147.

[82] T.C. Powers, Structure and Physical Properties of Hardened Portland Cement Paste, J Am Ceram Soc, 41 (1958) 1-6.

[83] P.K. Mehta, P.J.M. Monteiro, Concrete : microstructure, properties, and materials, 3rd ed., McGraw-Hill, New York, 2006.

[84] S. Mindess, J.F. Young, D. Darwin, Concrete, 2nd ed., Prentice Hall, Upper Saddle River, NJ, 2003.

[85] J.J. Beaudoin, Handbook of analytical techniques in concrete science and technology, Noyes Publications ;, Park Ridge, NJ.

[86] S. Diamond, Mercury porosimetry - An inappropriate method for the measurement of pore size distributions in cement-based materials, Cement Concrete Res, 30 (2000) 1517-1525.

[87] I. Tekin, R. Birgul, H.Y. Aruntas, Determination of the effect of volcanic pumice replacement on macro void development for blended cement mortars by computerized tomography, Constr Build Mater, 35 (2012) 15-22.

[88] N. Narayanan, K. Ramamurthy, Structure and properties of aerated concrete: a review, Cement Concrete Comp, 22 (2000) 321-329.

[89] K.K. Aligizaki, Aligizaki, Kalliopi K. Pore structure of cement-based materials: testing, interpretation and requirements, CRC Press2005.

[90] S.W. Tang, X.H. Cai, Z. He, W. Zhou, H.Y. Shao, Z.J. Li, T. Wu, E. Chen, The review of pore structure evaluation in cementitious materials by electrical methods, Constr Build Mater, 117 (2016) 273-284.

[91] P. Lura, J. Couch, O.M. Jensen, J. Weiss, Early-age acoustic emission measurements in hydrating cement paste: Evidence for cavitation during solidification due to self-desiccation, Cement Concrete Res, 39 (2009) 861-867.

[92] N. Bossa, P. Chaurand, J. Vicente, D. Borschneck, C. Levard, O. Aguerre-Chariol, J. Rose, Micro- and nano-X-ray computed-tomography: A step forward in the characterization of the pore network of a leached cement paste, Cement Concrete Res, 67 (2015) 138-147.

[93] N. Burlion, D. Bernard, D. Chen, X-ray microtomography: Application to microstructure analysis of a cementitious material during leaching process, Cement Concrete Res, 36 (2006) 346-357.

[94] M. Moradian, Q. Hu, M. Aboustait, M.T. Ley, J.C. Hanan, X. Xiao, V. Rose, R. Winarski, Multi-scale In-Situ Observations of Structure and Chemistry Changes of Portland Cement Systems During Hydration, (Submitted).

[95] R.C.K. Wong, K.T. Chau, Estimation of air void and aggregate spatial distributions in concrete under uniaxial compression using computer tomography scanning, Cement Concrete Res, 35 (2005) 1566-1576.

[96] D.P. Bentz, S. Mizell, S. Satterfield, J. Devaney, W. George, P. Ketcham, J. Graham, J. Porterfield, D. Quenard, F. Vallee, H. Sallee, E. Boller, J. Baruchel, The Visible Cement Data Set, J Res Natl Inst Stan, 107 (2002) 137-148.

[97] D.P. Bentz, D.A. Quenard, H.M. Kunzel, J. Baruchel, F. Peyrin, N.S. Martys, E.J. Garboczi, Microstructure and transport properties of porous building materials. II: Three-dimensional X-ray tomographic studies, Mater Struct, 33 (2000) 147-153.

[98] D. Gastaldi, F. Canonico, L. Capelli, E. Boccaleri, M. Milanesio, L. Palin, G. Croce, F. Marone, K. Mader, M. Stampanoni, In situ tomographic investigation on the early hydration behaviors of cementing systems, Constr Build Mater, 29 (2012) 284-290.

[99] L. Helfen, E. Dehn, P. Mikulik, T. Baumbach, Three-dimensional imaging of cement microstructure evolution during hydration, Adv Cem Res, 17 (2005) 103-111.

[100] K.Y. Kim, T.S. Yun, J. Choo, D.H. Kang, H.S. Shin, Determination of air-void parameters of hardened cement-based materials using X-ray computed tomography, Constr Build Mater, 37 (2012) 93-101.

[101] M.A.B. Promentilla, T. Sugiyama, T. Hitomi, N. Takeda, Quantification of tortuosity in hardened cement pastes using synchrotron-based X-ray computed microtomography, Cement Concrete Res, 39 (2009) 548-557.

[102] Z.Q. Wu, J.F. Young, Formation of Calcium Hydroxide from Aqueous Suspensions of Tricalcium Silicate, J Am Ceram Soc, 67 (1984) 48-51.

[103] J.J. Chen, J.J. Thomas, H.F.W. Taylor, H.M. Jennings, Solubility and structure of calcium silicate hydrate, Cement Concrete Res, 34 (2004) 1499-1519.

[104] F. Chalencon, L. Orgeas, P.J.J. Dumont, G. Foray, J.Y. Cavaille, E. Maire, S.R. du Roscoat, Lubricated compression and X-ray microtomography to analyse the rheology of a fibre-reinforced mortar, Rheol Acta, 49 (2010) 221-235.

[105] K.V. Subramaniam, X.J. Wang, An investigation of microstructure evolution in cement paste through setting using ultrasonic and rheological measurements, Cement Concrete Res, 40 (2010) 33-44.

[106] J. Pourchez, B. Ruot, J. Debayle, E. Pourchez, P. Grosseau, Some aspects of cellulose ethers influence on water transport and porous structure of cement-based materials, Cement Concrete Res, 40 (2010) 242-252.

[107] J. Adrien, S. Meille, S. Tadier, E. Maire, L. Sasaki, In-situ X-ray tomographic monitoring of gypsum plaster setting, Cement Concrete Res, 82 (2016) 107-116.

[108] W.A. Gerth, Effects of Dissolved Electrolytes on the Solubility and Partial Molar Volume of Helium in Water from 50 to 400 Atmospheres at 25-Degrees-C, J Solution Chem, 12 (1983) 655-669.

[109] J. Zhang, E.A. Weissinger, S. Peethamparan, G.W. Scherer, Early hydration and setting of oil well cement, Cement Concrete Res, 40 (2010) 1023-1033.

[110] S. Peethamparan, E. Weissinger, J. Vocaturo, J. Zhang, G. Scherer, Monitoring chemical shrinkage using pressure sensors, ACI Special Publication, 270 (2010) 77-88.

[111] T. Sun, Y. Neuvo, Detail-Preserving Median Based Filters in Image-Processing, Pattern Recogn Lett, 15 (1994) 341-347.

[112] Z. Wang, D. Zhang, Progressive switching median filter for the removal of impulse noise from highly corrupted images, Ieee T Circuits-Ii, 46 (1999) 78-80.

[113] F.R. Brushett, L. Trahey, X.H. Xiao, J.T. Vaughey, Full-Field Synchrotron Tomography of Nongraphitic Foam and Laminate Anodes for Lithium-Ion Batteries, Acs Appl Mater Inter, 6 (2014) 4524-4534.

[114] C.W. Chung, P. Suraneni, J.S. Popovics, L.J. Struble, W.J. Weiss, Application of ultrasonic P-wave reflection to measure development of early-age cement-paste properties, Mater Struct, 46 (2013) 987-997.

[115] E. Tazawa, S. Miyazawa, T. Kasai, Chemical Shrinkage and Autogenous Shrinkage of Hydrating Cement Paste, Cement Concrete Res, 25 (1995) 288-292.

[116] C.J.J. Fox, On the coefficients of absorption of nitrogen and oxygen in distilled water and seawater, and of atmospheric carbonic acid in sea-water., T Faraday Soc, 5 (1909) 0068-0086.

[117] M.N. Kutty, Site selection for aquaculture: Chemical features of water., food and agriculture organization (FAO), 1987.

[118] L.K. Wang, N.K. Shammas, W.A. Selke, D.B. Aulenbach, Gas dissolution, release, and bubble formation in flotation systems, Flotation Technology, Humana Press2010, pp. 49-83.

[119] G.C. Whipple, M.C. Whipple, Solubility of oxygen in sea water., J Am Chem Soc, 33 (1911) 362-365.

[120] R. Battino, T.R. Rettich, T. Tominaga, The Solubility of Oxygen and Ozone in Liquids, J Phys Chem Ref Data, 12 (1983) 163-178.

[121] S.E. Manahan, Water chemistry : green science and technology of nature's most renewable resource, CRC Press, Boca Raton, FL, 2011.

[122] M.M. Benjamin, Water chemistry, McGraw-Hill, Boston, 2002.

[123] J.C. Lee, D.L. Meyrick, Gas-Liquid Interfacial Areas in Salt Solutions in an Agitated Tank, Trans Inst Chem Eng, 48 (1970) T37-&.

[124] G. Marrucci, L. Nicodemo, Coalescence of Gas Bubbles in Aqueous Solutions of Inorganic Electrolytes, Chem Eng Sci, 22 (1967) 1257-&.

[125] Zieminsk.Sa, M.M. Caron, Blackmor.Rb, Behavior of Air Bubbles in Dilute Aqueous Solutions, Ind Eng Chem Fund, 6 (1967) 233-&.

[126] V.S.J. Craig, B.W. Ninham, R.M. Pashley, Effect of Electrolytes on Bubble Coalescence, Nature, 364 (1993) 317-319.

[127] P.K. Weissenborn, R.J. Pugh, Surface tension of aqueous solutions of electrolytes: Relationship with ion hydration, oxygen solubility, and bubble coalescence, J Colloid Interf Sci, 184 (1996) 550-563.

[128] V.S.J. Craig, B.W. Ninham, R.M. Pashley, Study of the long-range hydrophobic attraction in concentrated salt solutions and its implications for electrostatic models, Langmuir, 14 (1998) 3326-3332.

[129] C.L. Henry, C.N. Dalton, L. Scruton, V.S.J. Craig, Ion-specific coalescence of bubbles in mixed electrolyte solutions, J Phys Chem C, 111 (2007) 1015-1023.

[130] X.F. Pang, Water: molecular structure and properties, World Scientific2014.

[131] M. Firouzi, T. Howes, A.V. Nguyen, A quantitative review of the transition salt concentration for inhibiting bubble coalescence, Adv Colloid Interfac, 222 (2015) 305-318.

[132] L.K. Wang, Flotation technology, Humana, New York, 2010.

[133] A.C. Lasaga, A. Luttge, A model for crystal dissolution, Eur J Mineral, 15 (2003) 603-615.

[134] P.W. Voorhees, The Theory of Ostwald Ripening, J Stat Phys, 38 (1985) 231-252.

[135] V.S.J. Craig, Bubble coalescence and specific-ion effects, Curr Opin Colloid In, 9 (2004) 178-184.

[136] V.S.J. Craig, B.W. Ninham, R.M. Pashley, The Effect of Electrolytes on Bubble Coalescence in Water, J Phys Chem-Us, 97 (1993) 10192-10197.

[137] C.L. Henry, V.S.J. Craig, The Link between Ion Specific Bubble Coalescence and Hofmeister Effects Is the Partitioning of Ions within the Interface, Langmuir, 26 (2010) 6478-6483.

[138] B.T. Tamtsia, J.J. Beaudoin, J. Marchand, The early age short-term creep of hardening cement paste: load-induced hydration effects, Cement Concrete Comp, 26 (2004) 481-489.

[139] C. Galitz, Z. Grasley, Effects of strain reversal on elastic and viscoelastic properties of early age cement paste beams, Mater Struct, (2016) (in press).

[140] X. Li, Z.C. Grasley, J.W. Bullard, E.J. Garboczi, Computing the time evolution of the apparent viscoelastic/viscoplastic Poisson's ratio of hydrating cement paste, Cement Concrete Comp, 56 (2015) 121-133.

[141] X. Li, Z.C. Grasley, E.J. Garboczi, J.W. Bullard, Modeling the apparent and intrinsic viscoelastic relaxation of hydrating cement paste, Cement Concrete Comp, 55 (2015) 322-330.

[142] Q. Zhou, J.J. Beaudoin, Effect of applied hydrostatic stress on the hydration of Portland cement and C3S, Adv Cem Res, 15 (2003) 9-16.

[143] P.D. Bons, B. den Brok, Crystallographic preferred orientation development by dissolution-precipitation creep, J Struct Geol, 22 (2000) 1713-1722.

[144] D. Croize, F. Renard, K. Bjorlykke, D.K. Dysthe, Experimental calcite dissolution under stress: Evolution of grain contact microstructure during pressure solution creep, J Geophys Res-Sol Ea, 115 (2010).

[145] S. deMeer, C.J. Spiers, Uniaxial compaction creep of wet gypsum aggregates, J Geophys Res-Sol Ea, 102 (1997) 875-891.

[146] J.P. Gratier, Experimental Pressure Solution of Halite by an Indenter Technique, Geophys Res Lett, 20 (1993) 1647-1650.

[147] H.W. Green, Pressure Solution Creep - Some Causes and Mechanisms, J Geophys Res, 89 (1984) 4313-4318.

[148] Y. Le Guen, F. Renard, R. Hellmann, E. Brosse, M. Collombet, D. Tisserand, J.P. Gratier, Enhanced deformation of limestone and sandstone in the presence of high P-co2 fluids, J Geophys Res-Sol Ea, 112 (2007).

[149] E.A. Pachon-Rodriguez, E. Guillon, G. Houvenaghel, J. Colombani, Pressure solution as origin of the humid creep of a mineral material, Phys Rev E, 84 (2011).

[150] F. Renard, E. Gundersen, R. Hellmann, M. Collombet, Y. Le Guen, Numerical modeling of the effect of carbon dioxide sequestration on the rate of pressure solution creep in limestone: Preliminary results, Oil Gas Sci Technol, 60 (2005) 381-399.

[151] F. Renard, D. Bernard, X. Thibault, E. Boller, Synchrotron 3D microtomography of halite aggregates during experimental pressure solution creep and evolution of the permeability, Geophys Res Lett, 31 (2004).

[152] J.F. Hippertt, Microstructures and C-Axis Fabrics Indicative of Quartz Dissolution in Sheared Quartzites and Phyllonites, Tectonophysics, 229 (1994) 141-163.

[153] A. Stallard, D. Shelley, Quartz C-Axes Parallel to Stretching Directions in Very Low-Grade Metamorphic Rocks, Tectonophysics, 249 (1995) 31-40.

[154] J. Morel, Experimental investigation into the effect of stress on dissolution and growth of very soluble brittle salts in aqueous solution, Johannes Gutenberg-Universit/it, 2000.

[155] B. Bresson, F. Meducin, H. Zanni, C. Noik, Hydration of tricalcium silicate (C3S) at high temperature and high pressure, J Mater Sci, 37 (2002) 5355-5365.

[156] A.C. Jupe, A.P. Wilkinson, G.P. Funkhouser, Oil-Well Cement and C3S Hydration Under High Pressure as Seen by In Situ X-Ray Diffraction, Temperatures <= 80 degrees C with No Additives, J Am Ceram Soc, 94 (2011) 1591-1597.

[157] G.W. Scherer, G.P. Funkhouser, S. Peethamparan, Effect of pressure on early hydration of class H and white cement, Cement Concrete Res, 40 (2010) 845-850.

[158] Z.C. Grasley, C.A. Jones, X. Li, E.J. Garboczi, J.W. Bullard, Elastic and viscoelastic properties of calcium silicate hydrate, 4th International Symposium on Nanotechnology in ConstructionCrete, Greece, 2012.

[159] Z.C. Grasley, K.R. Rajagopal, X. Li, Theoretical basis for apparent viscoelastic and viscoplastic behavior of cementitious materials, International US-Poland Workshop on Multiscale Computational Modeling of Cementitious MaterialsCracow, Poland, 2012.

[160] C.P. Aichele, D. Venkataramani, J.E. Smay, M.H. McCann, S. Richter, M. Khanzadeh-Moradllo, M. Aboustait, M.T. Ley, A comparison of automated scanning electron microscopy (ASEM) and acoustic attenuation spectroscopy (AAS) instruments for particle sizing, Colloid Surface A, 479 (2015) 46-51.

[161] B.R. Frieden, New Restoring Algorithm for Preferential Enhancement of Edge Gradients, J Opt Soc Am, 66 (1976) 280-283.

[162] T.S. Huang, G.J. Yang, G.Y. Tang, Fast 2-Dimensional Median Filtering Algorithm, Ieee T Acoust Speech, 27 (1979) 13-18.

[163] R.C. Gonzalez, R.E. Woods, Digital image processing, 3rd ed., Prentice Hall, Upper Saddle River, N.J., 2008.

[164] R.C. Gonzalez, R.E. Woods, S.L. Eddins, Digital Image processing using MATLAB, 2nd ed., Gatesmark Pub., S.I., 2009.

[165] T. Kurita, N. Otsu, N. Abdelmalek, Maximum-Likelihood Thresholding Based on Population Mixture-Models, Pattern Recogn, 25 (1992) 1231-1240.

[166] O.D. Trier, A.K. Jain, Goal-Directed Evaluation of Binarization Methods, Ieee T Pattern Anal, 17 (1995) 1191-1201.

[167] M.Z. Zhang, Y.J. He, G. Ye, D.A. Lange, K. van Breugel, Computational investigation on mass diffusivity in Portland cement paste based on X-ray computed microtomography (mu CT) image, Constr Build Mater, 27 (2012) 472-481.

[168] W.D. Callister, Materials science and engineering : an introduction, 7th ed., John Wiley & Sons, New York, 2007.

[169] K. Velez, S. Maximilien, D. Damidot, G. Fantozzi, F. Sorrentino, Determination by nanoindentation of elastic modulus and hardness of pure constituents of Portland cement clinker, Cement Concrete Res, 31 (2001) 555-561.

[170] R.C. Batra, J.S. Yang, Saint-Venants Principle in Linear Piezoelectricity, J Elasticity, 38 (1995) 209-218.

[171] H. Zhu, F. Pierron, Exploration of Saint-Venant's Principle in Inertial High Strain Rate Testing of Materials, Exp Mech, 56 (2016) 3-23.

[172] J.N. Goodier, A general proof of Saint-Venant's principle., Philos Mag, 23 (1937) 607-609.

[173] R.J. Knops, P. Villaggio, On Saint-Venant's Principle for Elasto-Plastic Bodies, Math Mech Solids, 14 (2009) 601-621.

[174] B. Lautrup, Physics of continuous matter : exotic and everyday phenomena in the macroscopic world, 2nd ed., Taylor & Francis, Boca Raton, 2011.

[175] C.W. Correns, Growth and Dissolution of Crystals under Linear Pressure, Discuss Faraday Soc, (1949) 267-271.

[176] A. Kumar, S. Bishnoi, K.L. Scrivener, Modelling early age hydration kinetics of alite, Cement Concrete Res, 42 (2012) 903-918.

[177] I. Pignatelli, A. Kumar, R. Alizadeh, Y. Le Pape, M. Bauchy, G. Sant, A dissolution-precipitation mechanism is at the origin of concrete creep in moist environments, J Chem Phys, 145 (2016).

APPENDICES

Appendix-A

Automated Scanning Electron Microscope (ASEM)

The particle size distribution (PSD) and chemical makeup of OPC and mC_3S powders were examined by automated scanning electron microscopy (ASEM). An FEI-ASPEX PSEM Explorer instrument with an SDD EDS detector and a tungsten filament was utilized for this purpose. The powder was first dispersed using a 1:1 mix of acetone and isopropyl alcohol. A drop of the mixture was placed on a carbon tape covering the aluminum stub and then dried at room temperature.

The stub was then placed in the instrument where the contrast between the backscattered data and the substrate is used to find and analyze the particles. A computer algorithm finds the individual particles automatically over the course of scanning. Also, energy dispersive spectroscopy (EDS) is utilized to characterize the chemical makeup of the powder. Therefore, the instrument and algorithm are able to provide information about the number of particles, diameter, shape factor, and chemical composition of the examined powder. The necessary time for conducting the test is roughly five seconds per particle. Figure A1 demonstrates a schematic representation of the ASEM experiment. More information about ASEM can be found elsewhere [1A, 2A].

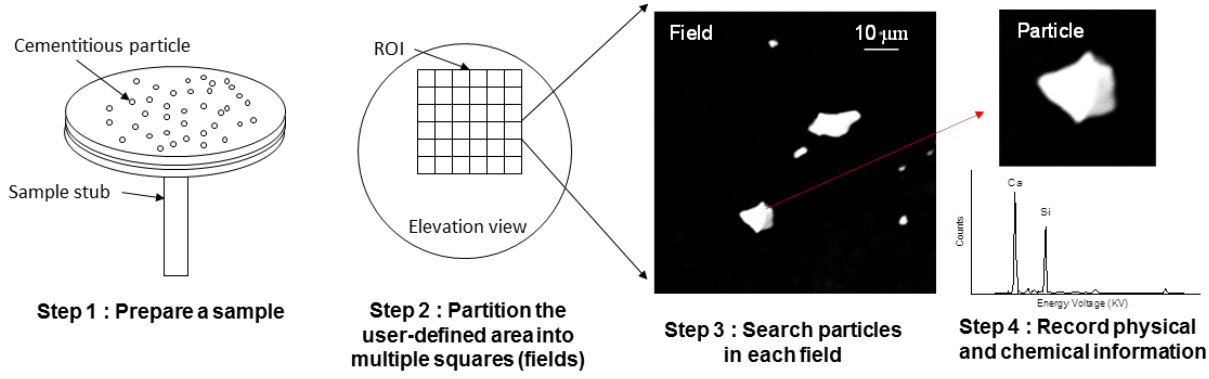

Fig. A1. A schematic representation of ASEM method.

Figure A2 also demonstrates particle size distributions of OPC and mC_3S powders obtained from the ASEM technique. According to the figure, OPC powder is slightly finer than mC_3S.

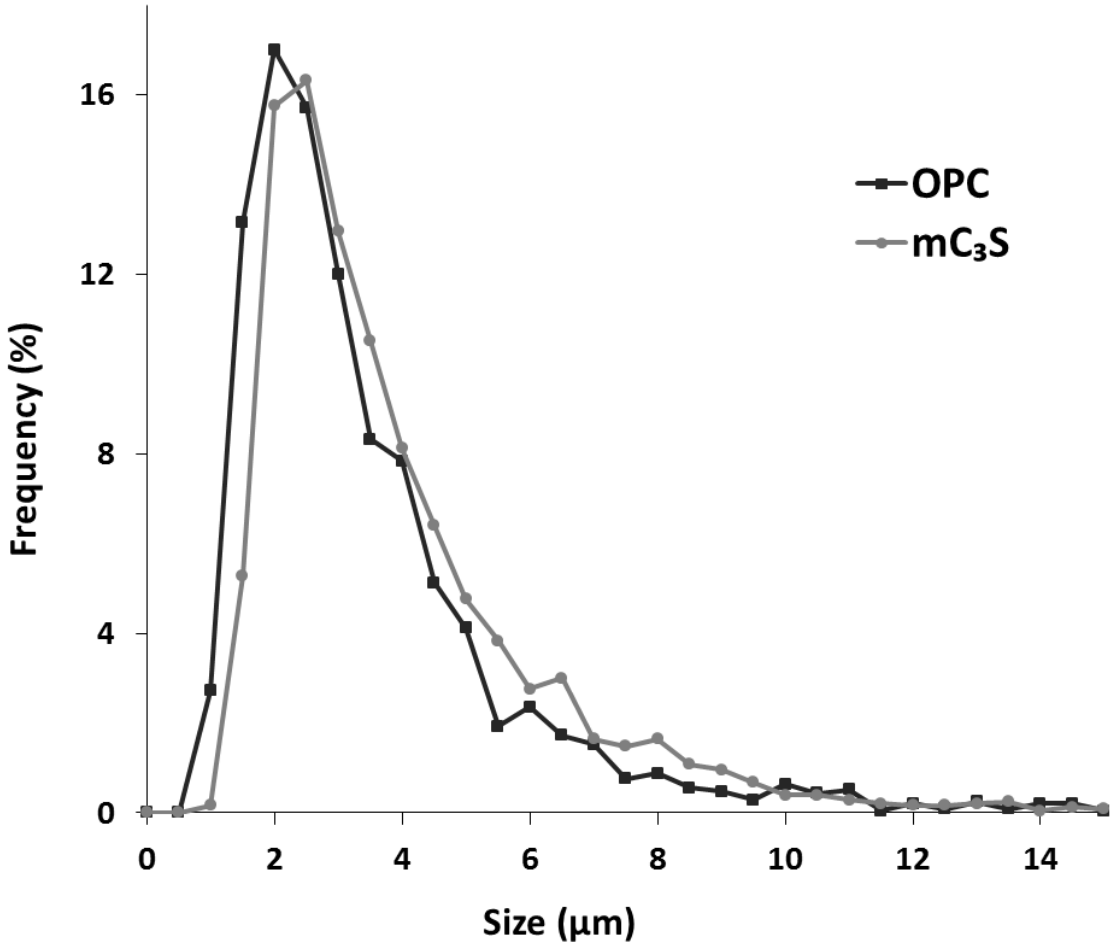

Fig. A2. Particle size distribution of OPC and mC_3S by ASEM.

Mixing and Sample Preparation for fCT

Water was added to the cementitious powder, and the mixture was stirred 10 times clockwise and 10 times counterclockwise in a vial by a stainless steel rod. Then the vial was placed in a Vortex Mixer produced by Stuart (Staffordshire, UK) and mixed with a speed of 1000 rpm for 3 minutes.

After mixing, a 1.5 mm diameter polyethylene tube was inserted into the paste. The end of the tube was covered with a finger and the tube was removed. The vacuum created in the sealed tube held the paste within the tube as it was removed. The bottom and top of the tube were then sealed with clay to minimize loss of moisture. The sample was compacted by holding the sealed tube in one hand and clapping it into another hand ten times.

Reconstruction and Segmentation of high-absorption materials in fCT Data

The 2-D projections were reconstructed in 3-D using a Fast Fourier Transforms (FFT) based algorithm (Gridrec Algorithm) to produce the necessary data for image processing. More details about the Gridrec Algorithm can be found in other publications [3A-5A].

A median filter with a radius of 2.5 μm was applied to all images to reduce noise. Median filtering is a nonlinear process that smooths the image by reducing noise.

Tomographs were collected from cement and mC_3S powder to determine a single gray value to determine the gray value for the high-absorption material segmentation. By having bulk and absolute densities of the powders the theoretical volume of cement in the powder sample can be determined. To measure the bulk density, the powder was placed and compacted in a container with the same specifications as other fCT samples. Based on the measured weight and the known volume of the container the bulk density was calculated. A gray value was chosen so that the calculated cement volume from the tomograph equals the theoretical value. The theoretical value was calculated by dividing bulk density (1.24 g/cm^3) by absolute density (3.15 g/cm^3 for OPC). Therefore, a threshold gray value was found for the powder so that 39.4% ($\frac{1.24}{3.15} \times 100 = 39.4$) of the volume of the container is cement grains and the rest is void. This threshold value was applied to all collected tomographs to segment the high-absorption materials from the rest of the paste. Since the density of mC_3S and OPC is close to each other, the same calculation was performed for mC_3S. After segmentation, some single voxel regions were removed as they are likely noise.

Isothermal Calorimetry Test

The procedure for making the paste for this test was the same as for fast tomography samples. The vials were capped and placed in a Tam Air Isothermal Calorimeter at a constant temperature of 25 °C, and the hydration rate was monitored for 24 hours. The heat capacities of cementitious powders and water were assumed to be 0.753 $Jg^{-1}K^{-1}$ and 4.1814 $Jg^{-1}K^{-1}$, respectively.

Mass Attenuation Coefficient of Hydration Products

The mass attenuation coefficient of a mixture of C-S-H and CH with different Ca/Si and H/S is calculated by tool available from NIST [6A] and the results are shown in Figure A3. The mass attenuation coefficient of C_3S is also shown by a horizontal dashed line. The source energy used in calculations matches the condition of fCT and is 30 keV. The H/S was assumed to be between 1.2 and 4 corresponding to dry and saturated conditions of C-S-H, respectively [7A].

The mass attenuation coefficient is correlated to the transmitted X-ray intensity as mentioned in the main manuscript [8A] and therefore these calculations can be helpful to obtain a rough idea about chemical change in fCT dataset. The nTACCo data showed that Ca/Si of the hydration

products at 2 h corresponding to the induction period is >4.4±2.39 and according to the graph, they are identified as high-absorption material because of the similar absorption to anhydrous C_3S. After 10 h of hydration and during the acceleration period, Ca/Si is reduced to 2.31±0.21 and so X-ray absorption is lower than anhydrous C_3S and the mixture is identified as low-absorption material. This can explain the increase and then decrease in volume of high-absorption materials as observed by the fCT and TXM data. Furthermore, this analysis does not take into account the presence of CS in the material. This would also be expected to increase the mass attenuation coefficient of the material.

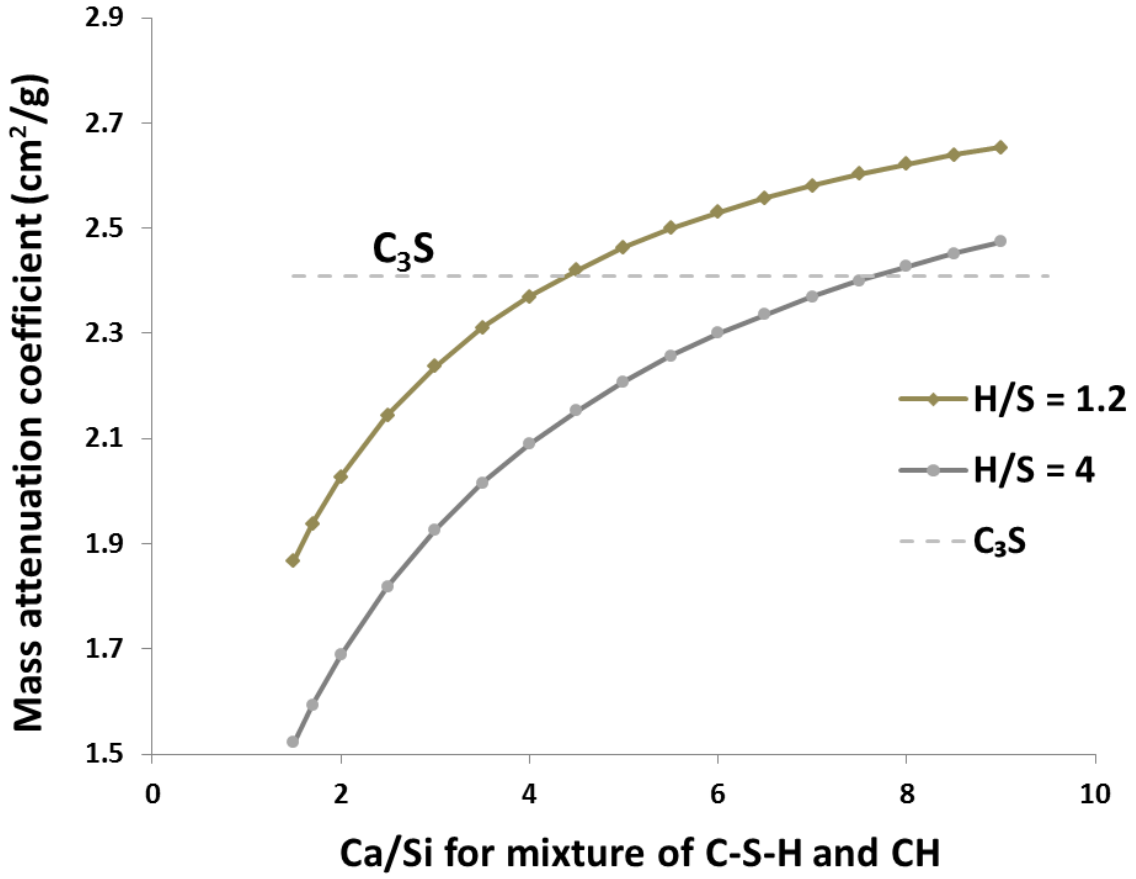

Fig. A3. Mass attenuation coefficient of C-S-H with different Ca/Si calculated from [6A]. The coefficient for C_3S is also shown by horizontal dashed line for comparison.

References

[1A] M. Aboustait, Q. Hu, R. Frazier, Y. Zhang, B. Tabb, T. Ley, J. Hanan, Innovative prediction of fly ash performance in concrete, Oklahoma Transportation Center Report, 2013.

[2A] C.P. Aichele, D. Venkataramani, J.E. Smay, M.H. McCann, S. Richter, M. Khanzadeh-Moradllo, M. Aboustait, T. Ley, A Comparison of Automated Scanning Electron Microscopy

(ASEM) and Acoustic Attenuation Spectroscopy (AAS) Instruments for Particle Sizing, Colloids Surface. A. 479 (2015) 46-51.

[3A] F. Marone, M. Stampanoni, Regridding reconstruction algorithm for real-time tomographic imaging, J. Synchrotron Radiat. 19 (2012) 1029–1037.

[4A] B.A. Dowd, G.H. Campbell, R.B. Marr, V. Nagarkar, S. Tipnis, L. Axe, D.P. Siddons, Developments in synchrotron x-ray computed microtomography at the national synchrotron light source, SPIE's International Symposium on Optical Science, Engineering, and Instrumentation, (1999) 224–236.

[5A] M.L. Rivers, tomoRecon: high-speed tomography reconstruction on workstations using multi-threading, SPIE Optical Engineering+ Applications, 2012.

[6A] National Institute of Standard and Technology (NIST). X-ray form factor, attenuation, and scattering tables. Available from: http://physics.nist.gov/PhysRefData/FFast/html/form.html.

[7A] J.F. Young, W. Hansen, Volume relationships for CSH formation based on hydration stoichiometries, In MRS proceedings 85 (1986) 313-322.

[8A] J.H. Hubbell, Photon Mass Attenuation and Energy-Absorption Coefficients from 1 Kev to 20 Mev, Int J Appl Radiat Is, 33 (1982) 1269-1290.

Appendix-B

Reconstruction and Segmentation of air-filled void in Fast tomography Data

The acquired radiographs were reconstructed to produce 2D slices using Gridrec Algorithm that is a Fast Fourier Transforms (FFT) based algorithm [1B, 2B]. More information on the Gridrec Algorithm can be found in the literature [3-5B].

The resulting images need some initial pre-processing to be used for analysis. A median 2.5×2.5×2.5 voxels filter was applied to all reconstructed slices to reduce the noise and artifacts in images before implementing image segmentation. This filter is popular for image processing because of its simplicity and capability of preserving image edges [6-8B]. This process consists of finding the median of a number of pixels in the neighborhood of a pixel and putting the calculated median value as the new value for that pixel [9B]. The number of neighbors depends on the size of the filter.

The air-filled voids were separated from the rest of the paste by applying a single threshold value to the histogram of the tomographic datasets. The threshold value was decided based on the measurements from at least 30 individual voids that were isolated by an operator within each tomograph dataset. The average gray value of air-filled voids was calculated based on the implemented measurements. Figure B1 shows a histogram of average gray value of voids in OPC w/s = 0.60. A normal distribution is fitted to the data. According to normal distribution definition, about 99.7% of the voids are within 3×standard deviation from mean. Since voids are the darkest phase in the tomographs, the lower gray value threshold is 0. So the calculated values were slightly rounded to include 0 in the segmentation range.

Figure B2 shows the gray value histogram from entire ROI for OPC with w/s = 0.60. The location of calculated threshold value can also be found in the graph.

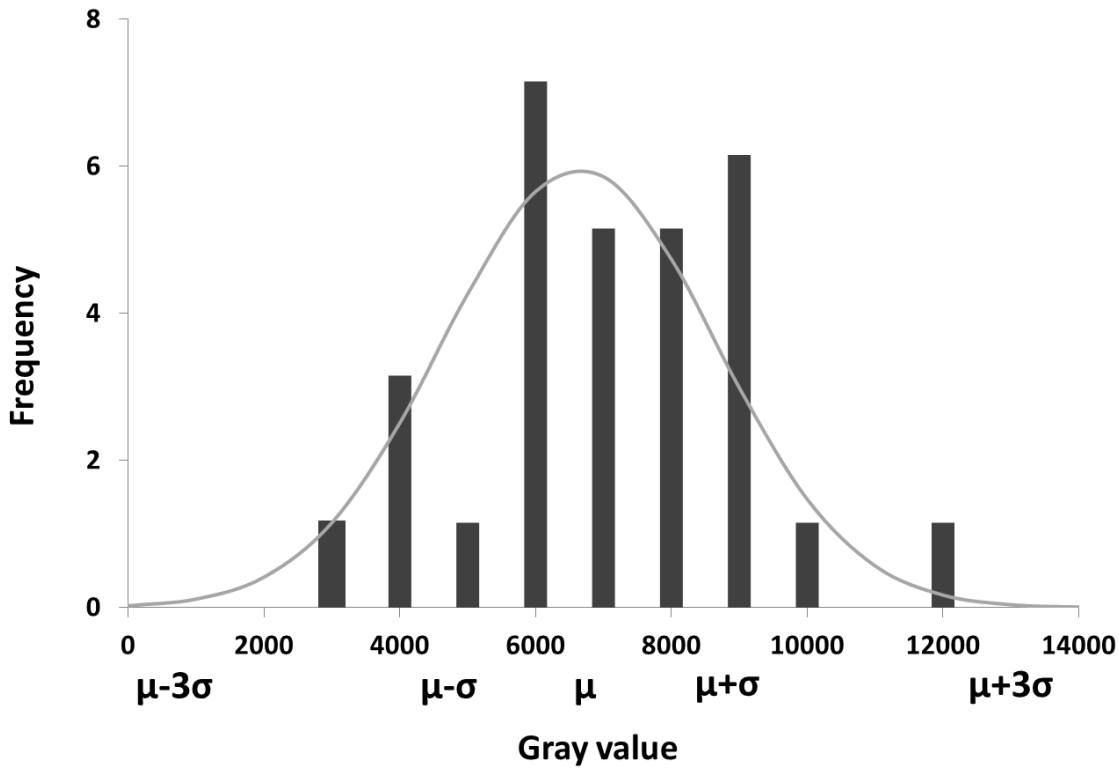

Fig. B1. Distribution of average gray value of voids in OPC w/s = 0.60.

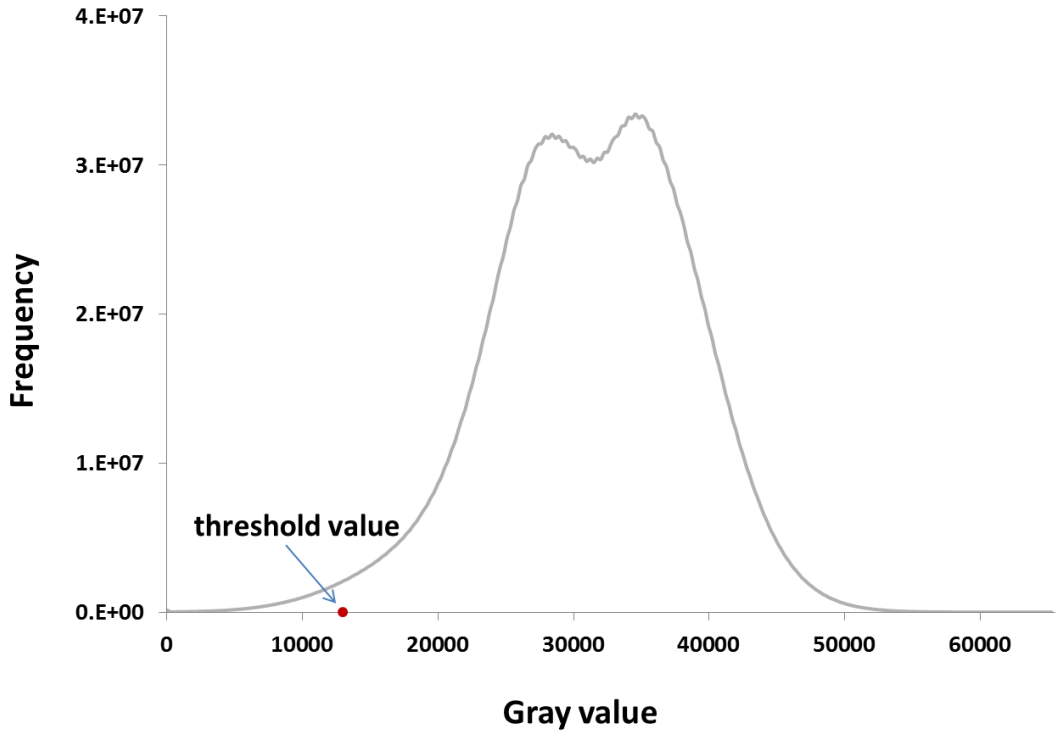

Fig. B2. Histogram of entire ROI in all time periods for OPC w/s = 0.60. The segmenting value is shown by a red dot.

Estimation of dissolved air in the mixture

A typical calculation for w/s=0.60 and dissolved air M_{air}=30 mg/l is presented in this section. The assumed densities are: air ≈1.20 kg/m^3, water ≈1000 kg/m^3, cement 3150 kg/m^3 [10,11B].

For 1 liter of water and w/s=0.6:

$$\text{Ms} = \frac{1}{0.6} = 1.67\ kg$$

where M_s is mass of solid.

Total volume of paste V_t is calculated by: $V_t=V_w+V_s$

where V_w is the volume of water, and V_s is the volume of solid. Vs can be calculated by dividing mass to the density:

$$V_s = \frac{M_s}{\rho_s} = \frac{1.67}{3.15} = 0.52 \text{ liter}$$

where ρ_s=3.15 gr/cm^3 is density of the solid.

So the total volume of a paste with 1 liter of water and w/s=0.60 would be:

$V_t=V_w+V_s=1+0.52=1.52$ liter

The volume of dissolve air in the mixing water in gas state V_{air} is:

$$V_{air}=\frac{M_{air}}{\rho_{air}}=\frac{30}{1.2}\times 10^{-3}=0.025 \text{ liter}$$

where $\rho_{air}=1.2$ kg/m^3 is density of air. So the percentage of air stemmed from the mixing water in the paste can be easily calculated by:

$$\%\text{ of air in paste}=\frac{V_{air}}{V_t}=\frac{0.025}{1.52}\times 100=1.64\%$$

Table B1 shows the calculated values for different conditions. The table shows that the normal water at the examined w/s can add between 0.9 to 6.9% of air bubbles to the paste sample.

Table B1. Estimation of maximum air content originated from mixing water in cement paste with different w/s and different levels of dissolved air in the mixing water.

Dissolve air in mixing water (mg/L)	w/s	Possible % of void stemmed from mixing water in paste
20	0.40	0.9
	0.50	1.0
	0.60	1.1
	0.70	1.1
25	0.40	1.2
	0.50	1.3
	0.60	1.4
	0.70	1.4
30	0.40	1.4
	0.50	1.5
	0.60	1.6
	0.70	1.7
60	0.40	2.7
	0.50	3.1
	0.60	3.8
	0.70	3.3
120	0.40	5.6
	0.50	6.1
	0.60	6.5
	0.70	6.9

References

[1B] F. De Carlo, P.B. Albee, Y.S. Chu, D.C. Mancini, B. Tieman, S.Y. Wang, High-throughput real-time X-ray microtomography at the advanced photon source, International Symposium on Optical Science and Technology, International Society for Optics and Photonics, (2002) 1-13.

[2B] F. De Carlo, B. Tieman, High-throughput X-ray microtomography system at the advanced photon source beamline 2-BM, In Optical Science and Technology, the SPIE 49th Annual Meeting, International Society for Optics and Photonics, (2004) 644-651.

[3B] F. Marone, M. Stampanoni, Regridding reconstruction algorithm for real-time tomographic imaging, J. Synchrotron Radiat. 19 (2012) 1029–1037.

[4B] B.A. Dowd, G.H. Campbell, R.B. Marr, V. Nagarkar, S. Tipnis, L. Axe, D.P. Siddons, Developments in synchrotron x-ray computed microtomography at the national synchrotron light source, SPIE's International Symposium on Optical Science, Engineering, and Instrumentation, (1999) 224–236.

[5B] M.L. Rivers, tomoRecon: high-speed tomography reconstruction on workstations using multi-threading, SPIE Optical Engineering+ Applications, 2012.

[6B] I. Pitas and A. N. Venetsanopoulos, Nonlinear Digital Filters: Principles and Applications. Boston, MA: Kluwer, 1990.

[7B] T. Sun, Y. Neuvo, Detail-preserving median based filters in image processing, Pattern Recognit. Lett, 15 (1994) 341–347.

[8B] Z. Wang, D. Zhang, Progressive switching median filter for the removal of impulse noise from highly corrupted images, Circuits and Systems II: Analog and Digital Signal Processing, IEEE Transactions, 46 (1999), 78-80.

[9B] D. R. K. Brownrigg, The weighted median filter, Communications of the ACM, 27 (1984) 807-818.

[10B] , J.M. Wallace, P.V. Hobbs, Atmospheric science: an introductory survey, 92, Academic press, 2006.

[11B] P.K. Mehta, P.J.M. Monteiro, Concrete : microstructure, properties, and materials, 3rd ed., McGraw-Hill, New York, 2006.

Appendix-C

Number of investigated individual particles

Table. C1. Number of investigated individual particles for each dataset

Sample Code	Number of investigated discrete high-absorption materials
OPC-NL	4340
OPC-P	4611
OPC-1	3894
OPC-2	5065
OPC-3	3899

VITA

MASOUD MORADIAN

Candidate for the Degree of

Doctor of Philosophy

Thesis: DIRECT OBSERVATIONS ON MICROSTRUCTURE EVOLUTION OF CEMENT SYSTEMS AT EARLY AGES

Major Field: Civil Engineering

Biographical:

Education:

Completed the requirements for the Doctor of Philosophy in Civil Engineering at Oklahoma State University, Stillwater, Oklahoma in May, 2017.

Completed the requirements for the Master of Science in Civil Engineering/Structure at University of Tehran, Tehran, Iran in 2011.

Completed the requirements for the Bachelor of Science in Civil Engineering at K.N.T University of Technology, Tehran, Iran in 2008.

Experience:

Graduate Research Assistant, Oklahoma State University (2013-2017)
Research Assistant, University of Tehran (2009-2013)
Teaching Assistant, K.N.T University of Technology (2006-2012)

Professional Memberships:

American Concrete Institute (ACI)
The American Ceramic Society
American Society of Civil Engineers (ASCE)
American Society for Testing and Materials (ASTM)